12-2016

Experimental Characterization and Simulation of Carbon Nanotube Strain Sensing Films

Nagendra Krishna Chaitanya Tummalapalli
Western Michigan University, tnkchaitu@gmail.com

EXPERIMENTAL CHARACTERIZATION AND SIMULATION OF CARBON NANOTUBE STRAIN SENSING FILMS

by

Nagendra Krishna Chaitanya Tummalapalli

A thesis submitted to the Graduate College
in partial fulfillment of the requirements
for the degree of Master of Science in Engineering (Mechanical)
Mechanical and Aerospace Engineering
Western Michigan University
December 2016

Thesis Committee:

Dr. Muralidhar K. Ghantasala, Ph.D., Chair
Dr. William W. Liou, Ph.D.
Dr. Pavel Ikonomov, Ph.D.

EXPERIMENTAL CHARACTERIZATION AND SIMULATION OF CARBON NANOTUBE STRAIN SENSING FILMS

Nagendra Krishna Chaitanya Tummalapalli, M.S.E.

Western Michigan University, 2016

Carbon Nanotubes (CNTs) have excellent mechanical, electrical and electromechanical properties. These properties led to a lot of novel applications. Due to change in electrical properties under mechanical loading, these composites have potential applications in strain sensors, when these are fabricated as films. CNT-based films are commonly fabricated using different physical and chemical techniques based on the property requirements governing those applications. In this work, CNT films were prepared using wet chemical based methods and chemical vapor deposition techniques.

Plasma chemical vapor deposition using microwave power is used in the first method to deposit films on silicon substrates, using Nickel film as a catalyst layer. The effect of different processing steps in this method, viz., hydrogen annealing, hydrogen plasma pre-growth treatment and MWCVD deposition properties on the film properties is studied in the first stage. In the second method, Carbon nanotube-polyurethane nanocomposite films of different loading proportions (1 to 8%) are prepared along with N-methyl-2-pyrrolidone (NMP) on different substrates using a spin coating. These film properties were analyzed using different characterization techniques.

These studies demonstrated the optimization of the growth and preprocess parameters with respect to the structural phase, microstructure and conductivity of these films in both the methods. Simulation of the CNT sensor characteristics was performed using COMSOL Multiphysics software. Optical lithography is used to fabricate the sensor structures using CNT nanocomposite films. The results of these studies were discussed in detail.

ACKNOWLEDGEMENTS

I would like to take this opportunity to thank my thesis advisor Dr. Muralidhar Ghantasala for his invaluable advice, encouragement, and motivation. I am thankful to Dr.William W Liou and Dr. Pavel Ikonomov for agreeing to serve on my thesis advising committee and for their guidance throughout my Master's program. I would like to thank all professors from the Department of Mechanical Engineering, Western Michigan University for their valuable guidance and support throughout the course of my master's.

I thank Dr. Asghar Kayani, Dr. Massood Zandi Atashbar and Dr. Yang Yang for their continuous support with the laboratory equipment used in this research. I am very much grateful to Dr. Zhi Mei from Wayne State University who allowed us to use JSM-7600F SEM to characterize the samples. Special thanks to Peter Thannhauser, Glenn Hall and Matthew stoops for helping me a lot in various technical and machining aspects. I extend my thanks to Dr. KJ Suthar from Argonne National Labs who helped to carry out major discussions on the finite simulation aspects of this work. I would thank Dr. Mao Mao from COMSOL Multiphysics and Shane Smith from Elite Tooling Aerospace who contributed their help in this research. I extend my thanks to Center for Nanoscale Materials (CNM) who helped us to carry out Raman Spectroscopy analysis

I would like to acknowledge my student friends Samanthi Wickramarachchi, Amila C Dissanayake, Maddipatla Dinesh, D. Shripad, Bilge Nazli Altay who extended their helping handing in various aspects of this research.

Finally, I thank my parents TU Rao, TVPR Devi and my sister TLG Sravanthi for their invaluable support, motivation, and guidance. I am grateful for their persistence in channeling my academic goals and ambitions.

Nagendra Krishna Chaitanya Tummalapalli

TABLE OF CONTENTS

Table of Contents - continued

Table of Contents - continued

Table of Contents - continued

LIST OF TABLES

LIST OF FIGURES

List of Figures-continued

List of Figures-continued

List of Figures-continued

1 INTRODUCTION

In this chapter, introduction to the basic concepts of this research are given which include, carbon nanotubes, CNT based sensors etc. It highlights objectives and novelty of this work and finally concludes by stating the organization of the thesis.

1.1 Carbon Nanotubes

Carbon nanotubes are made of carbon atoms arranged in rolled up structures. They have extremely high strength resulting from their sp^2 bonds. This means that 2s and 2p shell of each carbon atom are bonded to the 2s and 2p bonds of adjacent neighboring atoms. However due to the defects in the structure, they form sp^3 bonds sometimes which results in bonding to 4 other atoms which may change their structure. They have spectacular properties. These properties make them a key application in nanotechnology. They are cylindrical elongated structures. They are mainly classified as single walled carbon nanotubes and multi walled carbon nanotubes. The properties of CNTs depend on their geometry. They can be metallic or semiconducting. Their applications include fibers[1], [2], composite materials[3], [4], transistors [5], nanowires [6], fuel cells [7]–[9], gas storage [10], LED's [11] etc. Figure 1 shows the picture of single, double and multiwall carbon nanotubes. Apart from the above mentioned applications, CNT sensors are attracting the present day research. The individual properties of CNTs constitute the properties of the sensor. CNTs are applied in sensors based on films because individual CNTs cannot form a sensor by their own. Hence CNT based sensors are fabricated by growing forests of CNT films using PECVD technique or synthesizing CNT-polymer nanocomposites.

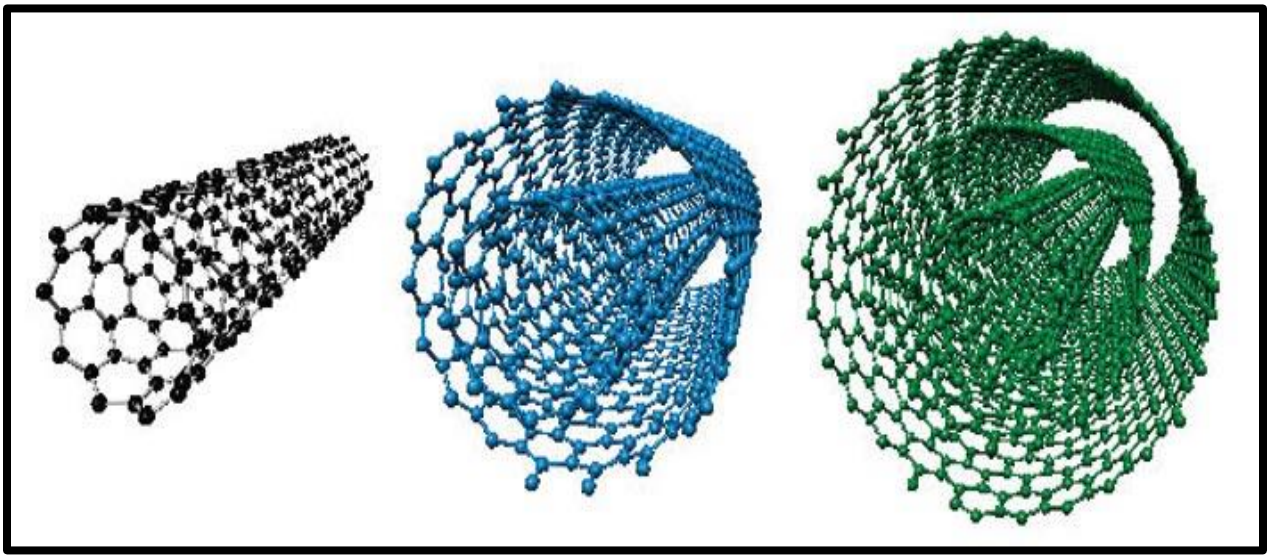

Figure 1: Single, double and multi-walled carbon nanotubes

1.2 Sensors

A sensor is a device, which transforms one form of energy into another. It can also be defined as a device which detects and responds to input data and exhibits the output. There are basically two types of sensors. They are analog sensors and digital sensors.

Analog sensors produce a continuous output signal which is generally proportional to a quantity which is being measured. Digital sensors produce a discrete output signal or voltage that is a digital representation of the quantity being measured. They usually produce binary output signals. The wide range of sensors include thermostats [12], light sensors [13], cameras [14], ohmmeters[15] barometers [16], photodetectors [17] etc. CNT based sensors are more advantageous compared to the above stated conventional sensors, in terms of cost, accuracy and sensitivity.

1.3 Sensors based on CNTs

Carbon nanotube based sensors are fabricated by growing thin films of CNT forests using PECVD technique and synthesis of CNT-polymer sensors. Arrays of CNTs are grown on substrates using various techniques like laser ablation, arc discharge and chemical vapor deposition (CVD) etc. CVD is widely followed technique because of various advantages compared to the other techniques [18] and is used in this research. CNTs act as fillers in polymer matrices to form CNT-polymer composite materials. These composites are further fabricated to form sensors. CNT-polymer composite sensors have improved mechanical, electrical and electromechanical properties. They have wide range and high performance applications. CNTs are mainly loaded into polymer matrices to increase the electrical conducting properties. These composites change their electrical properties under mechanical loadings. This is one of the main motivation behind our research. Some of the major classifications of CNT based sensors are:

- Nano-scale sensors.
- Macro/micro-scale sensors.

These sensors are used to measure temperature, strain, pressure etc. which are used in various industrial or commercial applications. With the latest development in recent times, it is easy to fabricate a sensor with exceptional properties like low cost, long life, high accuracy, high sensitivity etc. Nanotechnology is creating a boom in the field of fabrication of sensors. CNTs are incorporated in polymer matrices to form CNT-polymer nanocomposites. These nanocomposites are fabricated into devices and sensors.

1.4 CNT-polymer nanocomposites

Nanocomposites are made of electrically insulating material acting as the domain and incorporating electrically conductive materials like metallic nanoparticles, CNTs etc. After the

discovery of CNTs and study of their exceptional properties, CNT composites have become one of the most interesting and promising studies. They are synthesized using CNTs as fillers, surrounded by polymers as the matrices of the composite. Research on wide variety of polymers were done till date including, epoxy, polyamide, polyurethane, polyethylene and polycarbonate etc.[19]. These composites are used in many fields like electronics and data storage, defense, aerospace etc. Figure 2 shows the examples of commercial products containing CNT-polymer composites.

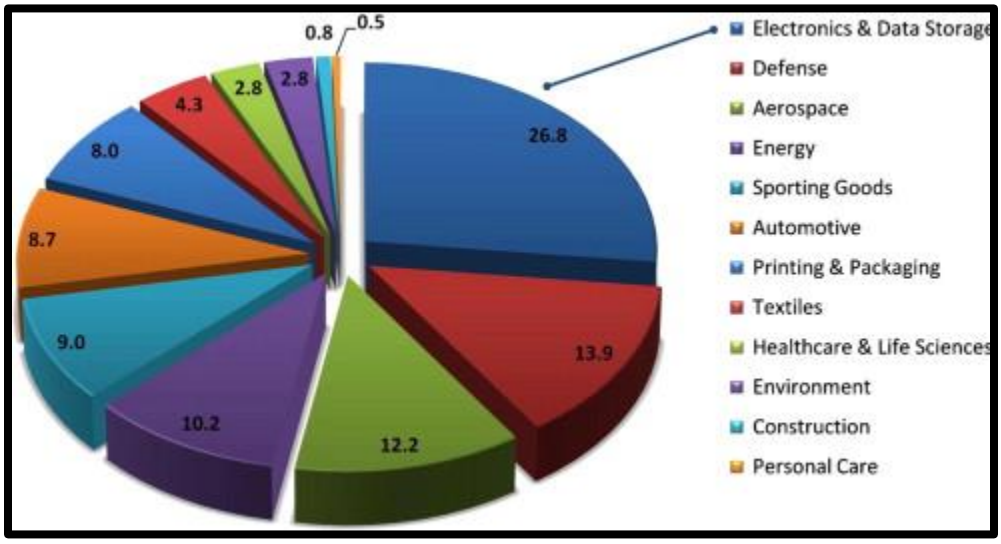

Figure 2: Examples of commercial products containing CNT-polymer composites [19]

1.5 Motivation

Carbon nanotubes (CNTs) are graphitic carbon fillers in nanoscale with unique mechanical, electrical, optical, transport and electromechanical properties. Incorporating these CNTs in polymer matrices results in nanocomposites with improved mechanical, electrical and transport properties for wide range of applicatons. CNTs increase the mechanical strength and electrical conductivity of these composites without affecting other properties. CNT composite films are synthesized using various techniques. They are synthesized using CNTs as fillers which is surrounded by polymer matrix.

Polymers have applications in many fields like electronics, aerospace, biomedical and automotive industries. Electrically conductive composites are primarily composed of conducting and insulating heterogeneous material systems. The conducting phase may be carbon particles, metallic particles etc. with polymers acting as the insulating materials. Recent researches focused mainly on CNTs or metallic nanoparticles. These nanoscale fillers have benefits like high surface

to mass ratio, high aspect ratio and light weight which further improve the properties of CNT nanocomposites.

These composites change their electrical behaviour w.r.t mechanical loading. Hence the potential applications of these CNT-polymer composites include stress and strain sensors, actuators etc. These composite sensors have a wide range of advantages compared to other sensors like high sensitivity, flexibility. Stretchable sensor applications include large scale neuron sensor networkson humans, engineering structures etc. Despite of many potential applications, this field has not attracted real world applications because lack of understanding the physics at nanoscale, variance in reported performance results, and the behaviour of these sensors in various environments. Thus, this is a field which needs lots of understanding and also questions that need to be answered.

1.6 Objectives of the study

A complete understanding of CNT based sensors and study of its behavior and properties require an in-depth study. This can be done by growing the carbon nanotubes based films, synthesizing the nano-composites, finite element analysis and fabrication of the sensor. Present studies are limited to material properties study, nano-composites study or finite elemental study. But significant research is not done to compare all the values. This research addresses these deficiencies and hence the main objectives of this work are

1. Growth of CNT based films using PECVD technique.
2. CNT-polymer nanocomposite synthesis.
3. Characterization of CNT based films.
4. Multiphysics simulation of nanocomposite strain sensor using COMSOL Multiphysics.
5. Fabrication of CNT-polymer strain sensor using optical lithography.

1.7 Statement of novelty

The study reported in this thesis extends existing knowledge on growth of CNT based films using PECVD technique, synthesis of CNT composites with study of electrical conductivity behavior of CNT based films with several unique contributions. Characterization of CNTs grown by PECVD technique, CNT composites is presented.

An intensive study on optimizing growth parameters of CNT based films using PECVD technique, like annealing treatment time, plasma treatment time and growth time is carried out. The increase in surface energy process was done through UVO exposure by optimizing the exposure times and further calculating the surface energy. These films are characterized using RBS, Raman spectroscopy, SEM, 4-probe electrical conductivity studies etc. It is extended to the synthesis of CNT-polymer composite based films. CNT wt. % loading, post deposition annealing temperatures, spinning speeds and times for the fabrication and deposition of CNT polymer composites and

thin films are studied. These CNT composite films are characterized using SEM, Raman spectroscopy and 4-probe electrical conductivity studies. After the synthesis of CNT based films, strain sensor finite element simulation is done.

Mechanical design software, Catia V5, was used to design the sensor model and COMSOL Multiphysics 5.2a was used to perform the finite element analysis. The material properties, necessary boundary conditions, proper mesh and post processing the results is determined sequentially. To the best of the author's knowledge, this study is first time reporting the Multiphysics simulation of CNT-polymer composite strain sensor using COMSOL Multiphysics 5.2a software.

Optical lithography is used to fabricate this CNT-polymer composite sensor by designing an experimental. This sensor is mounted on a cantilever beam and is used to study the strain induced in the beam due to mechanical loading. The data was acquired using National Instruments data acquisition systems and interpret the data using LabVIEW. This data is compared to the conventional strain gauge data and is computed for gauge factor. The results are accurately analyzed and interpreted by comparing the experimental and finite element simulation results.

1.8 Thesis outline

Chapter 2 presents the literature review of carbon nanotubes, its related structures and their properties, CNT-polymer nanocomposite synthesis, sensors in present world and their pros and cons, structural and electrical sensing of CNT based devices, application of CNT polymer composites in various sensors,

Chapter 3 focusses on equipment and materials used in this research and their technical information provided by manufactures, experimental techniques that are carried out during this thesis and fabrication methods and techniques. They include PVD, PECVD, spin coating, ultrasonication, UVO exposure etc. This chapter also presents characterization techniques like SEM, RBS, Raman Spectroscopy, 4-probe electrical conductivity measurements.

Chapter 4 presents information on sample preparation which include catalytic thin film deposition, CNTs synthesis, synthesis and deposition of CNT-polymer composites and various experimental parameters which are optimized.

In chapter 5, CNT-composite sensor fabrication for strain sensing purpose, using optical lithography technique, is discussed. This includes the complete discussion on the experimental procedure and optimization of various sequential steps included in the process.

Chapter 6 will focus on designing the sensor model using Catia V5 and exporting that model to COMSOL Multiphysics and performing the finite element analysis. Setting up the model, defining the material properties, boundary conditions, mesh, processing and post processing of the results will be discussed completely.

In chapter 7, the main results, discussions and conclusions are reported with the necessary scientific explanations. The future scope of the project is also discussed in this chapter. Additional information is given in the form of pictures, tables, graphs and appendix.

With this introduction to the concept of Carbon nanotubes, CNT based sensors and nanocomposites, the next chapter would review the existing literature on CNTs and its properties, CNT based polymer nanocomposites and finite element simulations of strain gauges.

2 LITERATURE SURVEY

In the previous chapter, we have discussed the basics of carbon nanotubes, polymer composites and CNT based sensors. In this chapter, the existing literature of CNTs and their properties, synthesis techniques of CNTs using plasma enhanced chemical vapor deposition technique, synthesis of carbon nanotube polymer composites and their properties, finite element modelling and analysis of strain gauges is discussed in detail.

2.1 Carbon nanotubes (CNTs) and C60 and their properties

Research and development of carbon nanostructures led to the discovery of C60 (figure 3) and carbon nanotubes. After diamond and graphite, Buckyball C60 is the pure form of carbon. It has 60 carbon atoms consisting of truncated icosahedrons, a polygon with 60 vertices and 32 faces where 12 of them are pentagonal, and 20 of them are hexagonal. It was discovered in the year 1985 by Dr. Richard E. Smalley and a group from Rice University and named after R. Buckminster Fuller, a famous American architect[20].

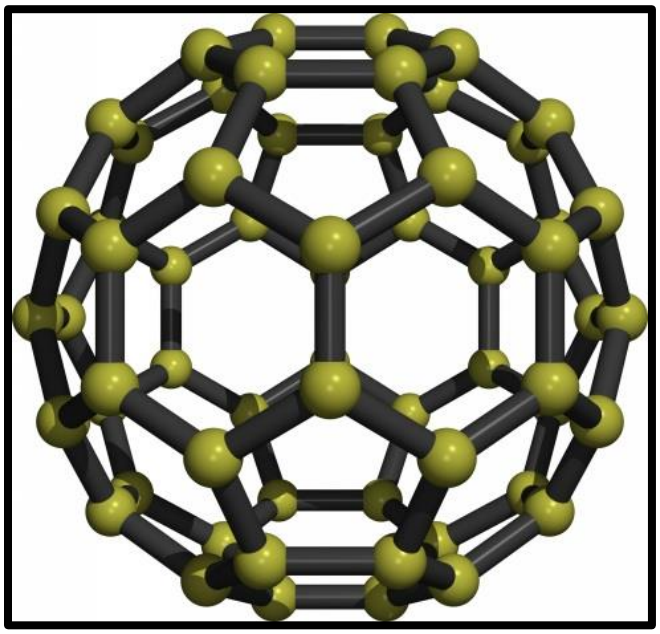

Figure 3: Buckminsterfullerene or C-60 molecule

Transmission Electron Micrographs of elongated carbon nanoparticles with capped ends, consisting of cylindrical graphitic layers, obtained by Iijima in 1991 led to the discovery of CNTs [21]. They are made of graphitic shells with adjacent shell separation of 0.34nm. Structurally CNTs are made of rolling up the graphene sheets. These graphene sheets consist of carbon atoms in a

hexagonal lattice. They are the products formed as a result of the catalyst reacting from the thermal decomposition of hydrocarbon gasses CNTs in macroscopic quantities were successfully made in 1992 by Ajayan and Ebbesen [22]. Carbon-arc discharge method, laser ablation method, chemical vapor deposition (CVD) method, flame synthesis and Smalley's high-pressure carbon monoxide (HIP-CO) are some of the mostly followed CNT synthesis techniques.

Single-wall CNTs (SWCNT) and multi-wall CNTs (MWCNT) are the two types of CNTs, shown in figure 4. SWCNTs are made from a sheet of graphite which is rolled into an endless cylinder. A nanotube indicated by the indices (11, 7) (figure 5) can be formed by rolling up the sheet along the vector C. Armchair and zigzag CNTs are formed by rolling the sheet along the dotted line. All other wrappings lead to chiral tubes whose wrapping angle is given on zigzag direction or arm chair direction. The angle between T and H is the chiral angle Φ. Dashed lines are perpendicular to C and run in the direction of the tube axis T vector. The solid vector H is perpendicular to the armchair direction and specifies the direction of nearest-neighbor hexagon rows indicated by black dots. CNTs can be fabricated by wrapping up a single sheet of graphite such that two hexagonal lattice sites coincide. The wrapping vector C is specified by a pair of integers (n, m) and two unit vectors a_1 and a_2 and is given by the following equation

$C = na_1 + ma_2$. ……(1)

If n=m, it's an armchair tube and zigzag when m=0. All other tubes are the chiral type and have finite wrapping angle in between 0° and 30°. Arm-chair tubes are metallic if the bands are crossing Fermi level. For all other tubes, they may be metallic or semiconducting. The gap should only depend on the diameter.

MWCNTs contain overlapping cylindrical tubes like coaxial cables. Their diameter ranges from few to 40nm and length of few micrometers. They consist of thicker walls, having multiple coaxial graphene cylinders separated around 0.34nm (which is the interlayer distance in graphite). The aspect ratio of nanotubes varies with the diameter. CNTs prepared experimentally are observed to be closed at both ends which involve the introduction of pentagonal topological defects. Thus, the tubes are essentially made of cylinders attached to halves of large fullerene-like structures at the ends.

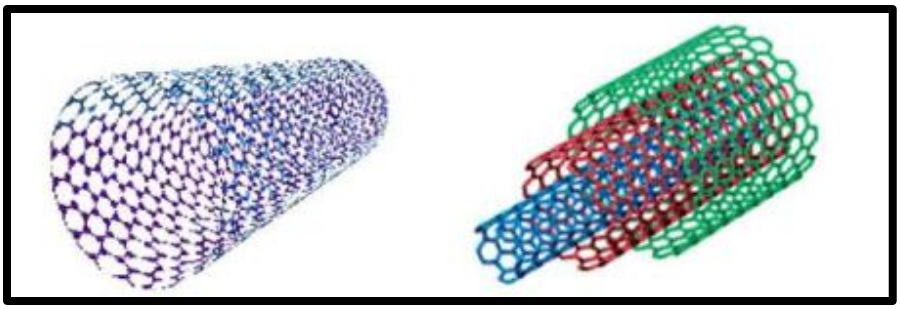

Figure 4: Single and multiwall carbon nanotubes

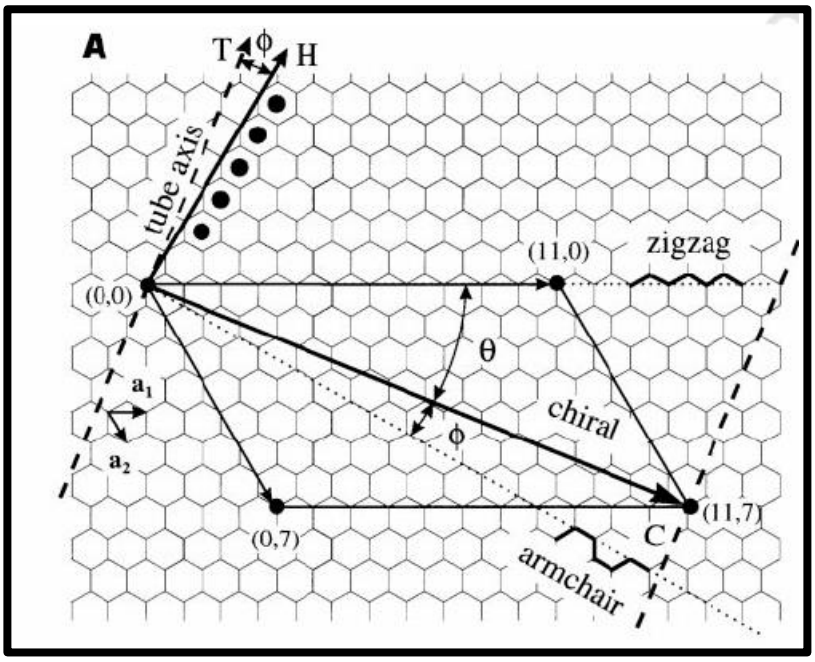

Figure 5: Relation between the hexagonal carbon lattice and the chirality of carbon nanotubes [23]

Regarding tensile strength and elastic modulus, CNTs are one of the strongest materials. An MWCNT resulted in tensile strength of 63GPa [24] when tested in 2000 and also high elastic moduli in order of 1Tpa.This high strength is the result of the covalent sp^2 bonds formed between individual carbon atoms. They have remarkable field emission properties [25], [26], [27], [28], [29]. Their excellent structural, electrical and mechanical properties of CNTs made them applied to nanoelectronic devices [30], field emission sources [31], supercapacitors [32] and scanning probes [33]. For the applications of CNTs in various fields, they properties should be studies thoroughly.

2.2 Properties of carbon nanotubes

After the discovery of CNTs, the study of its properties, opened a wide way of research to study the interesting properties of a new material. The interesting point to be noted is that, the properties of CNTs depend on various factors size, defects and orientations etc. Most of the researchers reported that, it exhibited a combination of ideal properties including mechanical, electrical, thermal, transport, optical and electromechanical properties etc. which them as the ideal material in many applications. Hence it's important to study the properties of CNTs in detail.

2.2.1 Mechanical properties

CNTs are one of the strongest materials in nature. The superlative mechanical properties of CNTs make them the filler material of choice for composite reinforcement. They are long cylinders of graphene. CNTs has different properties in axial and radial directions because of its structure. CNTs are very strong in axial direction. Young's modulus is in the order of 270-950GPa and tensile strength of 11-63GPa[34], compressive strength around 100GPa, stiffness of 230 – 725GPa [35]. They are soft in their radial direction. Radial direction elasticity is of CNTs is important especially for CNT composites where these fillers are subjected to large deformations in transverse direction under the applied load. They have high stiffness and axial strengths up to 100 times higher than that of steel. Many studies were carried out on the elastic & inelastic, fracture behaviors of CNTs [36]–[40]. Mechanical properties are influenced by diameter, length, aspect ratio and defects of tubes. The present issue with today's research is understanding the bonding between at the surface interface of CNT and polymer which one day would make a huge contribution to this field. Some of the important mechanical properties present in the existing literature are given in figure 6.

Properties	SWCNTs	MWCNTs
Specific Gravity	0.8 g/cm^3	1.8 g/cm^3
Elastic Modulus	~1 TPa	~0.3 – 1 TPa
Strength	50 – 500GPa	10 – 60 GPa
Resistivity	5 – 50 μΩ cm	5 – 50 μΩ cm
Thermal Conductivity	3000 W m^{-1} K^{-1}	3000 W m^{-1} K^{-1}
Thermal Stability	>700 °C (in air); 2800°C (in vacuum)	>700 °C (in air); 2800°C (in vacuum)
Specific Surface Area	~400-900m^2/g	~200 – 400m^2/g

Figure 6: Mechanical properties of CNTs present in the literature [41]

2.2.2 Electrical properties

Carbon nanotubes have emerged as a potential material of the new century and are being considered for a whole host of applications ranging from large scale structures in automobiles to nanometer scale electronics. The electronic band structure of nanotube can be described by considering the bonding of the carbon atoms arranged in a hexagonal lattice. Each carbon atom is covalently bonded to three neighbor carbons via sp^2 molecular orbitals. The fourth valence electron, hybridizes will all the other p_z orbitals to form a delocalized π-band. Graphene can be metallic or semiconducting[42] because it has got two carbon atoms in the unit cell. Mintrime [43], Hamada[44] and Saito[45] believed that the conducting properties can be determined by tight-binding electronic structure calculations between the coefficients (n_1 and n_2) of the

translational vector $C_h=n_1a_1 + n_2a_2$, which connects two crystallographically equivalent sides. When $2n_1 + n_2$ is multiple of three, then the CNT exhibit non-metallic or semi conducting behavior, with a band gap for conduction (E_g), is obtained in all other cases. When $n_1 = n_2$, SWCNTs are armchair tubes which are metallic in nature. The fermi level crossing for zig-zag (n_1, 0) can be metallic or semi-conducting.

CNTs have their superior electrical properties due to their electronic structure of graphite and 1-D character. Resistance to electron flow in materials is caused by electron collision with defects. Such collisions scatter electrons from their path, increasing the electrical resistance. In a 1-d structure like CNTs, electrons can travel only forward or backward indicating that resistance can only occur when atoms travel backwards (backscattering). This backscattering of electrons causes resistance in CNTs. If CNTs don't have any defects, then electronic transport takes place by acoustic phonons and optical phonons[46]. They also carry high current densities (10^9 – 10^{10} A/cm^2). It conducts current without change in structural morphology or measurable change in resistance for temperatures up to 250°C. Bending and twisting of CNTs also affect their electrical properties. Exposure to gases also changes the resistance of these CNTs which makes them potentially applicable as a chemical sensor with fast response and high sensitivity. CNTs are grown or supported on substrates which can be placed on the structures to measure stress, strain etc. due to the change in their structure or properties due to loading. That's the reason, they are the ideal fillers in polymer composites. Nanotube bending leads to mixing of π and σ states, leading to enhanced density of states in the valence band near Fermi energy.

2.2.3 Electromechanical properties

A lot of research was done on the effect of electrical properties, when a carbon nanotube is subject to loading or twisting [47]–[51]. In general, theory suggested that the electromechanical properties of SWCNTs depend on chirality defined by the tube index. When CNTs are subjected to mechanical loading, band-gap changes are induced w.r.t. change in their structure. This concept makes them potentially applicable to electromechanical devices. Tombler [52] et al. was the first group to publish experimental work on electromechanical properties of SWCNTs. They used AFM tips to push suspended SWCNTs and observed up to 2 orders of magnitude conductance change at high strain for metallic SWCNTs. They further used non-orthogonal tight bonding molecular dynamics simulations to investigate the underlying physics of this electromechanical response. Figure 7 shows a SWCNT partly suspended over a trench for electromechanical measurements.

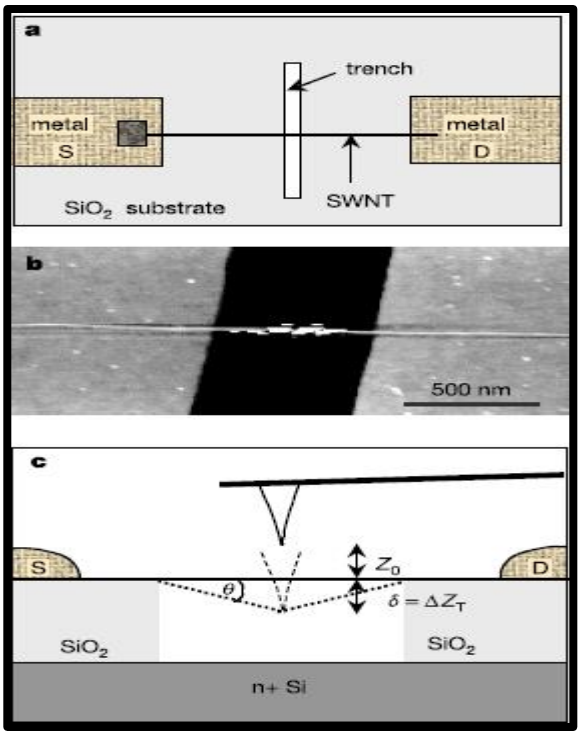

Figure 7: A SWCNT suspended over a trench and deformed using the tip of an AFM for electromechanical measurements [52]

The change in bandgap, induced by mecanical strain, is another mechanism responsible for CNT electromechanical behaviour [53]. Minot et al. demonstrated that it was possible to open a band gap in metallic CNTs or alter their electrical properties. These studies were crucial in demonstrating piezoresistivity individual nanotubes and exploring the mechanisms responsible for this response.

All these properties put together could make them as potential applications in the development of high sensitivity, low cost strechable sensors based on CNT-polymer nanocomposites. As a result CNT-based polymer sensors have been devoloped. In the following sections, literature survey on synthesis of CNTs, CNT based sensors and CNT-polymer nanocomposites will be presented. There are few more properties of CNTs which are presented in figure 8. With these dominating properties in various aspects, CNTs and CNT based films are applicable in various applications.

Properties of Carbon Nanotubes

Property	Item	Data
Geometrical	Layers	Single/Multiple
	Aspect Ratio	10-1000
	Diameter	~0.4nm to >3nm (SWNTs) ~1.4 to >100nm (MWNTs)
	Length	Several μm (Rope up to cm)
Mechanical	Young's Modulus	~1 TPa (steel: 0.2TPa)
	Tensile Strength	45GPa (steel: 2GPa)
	Density	1.33~1.4g/cm^3 (Al: 2.7 g/cm^3)
Electronic	Conductivity	Metallic/Semi-conductivity
	Current Carrying Capacity	~1TA/cm^3 (Cu: 1GA/cm^3)
	Field Emission	Activate Phosphorus at 1~3V
Thermal	Heat Transmission	>3kW/mK (Diamond: 2kW/mK)

Figure 8: Properties of Carbon nanotubes [54]

2.3 Synthesis of Carbon Nanotube based films

Investigation on growth and characterization of CNTs were encouraged after the invention of MWCNTs in 1991 and SWCNTs in 1993 by Sumio Iijima [21], [55], [56]. CNT films are synthesized using various techniques like Plasma Enhanced Chemical vapor deposition (PECVD), arc discharge, laser ablation etc. Among all the techniques PECVD turns out to be more advantageous, as mentioned earlier. PECVD technique mainly uses two power sources which are radio frequency (RFCVD) and microwave (MWCVD) frequency power sources. The growth of CNTs using PECVD technique is summarized in this chapter. Compared to both, MWCVD seems to be more dominating because it possesses high frequency and high energy. Hence it is widely used technique to promote the growth of CNTs.

2.4 Microwave Chemical Vapor Deposition (MWCVD)

CNTs grow well in using MWCVD systems [57]–[59]. This technique uses microwave frequency power as the input parameter. In this process, substrates are coated with catalytic thin films which are grown using physical vapor deposition technique. Growth of CNTs using this technique involved three important steps. They are annealing, plasma treatment and growth of CNTs. All these processes are done in a vacuum chamber.

Annealing is done to remove the traces of oxygen or oxygen thin films that might form of catalytic thin films. Hydrogen gas is mostly used for this process. This is done usually at higher temperatures. After hydrogen annealing process, power is coupled to the system. The power can be microwave or radio frequency power source. During the plasma treatment process, continuous thin film of catalyst is broken down into small nano islands. The properties of resulting CNTs depend on the size of these catalytic islands size. After the plasma treatment step, hydrocarbon gas along with an inert gas is sent into the chamber. Inert gas breaks the hydrocarbon gas into corresponding hydrogen and carbon atoms. Hydrogen is sent out of the system while carbon atoms get settled or get penetrated the catalytic nano islands. Depending on the adhesion properties of catalytic island with the substrate, growth of CNTs occurs in two models. They are tip-growth and base-growth models. This process if further discussed in the coming chapters in detail. Hence the growth and properties of CNT based films depend on the nature and thickness of the catalytic thin films deposited on the substrates.

2.5 Catalyst preparation on Si and SiO_2 substrates

Electron gun evaporation [60], thermal evaporation [61], ion beam sputtering [62] and magnetron sputtering [63] are some of the physical techniques used for depositing catalytic layers on the substrates. The properties of the carbon nanotube depend on the catalytic nano island that form on these layers. Hence the deposition time and thickness of these catalyst layers have a significant role in the experimental process. Inert gasses like ammonia and hydrogen are used for creating the catalyst nano-particles using ion bombardment at higher temperatures on the substrate [64]. Iron, cobalt, nickel, copper, platinum, etc. are some of the layers used for catalyst depositions because of diffusion rate and high solubility of carbon in these metals at high temperature [65]. After depositing the metallic thin films, CNTs based films are grown using MWCVD technique. Also, CNT film based sensors are fabricated using CNT-polymer nanocomposites.

2.6 Carbon nanotube-polymer nanocomposite

Carbon nanotubes possess high tensile strength and elastic modulus which results from the sp^2 bonds formed between the individual carbon atoms. Thermal, mechanical and barrier properties of these polymer-based composites are enhanced significantly by reinforcing CNTs into the polymer matrix. Carbon nanotube composites are made up of the polymer matrix and carbon nanotubes as fillers which are embedded in this matrix. CNTs possess high surface energy and the tendency for agglomeration because of its high aspect ratio and its nano-range size. CNTs usually exists as bundles or ropes. Homogenous dispersion of these bundles and ropes can be achieved by separating these bundles or clusters into individual elements. Noticeable changes have been made to these CNT composite materials. Nano composites with enhanced physical properties like conductivity, strength, elasticity and toughness are fabricated easily.

Several methods have been successfully investigated in preparing these composites like solution casting, melt-mixing and in situ polymerization. Effective properties and functional uses of these composites are mainly dependent on the distribution of CNTs in the polymer matrix which is the greatest challenge to today's researchers. Based on the type of polymers, thermosets or thermoplastics, there are several methods for producing polymer/CNT composites[66]. Good interfacial bonding, CNT dispersion, alignment and de-agglomeration are the key factors that affect the properties of CNT nanocomposites. To use the properties of the CNTs in the composites, they should be dispersed uniformly and individually throughout the composite. To the achieve load transfer across the CNT-polymer interface, good interfacial bonding is required. Most available forms of CNTs today are isotropic, fragile and contain many species. Production process on a large-scale produce a wide range of carbonaceous materials like fullerenes, amorphous carbon, etc. which can be removed by thermal annealing in air or oxygen or acid treatment for removing catalyst residues.

As mentioned above, CNTs tend to agglomerate which weakens the strength of the nanocomposite. To make it strong, CNTs should be de-agglomerated which is achieved by ultrasonication of the nanocomposite solution. CNTs are introduced into many polymer matrices, such as poly (methyl methacrylate)[67], polystyrene[68], nylon-6[69], polyaniline[70], polyethylene[71], [72], Polyurethane[73], epoxy-resin[74], poly (vinyl alcohol)[75] etc. Two methods have been used to fabricate these nanocomposites: non-covalent attachment and covalent attachment. These composites are used in many applications like light emitting diodes, photo voltaic solar cells, gas sensors, medical devices, coatings, adhesives, packaging materials, etc. Direct incorporation of CNTs into the polymer matrix is non-covalent attachment while in situ polymerization at their surface is a covalent attachment. The properties of nanocomposites depending upon the dispersion of CNTs in the polymer matrix.

2.7 Dispersion of CNTs

Surface morphology and strong covalent attractive bonding forces between CNTs are the major governing factors in CNT dispersion [76], [77]. For the CNTs to be dispersed well in the polymer matrix, these forces need to be overcome. Extrusion [78], sonication [79], shear mixing [80] are some of the techniques to disaggregate these CNTs and disperse them in the polymer matrix. Sonication is the most practiced technique for disaggregating the CNTs. Low power and short time are the best sonication parameters in the presence of a surfactant. Localized heating and cavitation forces support this process. Sometimes cavitation forces may degrade or shorten the CNTs [81]. Hence, the composite is fabricated either by dispersion of CNTs in the polymer solution or in-situ polymerization. The bonding between the CNT and polymers is believed to be a result of π-π stacking or non-covalent interaction, with some polymers. However most of CNTs are randomly distributed in the polymer matrix. Significant research is going on to distribute the CNTs in a specific direction with uniformity because the properties of these composites depending on many factors like CNT wt. %, CNT orientation, bonding between CNT and polymer matrix etc.

2.8 Properties of CNT-polymer nanocomposites

Composite materials with one of the constituent materials in the nanometer range are called nanocomposites. Atomic and molecular interactions strongly influence the macroscopic properties of the materials in this range. Mechanical, thermal and barrier properties of composite materials are improved by reinforcing small percentage of CNTs. CNTs are being commercialized in recent times where strength, conductivity, and other material properties need to be enhanced. Enhanced physical, chemical, transport and mechanical properties are offered by these CNT composite materials nowadays. Homogeneous distribution of CNTs throughout the composite is the key step for utilizing the properties of CNTs in the composite. Repeating and reproducing of same distribution of CNTs in the polymer matrix is a challenging task. This is one of the hot topics of the worldwide research taking place nowadays and its applications include photovoltaic devices, sensors, actuators, electromagnetic interference shielding (EMI) etc. Electrical properties of the composites change under mechanical loading, and this phenomenon makes it as an application in strain gauges. The main advantages of these strain gauges are it has high strain sensitivity, high accuracy and ease of production. Like the strain sensor, a wide variety of CNT-polymer based sensors are produced.

2.9 Carbon nanotube—polymer composites based sensors

Instruments or devices that sense or measure parameters like pressure, strain, temperature, etc. and convert them into measurable electrical signals are known as sensors. An ideal sensor should possess qualities like high sensitivity, reliability, responsive time, low production cost and easily reproducible in large numbers, etc. They have a wide range of applications in industry, research, etc. CNT's are the best sensing materials used to fabricate sensors in the micro and nanoscale. They can be easily dispersed in the polymer matrices based on a variety of standard procedures available like ultra-sonication or vacuum filtered techniques. Stress, strain, pressure, chemical, flow, gas, optical, position, biological sensors, etc. are some of the fields of its applications. CNT-polymer strain gauges are only considered for this research. These composites can be deposited as thin films on the substrates and can be used as CNT film sensors. These sensors can be easily mounted on the structures. They are highly fragile and experience low strain transfer because the interaction between the CNTs in the film is weak. Thus, the sensitivity of these type of sensors is quite low. With many of the advantages in the CNT based sensors and disadvantages in the conventional sensors, CNT based sensors are given high priority. An ideal strain sensor should possess some standard properties.

2.10 Performance characteristics of strain sensors

Some of the important performance characteristics of strain sensors include:

- Spatial resolution: they should be able to measure strain at any given point.
- Temperature insensitivity: they should behave ideally similar at all the temperature conditions.
- Sensitivity: they should experience high or low strains and should report them accurately
- Response time: they should possess a small response time.
- Stability: they should have long operating life even when frequently used.
- Ease of production: the production process should be simple.
- Repeatability: the results should be same whenever examined and also the sensor need to be fabricated with the same properties always.
- Mass production: they need to be produced in large quantities to be commercialized.

However, conventional strain gauges have lot of limitations.

2.11 Limitations of present existing strain gauges

Most of the strain sensors are made of metals, especially constantan (copper-nickel alloy) fabricated on the polymer substrates. They are easy to handle and install but the main limitations are [82].

- Low flexibility.
- Low gauge factors.
- Low dynamic range.
- Temperature sensitivity.
- Long term stability.

To overcome these limitations, CNT film based sensors are fabricated.

2.12 CNT-polymer strain sensors

A strain sensor measures the physical deformation of a component by experiencing the same strain as the component where it is placed.The electrical resistance of composites changes when a tensile or a compressive load is applied [66]. The change in the electrical properties are studied before and after applying the loads and then the deformations in the structure are determined. Strain gauges are categorized as piezoresistive, piezo capacitive, piezoelectric and semiconductor strain sensors. Carbon nanotubes are dispersed in the polymer matrix to form carbon nanotube composites, and these composites are spin coated and patterned on the substrates to form strain sensors with a thickness of around 150-200 µm. Most of the times CNTs are randomly distributed in the polymer matrix. They are sometimes directionally aligned using Langmuir-Blodgett

method. These sensors have high sensitivity than conventional strain gauges, and they can be easily mounted on different engineering structure based on the required configurations. The effectiveness of a strain gauge is determined by it gauge factor which is computed from

$$\text{Gauge factor (G.F)} = \frac{\frac{\Delta R}{R0}}{\frac{\Delta L}{L}} \quad \ldots\ldots (2)$$

Where, ΔR is change in resistance, R_0 is resistance of the specimen and ΔL is change in length and L is length of the specimen.

Different types of polymers are used to synthesize these CNT-polymer composites which include polystyrene, polypropylene, PMMA, PDMS [65], [83]–[85] etc. These composites are characterized in various conditions like static & dynamic, tensile and compressive strains and reported their gauge factors. This proves that CNT-polymer based strain sensor is one of the trending topic which requires in depth study. However, CNT strain sensors should possess good electrical conducting nature to act as a strain sensor because of strain sensor working principle. Hence the study of electrical conductivity property of CNT-polymer composites is highly advisable.

2.13 Electrical conductivity of CNT composites

Number of studies are carried out on the electrical conductivity of CNT composites [86]–[96]. DC resistance technique was used in this research to characterize the electrical nature of CNT composites. In the case of DC conductivity, significant current is passed into the sample and corresponding voltage is determined. According to Ohms law,

$$V = I \times R \quad \ldots\ldots (3)$$

Where, V is potential drop across the conductor, I is current through the conductor and R is resistance of the conductor.

The resistance here depends on intrinsic resistivity, length and cross sectional area of the specimen.

$$R = \rho \frac{L}{A} \quad \ldots\ldots (4)$$

This DC resistance is used to find the surface and volume resistivity.

$$\text{Volume resistivity } (\rho_{vr}) = \frac{VA}{It} \quad \ldots\ldots (5)$$

Where, V is voltage, A is area, I is measured current and t is thickness.

$$\text{Surface resistivity } (\rho_{sr}) = \frac{Vw}{IL} \quad \ldots\ldots (6)$$

Where, V is voltage, w is width of sample, I is measured current and L is distance between electrodes.

Figure 9 and 10 shows the experimental setup for calculating volume resistivity and surface resistivity.

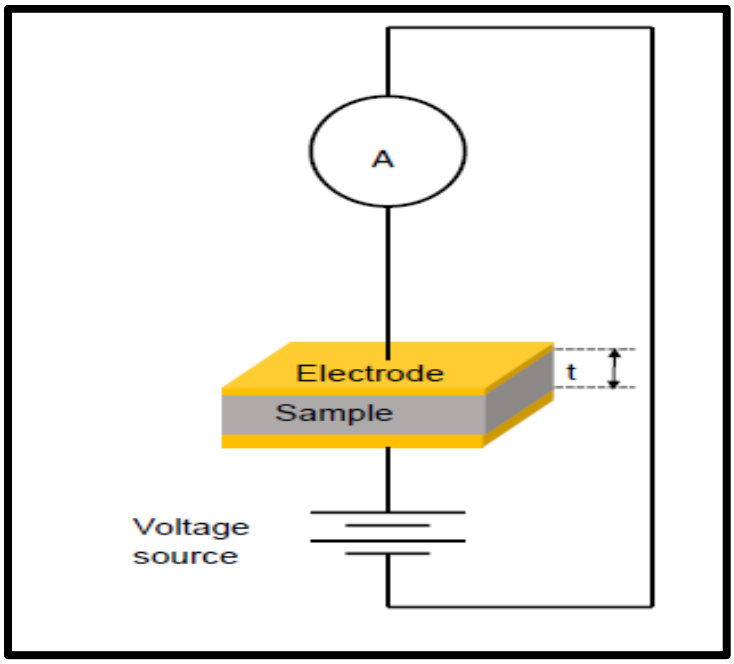

Figure 9: Experimental setup for measuring volumetric resistivity [97]

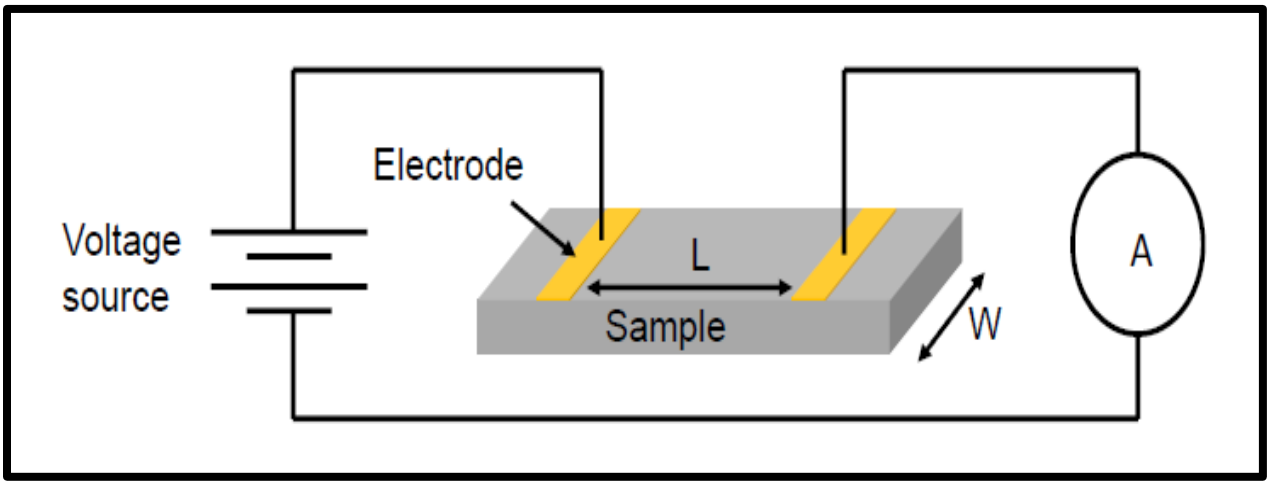

Figure 10: Experimental setup for measuring surface resistivity [97]

From the above equations, the electrical conductivity can be obtained. This electrical conductivity is analyzed with the wt. % of CNTs in the composite. The conductivity shows an increasing trend w.r.t. increase in CNT wt.% loading, which means it takes place in insulator-to-conductor transition of CNT composites, from no CNTs lo maximum wt.% loading of CNTs. This transition occurs as 3-stage process. In the stage-I, the composite behaves in insulating phase where the inter-tube distance between the CNTs is greater than the tunneling distance ($D > D_t$). In the stage-II, where few more CNTs are added to the composite, the inter-tube distance is less than the tunneling distance which increases the conductivity. This region is called percolation region and the wt. % of CNTs at this stage are called as percolation threshold. As the wt. % of CNTs keeps on increasing, the conductivity reaches the maximum value. Tunneling effect is the important parameter in piezo resistivity and it was found to be dominated when the inter-tube distance is less than 1.8nm [98]. Figure 11 shows the electrical conductivity behavior with increase in wt. % of CNTs in the composite. After the study of both electrical and mechanical properties of the composite films, the collective study of the CNT-polymer based sensor is required. This analysis can be done using finite element analysis.

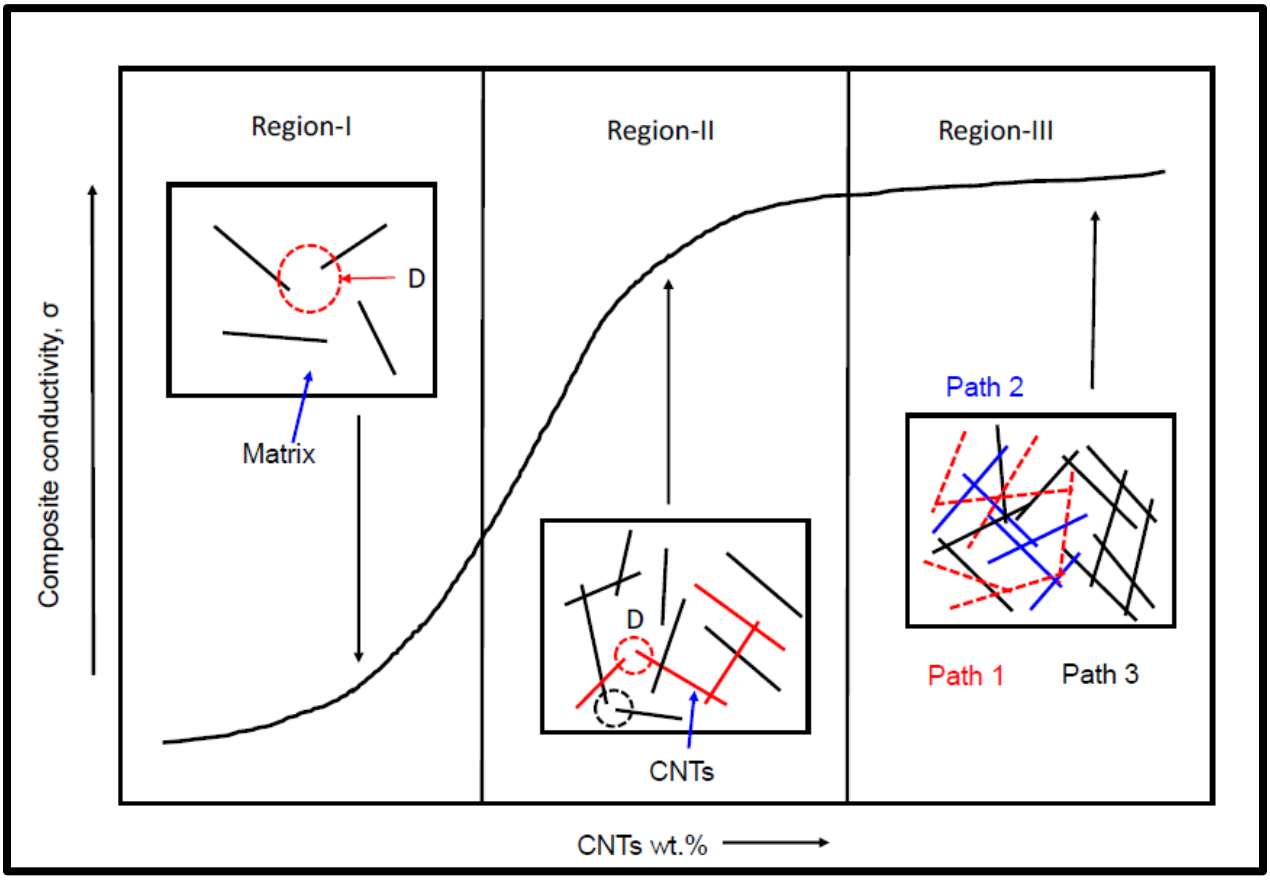

Figure 11: Variation of electrical conductivity and evolution of percolating networks with increase in CNT wt .% [97]

2.14 Finite element modeling of strain gauges

Nano structure have taken a special interest because of their material property advantages. Specifically, CNT-polymer composites have provided satisfactory results in terms of strength, stiffness, flexibility and conductivity. To further understand this topic and the underlying relationships, studies are extended to continuum mechanics and molecular dynamics approaches or modelling and analyzing of CNT-polymer composites. However, this research is focused on continuum mechanics approach. Despite of various studies conducted on interfacial bonding in CNT-polymer composites, there is a lack of quantitative understanding of the load transfer efficiencies. Some of the issues include, stress concentration, axial stress profile, interfacial shear stress distribution etc. Continuum mechanics approach was used to model CNT-based composite sensor, which assumes that there is a perfect covalent bond between polymer matrix and CNTs, CNTs are uniformly distributed in the polymer matrix, composite material/sensor is attached strongly to the structure which is to be studied etc. Considerable research is yet to be done in dealing with analytical and experimental methods to address this kind of Multiscale and Multiphysics problems. For computational simplicity, it is ideally considered to couple CNT-polymer composite with electromechanical models. McCullough outlines the macroscopic behavior of polymer composites [99], [100]. However, for CNT-polymer composites, it has become an issue when dealing with SWCNTs and MWCNTs in defining the number of layers and its diameter, which breaks the rules and regulations of continuum modeling. Still, there are limited studies and researches taking place in addressing these topics.

Representative volume element (RVE) analysis estimates the properties of CNT-polymer composites. Lot of research was done in this area to predict the properties [101], [102]. This RVE assumes a single CNT is embedded inside the polymer matrix, the interface bonding is ideally strong and there is perfect strain transfer to the CNTs. The CNTs can be defined as shells or tubes. Figure 12 shows the three RVEs commonly used.

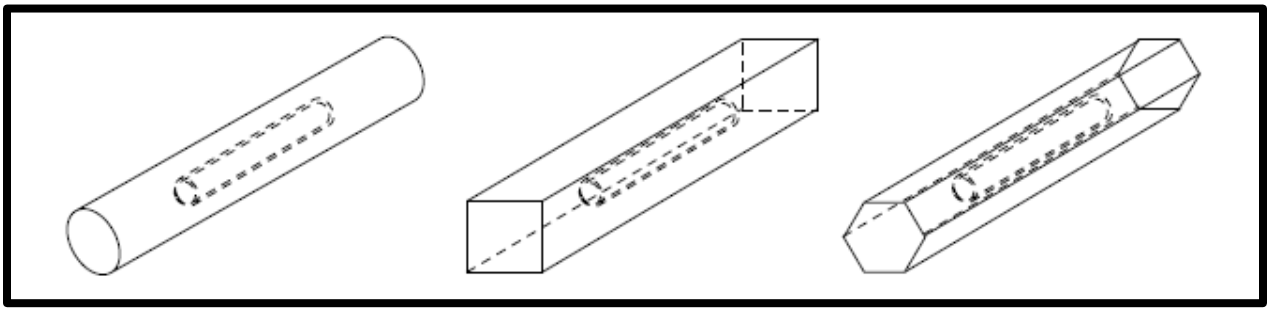

Figure 12: Cylindrical RVE, Square RVE, Hexagonal RVE [101]

Continuum mechanics approach is the feasible approach some conducting preliminary studies of CNT-polymer composite materials. It is proposed that 3-D elasticity models should be built to study stress and load carrying capabilities instead of beam or shell models[103]. CNTs will be in different sizes and different orientations when they are dispersed in the polymer matrix. They may be single wall or multiwall, straight or bend etc. because their distribution is random. Hence

the study would be quite complicated. To overcome this, RVE concept was assumed with the assumptions mentioned above. Computations are done by defining the CNT properties to the inner body and polymer properties to the surrounding matrix.

RVE concept gives the behavior of a single CNT embedded in polymer matrix. The approximation of the entire composite, film or sensor properties fabricated from it would be a tough task. Hence, to do that, the complete sensor model was built, defined its properties from the literature and performed analysis of the senor. This kind of work was published by few groups in the literature [104]–[108]. The extension of this research was done by our group and is first time reporting in the literature on COMSOL Multiphysics platform. Figure 13 shows the finite element analysis computations of stress, strain of a composite film, for a particular applied load condition, from [108].

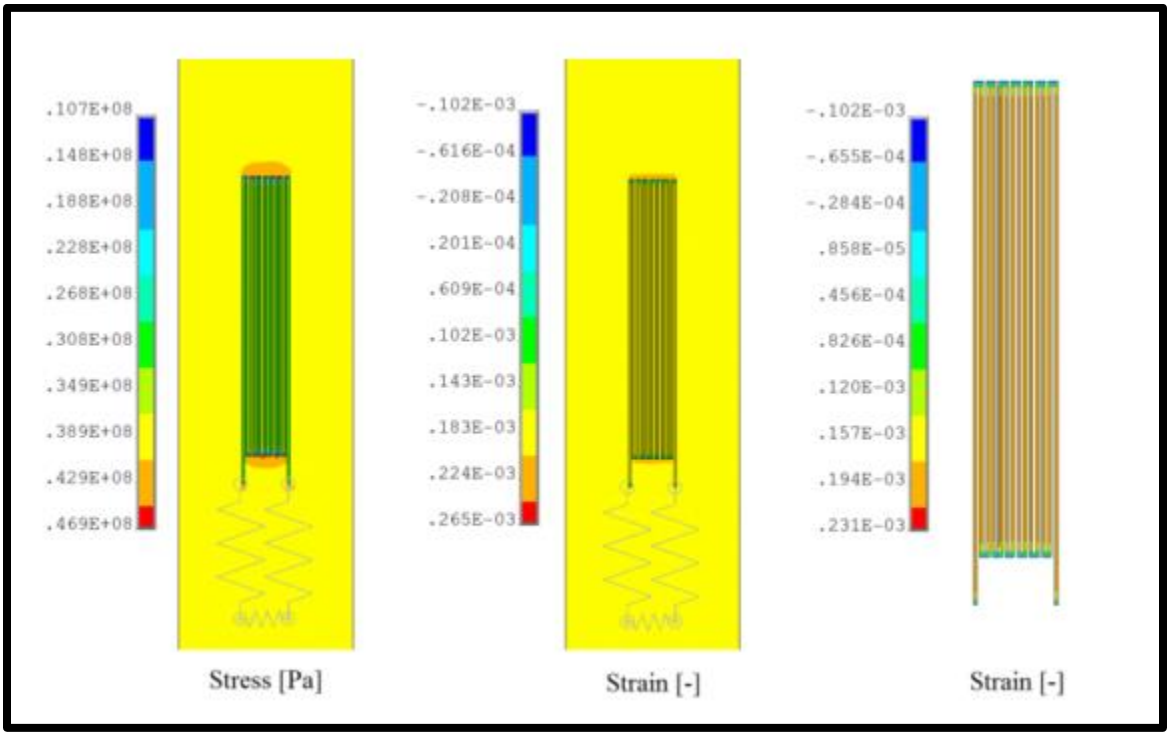

Figure 13: Stress, strain analysis of a composite film [108]

2.15 Summary

As discussed in this chapter so far, CNTs are the strongest materials that were discovered till date. They possess exceptional mechanical. Electrical and electromechanical properties. These CNTs can be produced using different techniques like arc discharge method, laser ablation

method and plasma enhanced chemical vapor deposition method. PECVD was discussed in detail because this technique was used in this research. This chapter also summarizes on the growth of metallic thin films using physical vapor deposition technique. The existing literature on CNT-polymer composites and their applications, CNT-polymer based sensors and their limitation were briefly discussed. This chapter also focused on the existing literature of finite element analysis of strain gauges.

In the next chapter, experimental techniques and characterization techniques used in this research are discussed briefly.

3 EXPERIMENTAL TECHNIQUES

In the previous chapter, the existing literature on CNTs, CNT composites and their sensors and finite elemental analysis of the strain gauges was presented. In this chapter, experimental techniques like physical vapor deposition, plasma enhanced chemical vapor deposition, spin coating techniques are discussed briefly. This chapter also presents the characterization techniques like, scanning electron microscopy, Raman spectroscopy, Rutherford backscattering spectroscopy and 4-probe method.

Carbon nanotube based films are grown using two processes. They are growth of CNT based films using MWCVD technique and preparation of CNT-polymer nanocomposites. MWCVD technique requires a catalyst layer grown deposited on the substrate. This deposition of metallic catalyst thin films is done by physical vapor deposition technique.

3.1 Catalyst thin film deposition

Catalyst thin film deposition is done on the substrates using sputtering or thermal evaporation. Sputtering is a process in which particles are ejected from a metal target (mostly) by supplying energy to the target or by bombarding the solid surface with high energy particles mostly argon or krypton. The electron from the target metal gets ejected when the kinetic energy of incoming particles is higher than surface binding energy. This technique is mostly used for thin-film deposition, etching, and analytical techniques. There are other techniques, as well, for thin film deposition[109]–[112]. DC diode system is simple in construction and operation compared to other techniques. One electrode is a cathode, and one electrode is an anode. The deposition takes place at high vacuum conditions i.e. around 10^{-2} to 10^{-4} torr range. Voltage is applied between the electrodes and a glow discharge is created which generates the gas ions. These gas ions are accelerated towards the cathode and sputter the target resulting in thin film deposition. The deposition time, current supplied, depends on the thickness of the thin film required. Figure 14 depicts the sputtering process taking place inside the vacuum chamber and figure 15 shows PVD 75, Kurt J. Lesker machine which is, present at Western Michigan University, used in this research to deposit metallic thin films. After depositing thin film catalyst layers, CNTs are grown using PECVD technique.

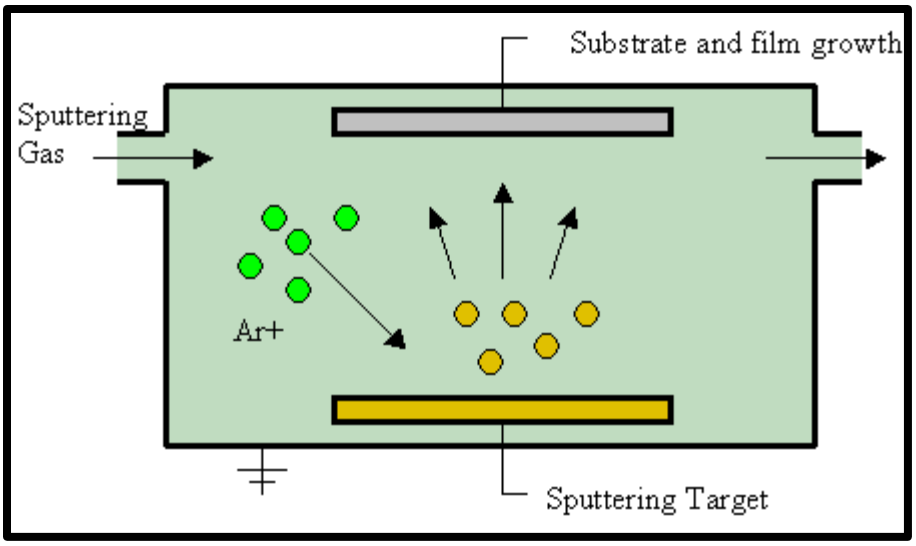

Figure 14: Sputtering process taking place inside the chamber

Figure 15: A picture of PVD 75, Kurt J. Lesker machine

3.2 Plasma Enhanced Chemical Vapor Deposition (PECVD)

PECVD technique is widely used to grown CNT films on substrates using metallic thin films as catalysts. Depending on the power source, PECVD is divided into microwave wave chemical vapor deposition (MWCVD) and Radio frequency chemical vapor deposition (RFCVD). Due to high frequency and high energy applications, MWCVD is mostly used to grow CNT based films. Thermal decomposition or catalysis enhanced thermal cracking of a gaseous carbon source is known as chemical vapor deposition (CVD). This is used to produce carbon nanofilaments. These nanofilaments are used to produce carbon fibers, which are called as vapor-grown carbon fibers. Production of CNT's or diamond-like carbons (DLC's) or graphene etc. using the CVD process involves the decomposition of hydrocarbon gases, frequently acetylene, methane, ethylene, and benzene etc., mixed with inert gas, mostly hydrogen or argon, onto the catalyst metallic particles which are deposited on the substrate, using magnetron sputtering or spraying the metal particles. The chemical reactions that are taking place inside the chamber are thermodynamically endothermic. Hence the reactions can be controlled by controlling the input energy. Heat is used as energy source in the CVD process at high temperatures. But if needs to be done at low temperatures, they either photons or plasma sources should be used. The reaction is chemically defined as

$$C_xH_y \longrightarrow xC + (y/2)\, H_2.$$

Carbon monoxide can also be used instead of hydrocarbons. The reaction is then chemically known as catalysis-enhanced disproportionation, which is also known as Boudouard equilibrium[113].

$$2CO \longleftrightarrow C + CO_2.$$

The commonly used catalyst layers are transition metals like Fe, Co, Ni etc. Catalyst has a significant influence on the properties of the resulting materials[114]. This process takes place around higher temperatures ranging between 600°C-1000°C (800-1300K). These temperatures are low compared to arc discharge (3000- 4000K) and laser ablation processes (1000-6000K). This low-temperature conditions are advantageous for producing MWCNT's regarding graphitic particles and like amorphous carbon. The properties of CNT's produced are sensitive to the conditions and materials under which the process is taking place. CNT's produced in this process are longer (few micrometers) compared to the other processes. Vertically aligned carbon nanotubes[115] and CNT's in large arrays[116] can be grown easily in suitable experimental conditions. CNT's may contain structural defects due to low-temperature experimental conditions, and this prevents them from structural rearrangements. However, these defects can be overcome by inert gas environments or heat treatments. The diameter of SWCNT's, produced in this process, possess less diameter compared to the other process dimensions. In commercial scale, CNT's can be mass produced with low cost on large-scale by performing CVD in fluidized bed reactor[117]. Figure 16 shows the schematic of the Plasma enhanced microwave chemical

vapor deposition system and figure 17 shows the system present at Western Michigan University and used for this Thesis.

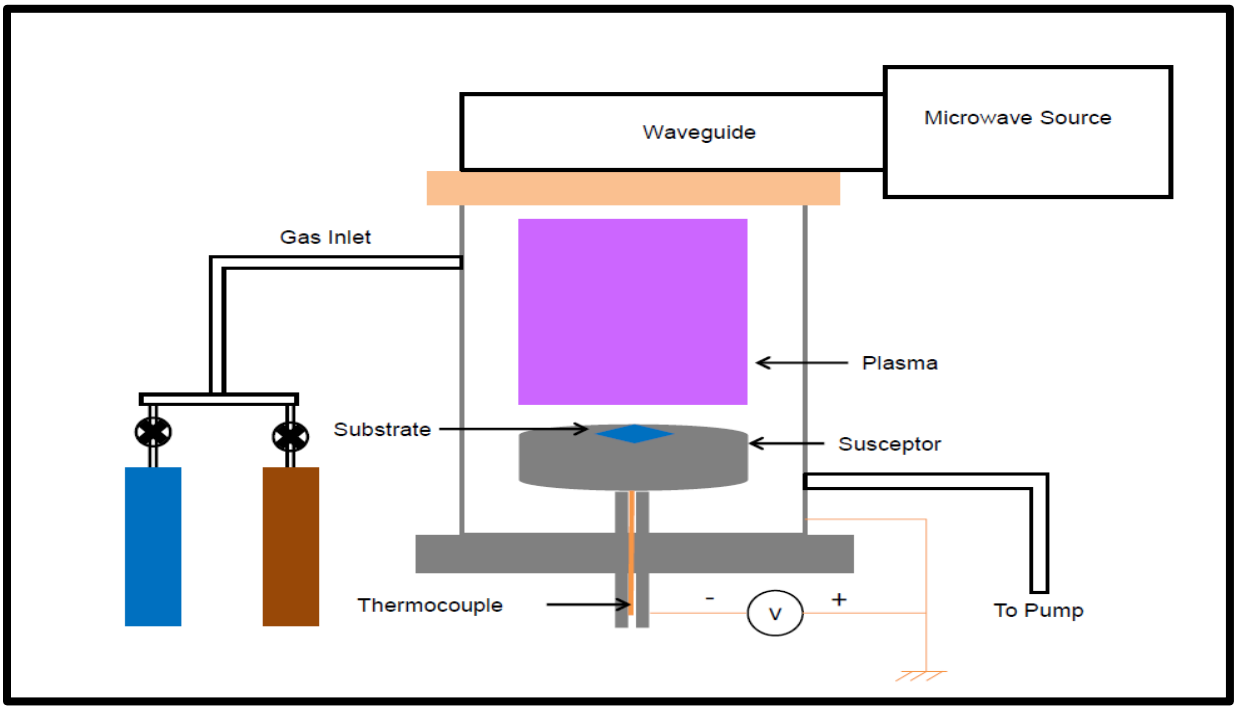

Figure 16: Schematic of plasma enhanced microwave chemical vapor deposition system [97]

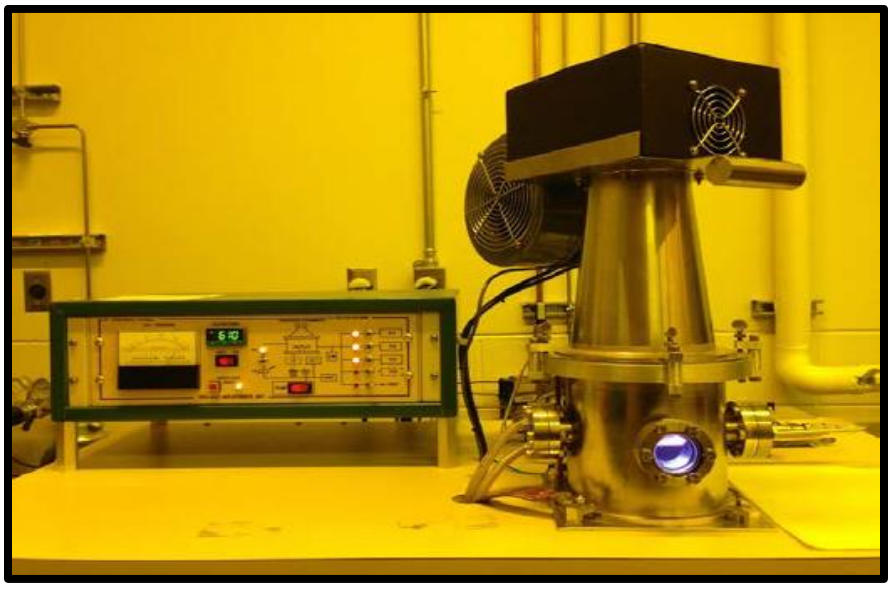

Figure 17: Microwave Chemical Vapor Deposition system at Western Michigan University

The catalyst layers are initially treated with inert gases like H_2 or argon, to reduce salts and oxides of metal compounds. This usually taken at high temperatures around 600-800°C. Then the power is coupled to plasma, and the plasma treatment forms on the nano catalytic islands. The plasma treatment duration depends on the properties of the CNT's required. This plasma energy helps in performing the experiment at low temperature conditions. It also initiates the chemical reactions by forming chemically active species and supply the energy to the substrate to enhance particle migration, nucleation and heterogeneous kinetics. Hence the name PECVD. This technique is used since 1960s to synthesize dielectric films at low temperature conditions. The chemistry of this process was greatly discussed in the literature[118], [119]. Then the hydrocarbon gas along with the inert gas is sent into the chamber, with plasma present inside the chamber. Now the gases are at high temperature and present above the catalyst layer present on the substrate. The pyrolysis action takes place on the catalyst layer which involves a) transportation of precursor gases, b) producing reactive and byproduct gases in the reaction zone, c) transportation and adsorption of reactants on the substrate surface, d) diffusion, nucleation and surface chemical reactions for film growth and finally e) desorption and transport of residuals away from reaction zone. The flow rate of the gases and deposition times should be calibrated from machine to machine.

CNT based films are also deposited by synthesizing CNT-polymer based nanocomposites. After synthesis of composites, they are deposited on the substrates using spin coating technique. Substrates are cleaned with deionized water and treated with ultra-violet ozone plasma treatment to increase the surface energy.

3.3 Ultra-violet Ozone plasma treatment (UVO)

The hydrocarbon contamination on the surface of the substrates are excited or dissociated by the absorption of short UV radiation. Atomic oxygen, which is generated by dissociating molecular oxygen at 184.9nm UV radiation, is combined with an oxygen molecule to form ozone molecules which are further dissociated by 253.7nm UV radiation. The excited or dissociated molecules react with this high-energy oxygen to form volatile molecules which desorb from the surface. Radicals like *OH, COO* and CO* also form on the surface of the substrate. Adhesion properties of the substrate are enhanced by increasing these polar groups which are formed because of oxidation of the surface. Jelight UVO cleaner-144AX, at our university, was used for our experiment. Figure 18 shows the machine used in this research. After treating the substrates with UVO, they are taken into clean room and CNT-polymer thin films are deposited on the substrates using spin coating technique.

Figure 18: Jelight UVO cleaner-144AX used in this research

3.4 Spin coating

To produce thin, uniform films on these UVO treated substrates; spin coater is used. Depending on the thickness of the required thin film, few drops of the nanocomposite solution were dropped on the surface of the substrate and accelerated to required rotation speed. The excess solution flows out of the substrate because of centrifugal force. The films tend to become thin further when the internal pressure forces reached equilibrium. The final film tends to be much thinner after placing the spin coated substrate in the hot oven at desired temperature and evaporating the solvent. Depending on the required thin film thickness, rotation speeds and times should be calibrated. They can be set used a controller which is attached to this device. Figure 19 shows the spin coater used in this research. Once the CNT based films are deposited using MWCVD technique or nanocomposite synthesis technique, the properties of these specimens are studied using various characterization techniques.

Figure 19: Laurell technologies WS-400-6NPP-LITE spin coater

3.5 Scanning Electron Microscopy (SEM)

In this technique, focused beam of electrons scan the specimen and produces image on the screen. The electron beam interacts with the specimen atoms and produce compositional and topographical information. This technique is usually used to study objects in micro and nano scale size. It provides information with great accuracy of 1nm. The analysis is carried out in a vacuum chamber where there is less effect of foreign material in the analysis. Depending on the sample specifications, the atmosphere of the experimental conditions can be decided. There are different modes and different kind of analysis present in one SEM machine and one of the mostly used mode is secondary electrons detection which are excited by electron beam.[120] By detecting these electrons using a special detector and raster scanning them, an image is produced on the monitor with required information. Figure 20 shows the basic construction of a SEM machine.

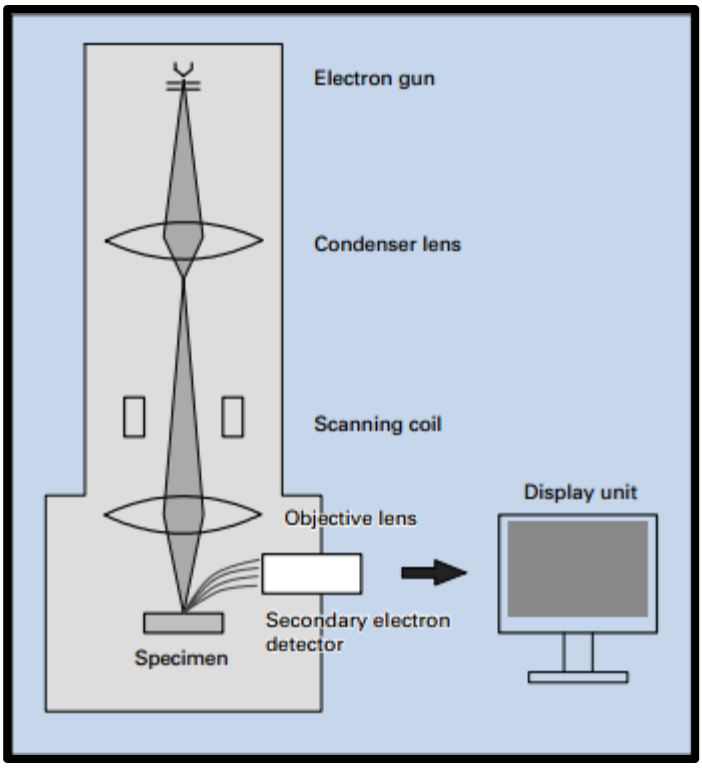

Figure 20: Basic construction of Scanning Electron Microscopy [121]

SEM construction basically requires an electron optical system, specimen stage, secondary electron detector, vacuum chamber and image display unit [122], [123]. Every SEM has similar construction model with few add-ons. An electron gun is used to send a beam of electron down to the specimen, which is fixed inside the vacuum chamber. To focus the specimen, a series of electromagnets are used. Glass lenses, which are found in regular microscopes, cannot be used because electron beam wont go through glass but electrons have a charge which means they are influenced by magnetic fields. So the condenser lenses, shown in above picture, are electromagnets and they are used to focus the electrons finally on the sample. The electron gun is generally a thermoionic electron gun which gives a bunch of electrons when heated. We generally use 15,000-30,000 volts to supply to the electron gun.

Negatively charged electrons are attracted towards the anode, so they head down in the direction, but these anodes has a holes built through them, which means they pass through the anode continously. Also the specimen stage has a positive charge, which attracts the electrons, passing through the anode hole towards them. Thus the electrons travel in downward direction and hits the sample. There are two type of electrons that come off from this.in one case we obtain secondary electrons and in the other case we obtain the backscattered electrons.

Secondary electrons are obtained when the electron beam comes down and hits the atoms of the specimen, those atoms absorb the energy and release their own electrons which are known as secondary electrons. There is a positively charged secondary electron detector, which is around 300volts to attract these positively charged secondary electrons. They detect low energy secondary electrons (<50eV)Once these electrons come in to the Faraday cage which is positively charged, they hit the detector. The detector uses this information to form an image on the display unit.

Backscattered electrons are the atoms refelected from the surface or from deeper down the specimen. We have a second detector to detect these backscattered electrons. They are usually high energy electrons. These electrons are good to obtain surface features. The electrons travelling deep into the specimen, actually don't come off but they give of X-rays. These electrons are called are primary electrons or absorbed electrons. These X-rays are used to obtain the elemental analysis of the sample[124] [125][126].

3.6 Raman Spectroscopy

This is a light scattering technique which was introduced by Sir.C.V. Raman in early 20th century.According to him, sunlight interacted with materials to produce a characteristic pattern. When light of certain frequency, irradiates a sample, the scattered light which comes out seems to have a series of frequencies. The scattered light has been modulated over the incident light frequencies, by some additional or depleted frequencies. This is known as Raman effect. This work was awarded a nobel prize in 1930, which stands with his name as Raman Spectroscopy. This is a non-destructive technique used to observe vibrational, rotational and other low frequency modes in a system which is used to determine the molecular structure of the object depending on how the light is reflected[127].

A laser operating in visible, infrared and UV region can be used for this process. When this laser interacts with the specimen, vibrations or excitations occur inside the system. This changes the energy of the incident laser or light. This energy shift is used to study about vibrations and rotations of the system. Rayleigh scattering, which is elastic scattering, of photons are shifted out. But there are weak inealstic Raman photons which are diverted through a detector. They are weak because of inelastic photons. Hence these weak signals are separated from Rayleigh scattering by passing them through a series of experimental setup which consist of multiple dispersion stages. Figure 21 shows the schematic of line diagram of Raman spectrometer.

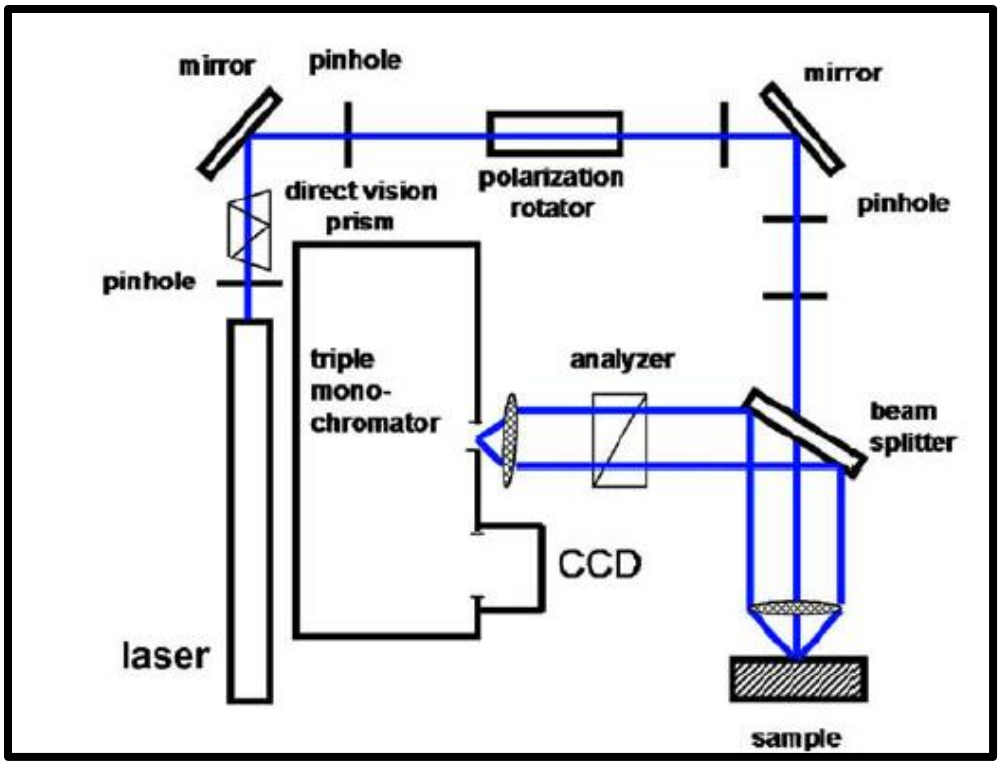

Figure 21: Line diagram of Raman spectrometer [97]

If the molecule, which is subjected to light, reaches higher energy than the initial stage, then the emitted photons shift to a low energy region. This frequency shift is known as stokes shift. If the molecules looses its energy, then that energy will be gained by emitted photons. These photons are shifted to a high frequency region and this frequency shift is known as anti-stokes shift. The Rayleigh photons have same energy as the incident beam. If the initial frequency is assumed to be ν_0 and ν_m is the vibrational frequency of the molecule. Then all the $\nu_0+\nu_M$ and $\nu_0-\nu_M$ represent anti-stokes and stokes line respectively whereas Rayleigh photos have same frequency ν_0.[128],[129], [130]which is shown in figure 22.

For the experimental purpose, a laser beam of ν_0 frequency was chosen. The signals from stokes line (S) are much stronger than anti-stokes lines (A). According to Maxwell-Boltzmann distribution law, which states that population of particles at ground state are greater than vibrational states. Because both stokes and anti-stokes lines give the same information about vibrational state of molecules, stokes side of the spectrum is measured.

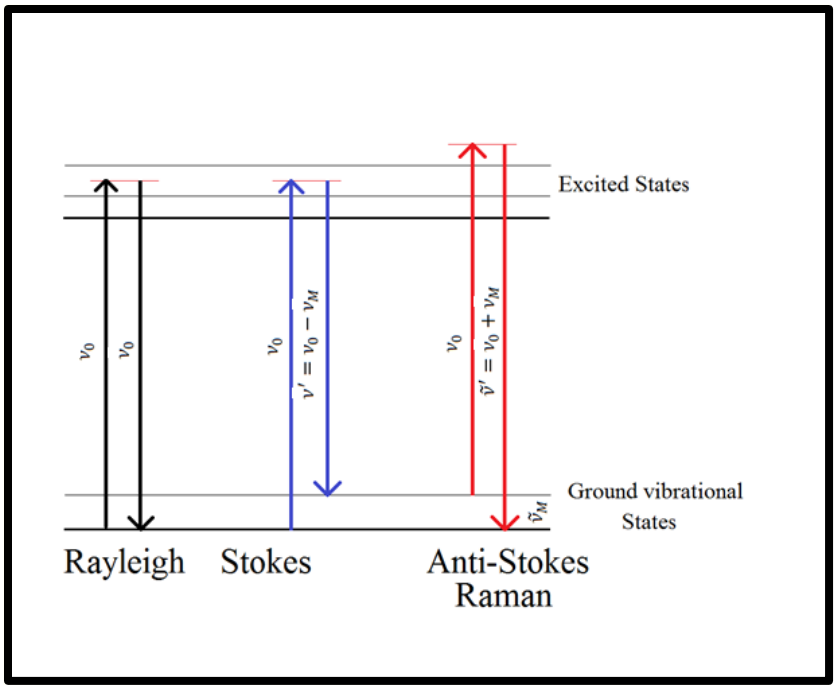

Figure 22: Comparison of frequency shifts for Rayleigh scattering, stokes and anti-stokes

3.7 Rutherford Backscattering Spectrometry (RBS)

RBS is an analytical technique where high energy ions are scattered from atomic nuclei in a sample. The energy of the back-scattered ions can be measured to give information on sample elemental composition, thin film thickness, stoichomtery etc. as a function of depth. [131]–[133]. Incident and backscattered energies are explained by law of conservation of energy and momentum which is given by [134].

$$E_1 / E_0 = K = [(M_2^2 - M_1^2 \sin^2\theta)^{1/2} + M_1 \cos\theta / M_1 + M_2]^2$$

Where, E_1 and E_0 are the energies of backscattered and incident particles respectively, K is kinematic factor, M_1 is mass of incident particle and M_2 is mass of target particle and θ is the angle in which the incident ion scattered.

According to history, Geiger-Marsden experiment was carried out in the direction on Earnest Rutherford. This states that, electrons are well distributed in a large positive charge. This is also called as plum-pudding model. To test this model, they would shoot alpha particles through a thin foil and they placed a detector behind it. The alpha particle being massive would pass through the foil and would be detected behind. He, then, wanted to place the detector infront of the sample, at an angle, assuming that there should be no alpha particles on the front side. But surprisingly they noticed few counts[135], [136]. Then they planned to modify the model. Instead of having the charge widely distributed, the positive charge be present at the center, nucleus, and assume that the electrons are revolving around the nucleus like the planets revolve

around around the sun. this was the planetory model. RBS was first used as a material analysis method in 1957 [135].

The exeperimental setup consist of a vacuum chamber in which the specimen is placed. Alpha particle beams,usually, are sent and focussed on the specimen. They are usually around 1 or 2 MeV. They go inside the material and in some cases they travel close to the nucleus of the atom.At this high energy when the beam hits the target material atoms, some of the incident ions are absorbed and some of the ions are backscattered. The energy of the backscattered ions gives the information about the target atoms and hence film thickness is determined from width of peaks in RBS spectrum. A detector is placed to receive and count the reflected or back scattered alpha particle. The analysis of particles coming into the detector in energy and number of counts, that is known as RBS spectrum. The beam size can be varied from 1-3mm, the sample should be flat and the it can be rotated inside. The backscattered spectra was collected using a detector amd the data is utilized by SIMNRA software. Figure 23 shows the 6MeV Van de Graaff accelerator in physics department at WMU.

Figure 23: 6MeV Van de Graaff accelerator

3.8 4-probe method

This technique is used to study the resistvity of a conductor or a semi conductor. It has 4-points or 4 terminals which are evenly spaced and are linearly arranged. They are pressed against the sample. A high impedance source is attached to this setup and it supplies the current which flows

through the outer two probes and through the sample. It has a voltmeter across the two interior probes that are measuring the corresponding voltage to determine resistivity. Figure 24 shows the schematic of a linear 4-probe arrangement [137]–[139].

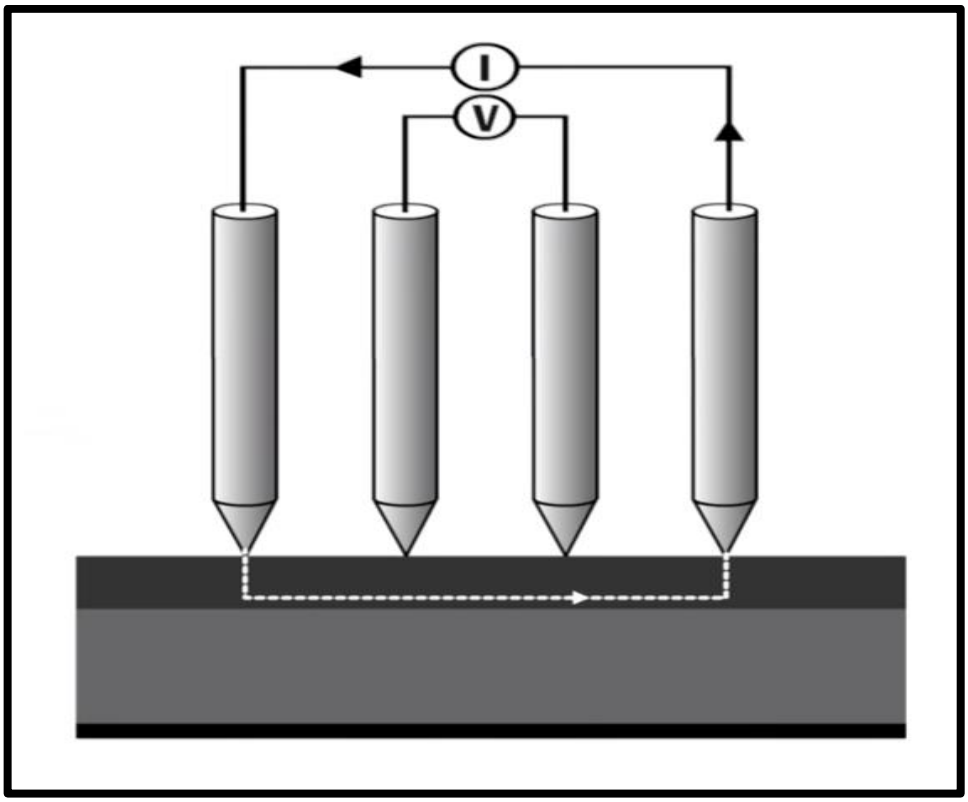

Figure 24: Schematic of a linear 4-probe arrangement

Resistivity of the semiconductor having the thickness 'w' is computed as

$$\rho = \rho_0 / f\ (\frac{W}{S})$$

where,w is thickness of semi conductor, s is spacing between probes in meters, ρ is resistivity of sample and ρ_0 is the resistivity of the material which is computed from

$$\rho_0 = \frac{V(2\pi s)}{I}$$

where V is floating potential difference between inner probes in volts, I is current through the outer pair of probes in amperes, s is spacing between probes in meters. $f\ (\frac{W}{S})$ values are given in the table 1. This technique supplies currents to the outprobes and measures the voltage across the inner probes and displays the corresponding resistance values of the specimen.

Table 1: Computing f (W/S) values from w/s ratio[140]

W/S	$f\ (\frac{W}{S})$
0.100	13.863
0.141	9.704
0.200	6.931
0.330	4.159
0.500	2.780
1.000	1.504
1.414	1.223
2.000	1.093
3.333	1.0228
5.000	1.0070
10.000	1.00045

3.9 Summary

In this chapter, experimental techniques like physical vapor deposition, to deposit metallic thin films, plasma enhanced chemical vapor deposition, to grow CNTs, spin coating technique, to deposit thin films of CNT-polymer composites are discussed briefly. This chapter discussed briefly on characterization techniques like, scanning electron microscopy, to study the surface morphology, Raman spectroscopy, to study the molecular configuration, Rutherford backscattering spectroscopy, to study the thickness of thin films and 4-probe method to study the electrical conducting nature of CNT polymer composites.

In the next chapter, the growth of CNTs using PECVD and synthesis of CNT-polymer composite films are discussed.

4 SAMPLE PREPARATION

In the previous chapter, experimental and characterization techniques are briefly summarized. In this chapter, the details of all the materials used in this research are reported. This chapter also focusses on the physical vapor deposition of metallic thin films, synthesis of CNTs using PECVD technique, synthesis of CNT-polyurethane composites and fabrication of CNT-polyurethane composites using spin coating technique.

4.1 Materials used

4.1.1 Silicon dioxide substrates

99.99% pure SiO_2 substrates are purchased from Sigma-Aldrich (USA). Its density is 2.6 g/mL at 25°C (lit.), transition temperature is 573.1°C and specific heat is 0.18cal/g.

4.1.2 Carbon nanotubes

Multi-wall carbon nanotubes are purchased from Sigma-Aldrich (USA). The specifications of the CNTs provided by the manufacturer are Bulk density is about 0.22 g/cm^3, the outer diameter of the nanotubes are about 6-10nm and length of 5μm.

4.1.3 Polymer

Selectophore polyurethane (PU) from Sigma-Aldrich is used as the polymer matrix. The specifications of the PU provided by the manufacturer are specific gravity 1.04 g/cc, flexural modulus is 1000psi, mold shrinkage is 0.008 to 0.012 in/in, the melting point is 360°F, Tensile strength at break is 38.9MPa and elongation at break are 307%.

4.1.4 Dispersion medium

1-Methyl-2-pyrrolidinone (NMP) from Sigma-Aldrich is used to disperse CNTs and polymer. Its vapor density is 3.4 (vs air), vapor pressure is 0.29mmHg (@20°C) and 0.99mmHg (@40°C), auto ignition temperature is 518°F, boiling point is 202°C (lit.) and density is 1.028 g/mL at 25°C.

4.2 Catalyst thin film deposition

Titanium and nickel thin films are grown on Silicon substrates with 100nm of Silicon dioxide barrier layer. Titanium is used as an adhesion promoting layer and nickel is used as a catalyst layer to grown CNTs. These thin films are grown using physical vapor deposition (PVD) technique.

Silicon with SiO_2 layers are cleaned with deionized water, dried and then loaded into the vacuum chamber of the PVD machine. The system is initially started with rotary vacuum pump. Later turbo pump is used to vacuum chamber. High vacuum, around 1 x 10^{-5} torr is achieved. Argon gas is used in this process.

High-purity titanium (99.9%) target was evaporated by DC magnetron sputtering and DC was set to 300mA. The argon pressure is set to 4 x 10^{-2} torr inside the vacuum chamber. Titanium is deposited for 2 minutes which yielded a thickness of around 2nm. Then high purity nickel (99.9%) is deposited on the top of titanium thin film for 1 minute which yielded a thinness of 2.5- 3.5nm. Rutherford backscattering spectrometry (RBS) was used to find the thickness of the thin films.

4.3 Carbon nanotube synthesis

A microwave plasma enhanced chemical vapor deposition (Tekvac PECVD-60M) was used to grow CNTs. It has a frequency of 2.45GHz and 600W power respectively. CNTs are grown around 600°C. CNTs are synthesized in three major steps. They are annealing, plasma treatment and growth.

Hydrogen annealing, at high temperatures, is done to remove the oxide layer formed on the catalyst layer. 40 standard cubic centimeter (sccm). Plasma step is the crucial step in determining the properties of the resultant CNTs. The nickel thin film is broken down into nano-islands during this process. Plasma along with hydrogen treats the catalytic thin film during this step and forms nano-islands which act like seeds to grow CNTs. The length and diameter of CNTs depends on the diameter of these nickel nanoislands. Because the process is at 600°C, there is no worry about nickel oxidation. The chamber here is around 0.1 to 0.4 torr. The growth of CNTs is followed immediately. Hydrocarbon gas, methane, is released into the chamber along with a precursor gas, Ar. This argon splits the hydrocarbon gas into hydrogen and carbon. The carbon here reacts with the nickel nano islands forming CNTs using tip growth or base growth models [141]. The gas flow rates are kept constant and they are argon 40, hydrogen 40 and methane 5 sccm respectively. The annealing, plasma treatment and growth time parameters were varied and presented in the table 2.

Table 2: Summary of the experimental parameters varied for the growth of CNTs on SiO2 substrate

Sample Name	Annealing Time (in min.)	Plasma treatment Time (in min.)	Growth Time (in min.)
B	60	30	30
C	60	20	30
D	60	10	30
F	20	30	30
G	10	30	30
H	30	30	30

I	40	30	30
J	60	30	10
K	60	30	40
L	60	40	30

4.4 Synthesis of CNT-polymer nanocomposite

Few trial and error experiments were conducted to observe the solubility of polyurethane polymer matrix and dispersion of CNTs in various kinds of surfactants. It was observed that dispersibility of CNTs and solubility of polyurethane can be achieved in 1-Methyl-2-pyrrolidinone (NMP).

Polyurethane is added to NMP and magnetically stirred at 50°C for 48 hours. This is done under keen observation to make sure that the polymer is completely dissolved. For every 1ml of NMP, 40mg of polyurethane is added. Then known quantities of CNTs are added to the above solution and stirred for 6hours at room temperature. This forms a CNT-polyurethane composite solution. The CNTs in this solution seems to be agglomerated. Hence ultrasonication is done for 30minutes to separate the clusters of CNTs into individual CNTs. The CNTs are added in varying quantities. We varied them like 1, 3, 5, 6.5 and 8wt. % of CNT-polymer solutions. This completes the CNT polymer composite synthesis process. Figure 25 gives the schematic of the composite synthesis process.

After the synthesis of composite, thin films of the composite are fabricated on the glass substrates. Glass substrates are initially cleaned with DI water, to remove the foreign material, dust etc. They are then treated with UVO for 20minutes. Refer section 3.3 to refer UVO treatment. After completing the UVO process, the substrates are transferred to the clean room. They are placed on the spinner and spun at 500rpm for 30seconds, which was found to be optimum. They are then heated in the oven to cure. The experimental parameters that were varied during this process are UVO exposure time which is varied between 0-14minutes, CNT loading into the composite which ranged from 1 to 8wt. % of CNT-polymer solutions, spinning speeds which varied from 350, 500, 750 and 1000 rpm at constant time i.e. 30 seconds, number of layers of deposition i.e. single layer of double layer, post deposition annealing temperatures i.e. 80, 110, 130°C for 10, 30 and 60 minutes. The results and discussions were given in the last chapter.

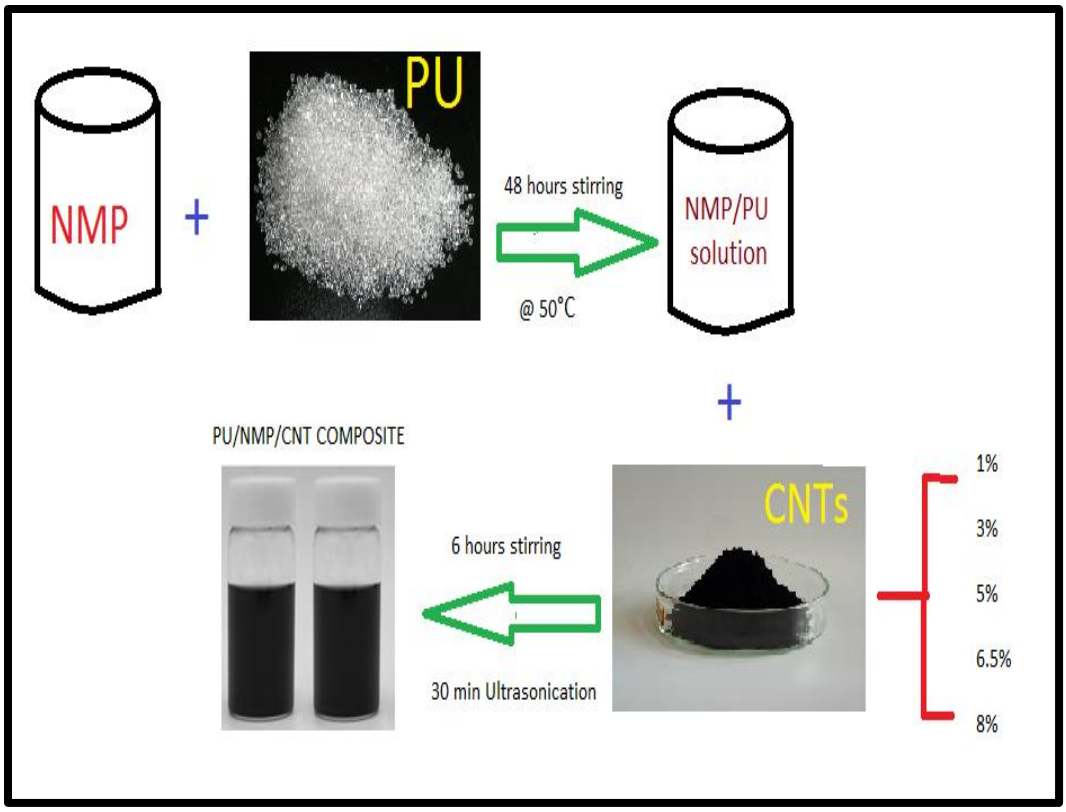

Figure 25: Schematic of synthesis of CNT-polyurethane composite process

4.5 Summary

In this chapter, physical vapor deposition of metallic thin films, synthesis of CNTs using PECVD technique, synthesis of CNT-polyurethane composites and fabrication of CNT-polyurethane composites using spin coating technique is briefly summarized. Next chapter focuses on the design and fabrication of strain sensor.

5 DESIGN AND FABRICATION OF SENSOR

In the previous chapter, the sample preparation process and growth of CNTs using PECVD technique and synthesis of CNT-polymer composite was discussed. This chapter will focus on the concept of strain sensor and fabrication of strain sensor using optical lithography technique. The lithography steps are explained in detail stating the importance of each step involved in the process.

Deposition of CNT based composite films and optimization of the characteristics has been one of the important steps in the development of devices. Among many of such devices that could show promising characteristics, strain sensors are observed to be one of the important class of sensors that can exploit excellent electrical, mechanical and electromechanical properties of both CNTs and CNT based composites.

5.1 Strain sensor model

A strain sensor design is important for fabrication because, the total gauge length of the sensor is folded into curls and fitted into a small area, to make the sensor compact and highly sensitive at the same time. It is designed in such a way that it experiences change in resistance, when a structure, on which the sensor is placed, is subjected to mechanical loading. This design consist of contact pads for depositing electrodes. Figure 26 shows the nomenclature/ terminology of the strain sensor. One of such designs is adopted for our experimental purpose.

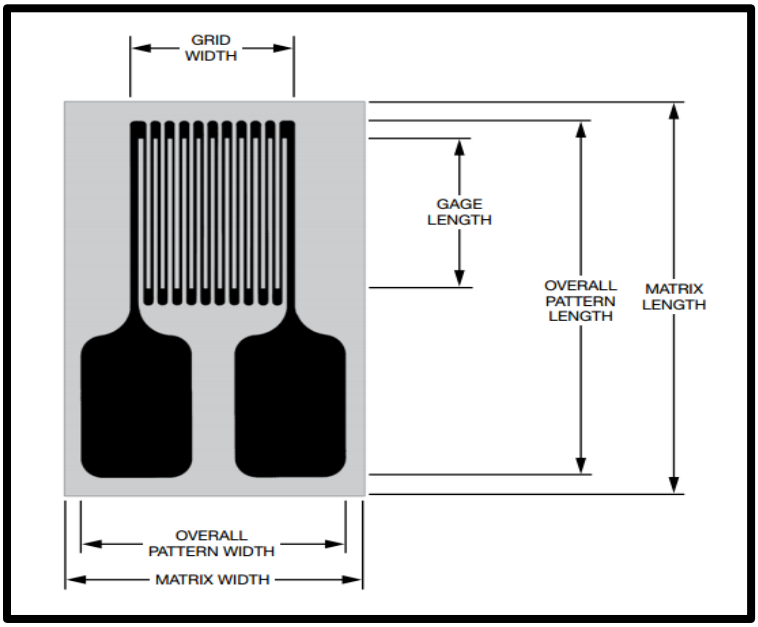

Figure 26: Nomenclature used in strain gauge fabrication

Based on sensor design and strain measurement criteria, metallic strain gauges with gauge factor of 2 and contact resistance of 120Ω are obtained. The dimensions of the sensor that were

purchased from Micro Measurements, USA is shown in figure 27. In this picture all the dimensional details of the strain sensor that was purchased are given. Then a strain gauge for our experimental purpose if fabricated from CNT nanocomposite using Optical lithography (Photo lithography).

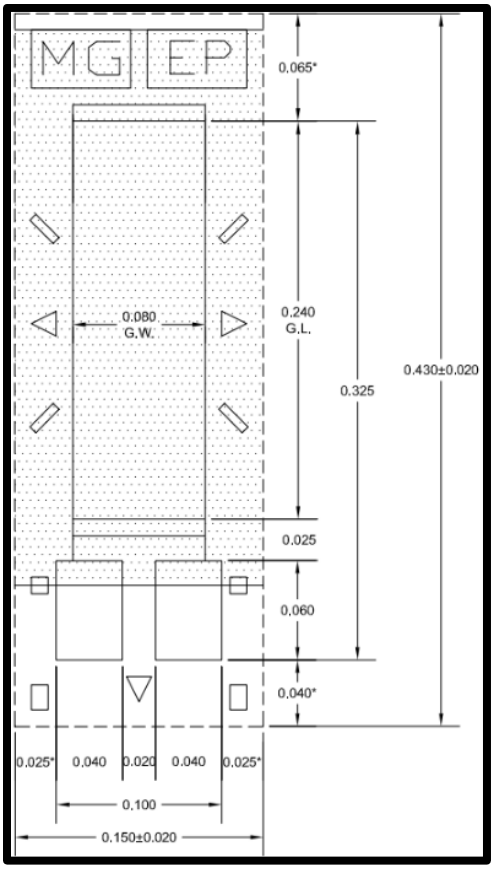

Figure 27: Conventional metal strain gauge used in our experiment

5.2 Fabrication of Strain gauge using Photo-Lithography

Photolithography, often known as optical or UV lithography, is a process of transferring the image of pattern from a photo mask on to a photoresist which is spun on the substrate. Lithographic steps are designed to obtain the final structure, CNT-composite based strain sensor.

The strain sensor structures were fabricated silicon substrate. The complete lithography process was performed in class 100 clean room at College of Engineering and Applied Science, Western Michigan University. The photolithography process to fabricate this CNT-polymer composite strain gauge is given in a 2-D schematic in the figure and will be discussed in detail in the following sections.

1. Substrate cleaning
2. Sputtering of titanium and nickel thin films
3. Dehydration bake
4. Spin coating of HDMS
5. Spin coating of photo-resist
6. Soft bake (Pre-bake)
7. Mask fabrication
8. Exposure
9. Post exposure bake
10. Development of photo-resist
11. Etching of nickel
12. Etching of titanium
13. Etching photo-resist for the second time
14. UVO exposure
15. Spinning of nanocomposite and heating it.
16. Etching nickel second time
17. Etching titanium second time.

5.2.1 Substrate cleaning

4” diameter silicon substrates, with 100nm thickness of silicon oxide layer is used for this process. These single crystal silicon substrates are cleaned and cut into smaller pieces, typically 1”. They are washed with de-ionized water to remove any foreign particles present on them. They are further dried with air-gun thoroughly to remove the traces of moisture on the surface. Figure 28 shows the cross-sectional layout of the SiO_2 substrate.

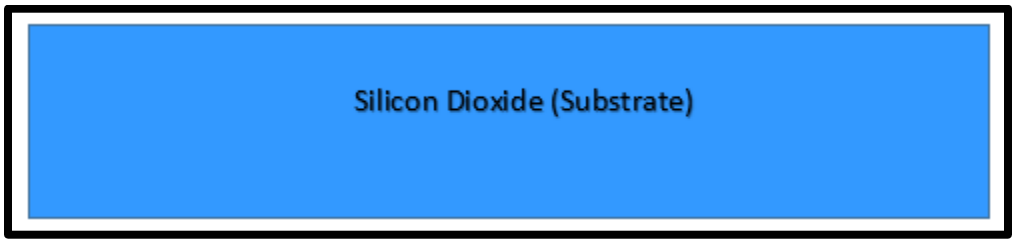

Figure 28: Cross-sectional layout of the SiO2 substrate

5.2.2 Sputtering of titanium and nickel thin films

After the substrate is cleaned, substrates are loaded inside the machine. PVD 75, Kurt J. Lesker Inc., USA was used to perform this thin film deposition process. Substrates are placed on the

substrate holder. The system is run initially on rotary vacuum pump and then later handled by high speed turbo vacuum pump.

Titanium is commonly used as adhesive promoting layer on silicon substrates and nickel is used as a conducting layer. This titanium and nickel thin films act as sacrificial layers which are going to be etched in the following steps. Magnetron sputtering process is used to deposit these thin films on the substrate. This technique is also known as “physical vapor deposition”. Initially the system is pumped down to a base pressure of 1×10^{-6} torr. The material which is to be deposited is present in the form of metal targets inside the vacuum chamber. Magnets are attached to these metal targets and they act as cathode. The positive ions present in Argon gas, which is admitted into the vacuum chamber, are attracted towards the metal targets. When the positive ions hit the metal targets, metal atoms are released. The operating pressure or the sputtering pressure during the deposition process is 4×10^{-2} torr. These atoms move towards the substrate, which is placed on the top is metal targets, and form a thin film. In order to eject an atom from the target, an energy greater than surface binding energy, of the atoms that are to be ejected, should be supplied. 300mA of current is supplied and the deposition takes place around 300-400V. Titanium is deposited for 5minutes which forms a thin film of around 5-10nm (figure 29). Later nickel is deposited for 15minutes which yielded a thickness of around 35-45nm (figure 30).

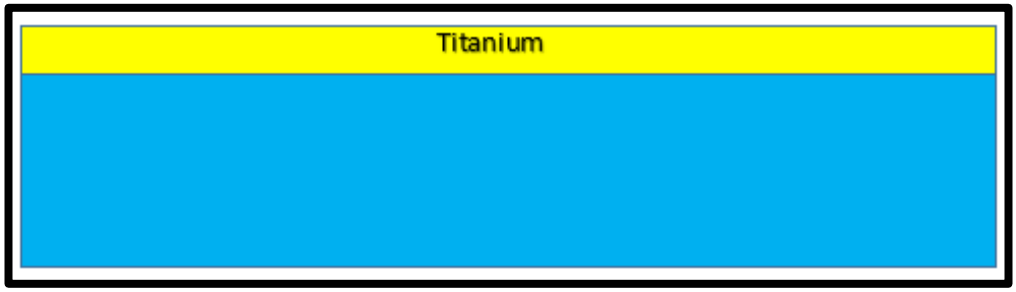

Figure 29: Titanium thin film on SiO2 substrate

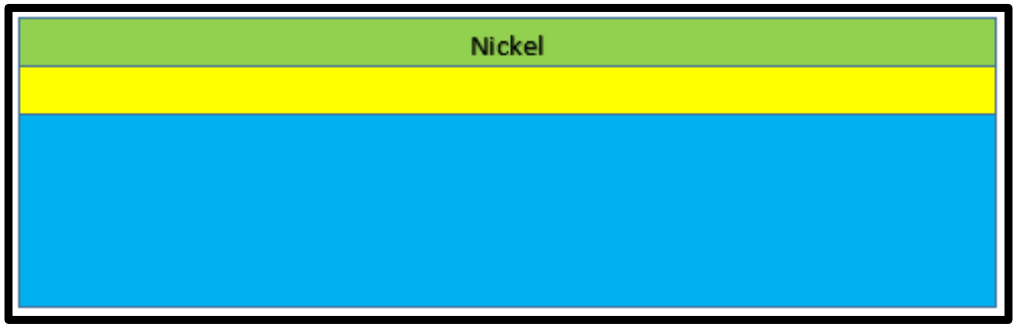

Figure 30: Nickel thin film on top of titanium layer

5.2.3 Dehydration bake

After deposition of titanium and nickel thin films, silicon substrates are subjected to dehydration bake. It is carried out in a convective oven at 120°C for 30 minutes to remove any moisture present on the films.

5.2.4 Spinning of Hexamethyldisilazane (HMDS)

HMDS is spin on to the substrate at 2000rpm for 30seconds. This deposits a thin layer of HMDS whose purpose is to increase the adhesive nature of photoresist on the substrate, which will be deposited in the following step.

5.2.5 Spinning of photo-resist

Photoresist is a polymer which changes its properties when exposed to UV light. Photoresists are usually two types which are positive photoresist and negative photoresist. The difference between both of them is, the UV light exposed region develops away for a positive resist and the UV light exposed region strengthens for a negative photoresist. The mask design depends on the type of photoresist used. The thickness of photoresist depend on the spinning speed. As the spinner speed increases, the thickness of the photoresist layer decreases. This is shown in figure 31.

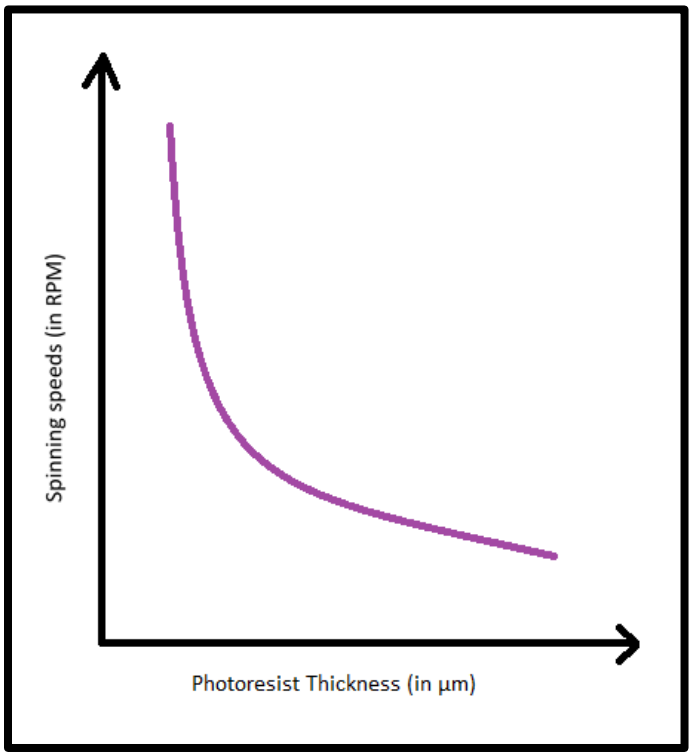

Figure 31: Spinning speed vs photoresist thickness plot

SU8-2025, purchased from MicroChem Inc., USA. is a negative photoresist used in this research. It is a highly viscous liquid which was used to deposit thick layers and was originally prepared by IBM for their fabrication process. The thickness of prepared layer depends on the spinning speed and time. 2-5ml of photoresist is dropped on the substrate and then spinned using a spinner. In this fabrication process, the substrate was initially spinned at 500rpm for 10 seconds and then ramped up to 1500rpm 30seconds. The initial speed condition was to spread the photoresist uniformly on the substrate and the layer speed was to achieve the desired thickness. This would result the thickness of photoresist around 20-30μm [142]. Figure 32 gives the overview of spinning speeds with change in time. Figure 33 depicts the cross-sectional view after depositing SU8-2025.

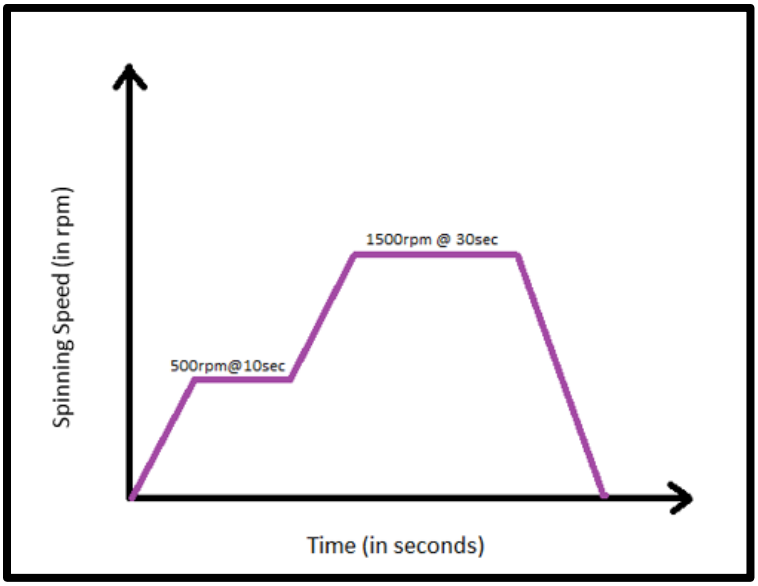

Figure 32: Spinning speed vs time to form photoresist layer

Figure 33: Cross-sectional layout of Silicon substrate with photoresist

The thickness of the deposited photoresist layer is given by the formula

Thickness = $(KC^2\eta) / s$

Where, K is calibration constant (ranging from 80 – 100), C is photoresist solid concentration (in %), ŋ is viscosity of photoresist, and s is spinner speed.

5.2.6 Soft bake

This step is done to remove moisture or water vapor from the photoresist and harden it so that it will not stick to the mask in the following step. After spinning the photoresist on the substrate, it is soft baked on hot plate at 65°C for 10minutes and 90°C for 20minutes. The temperature and time parameters should be chosen carefully because if the photoresist is under baked, it would stick to the mask in the next step or it would keep flowing on the substrate and if it is over baked, it would affect the photo-sensitivity of the material. Figure 34 represents the soft bake temperature parameters.

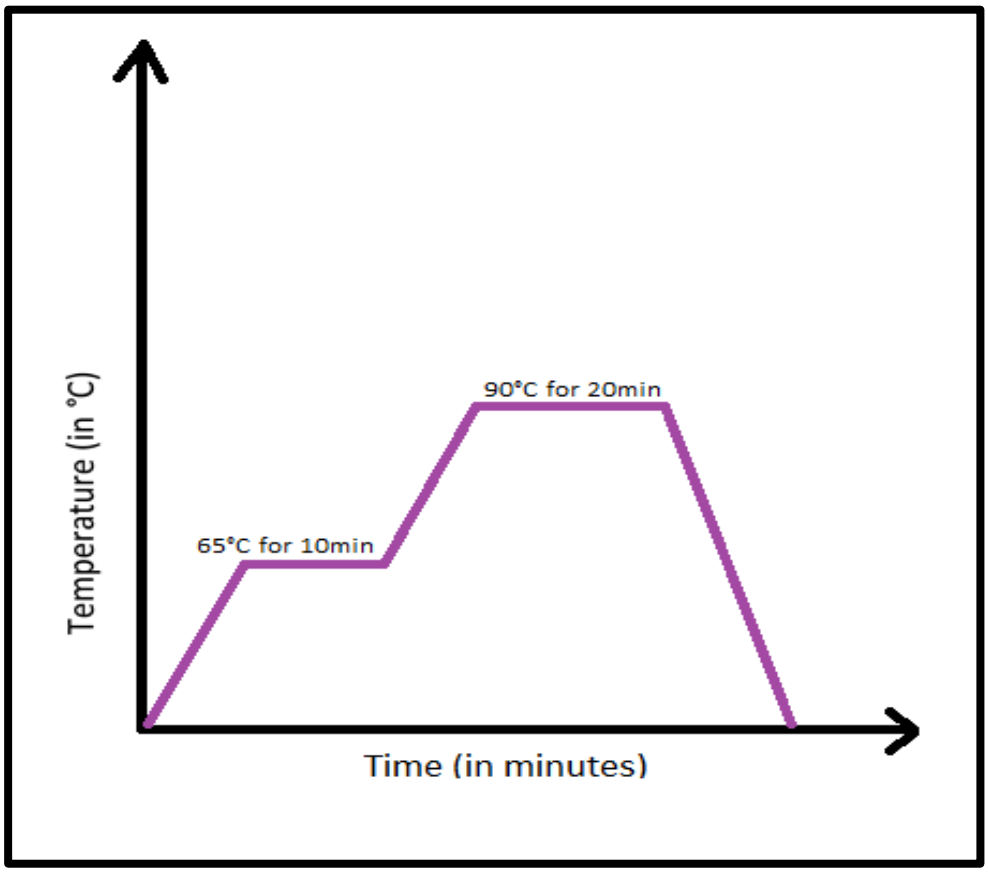

Figure 34: A schematic of two-step process of temperature vs. time in soft bake process

5.2.7 Mask fabrication

The mask has the pattern that needs to be transferred to the substrate. There are two types of masks which are positive mask and negative mask. They are printed on glass or transparent sheets considering the desired resolution of the final mask to be fabricated. A high resolution mask is obtained when printed on glass and low resolution mask is obtained when printed on transparent sheet. A suitable mask is prepared for patterning the negative photoresist that was used in this work such that the required pattern is developed at the end of the process. Initially, the mask drawing is prepared using AutoCAD software. This sketch represents the actual pattern to be printed on the mask. Figure 35 shows the mask used in this process.

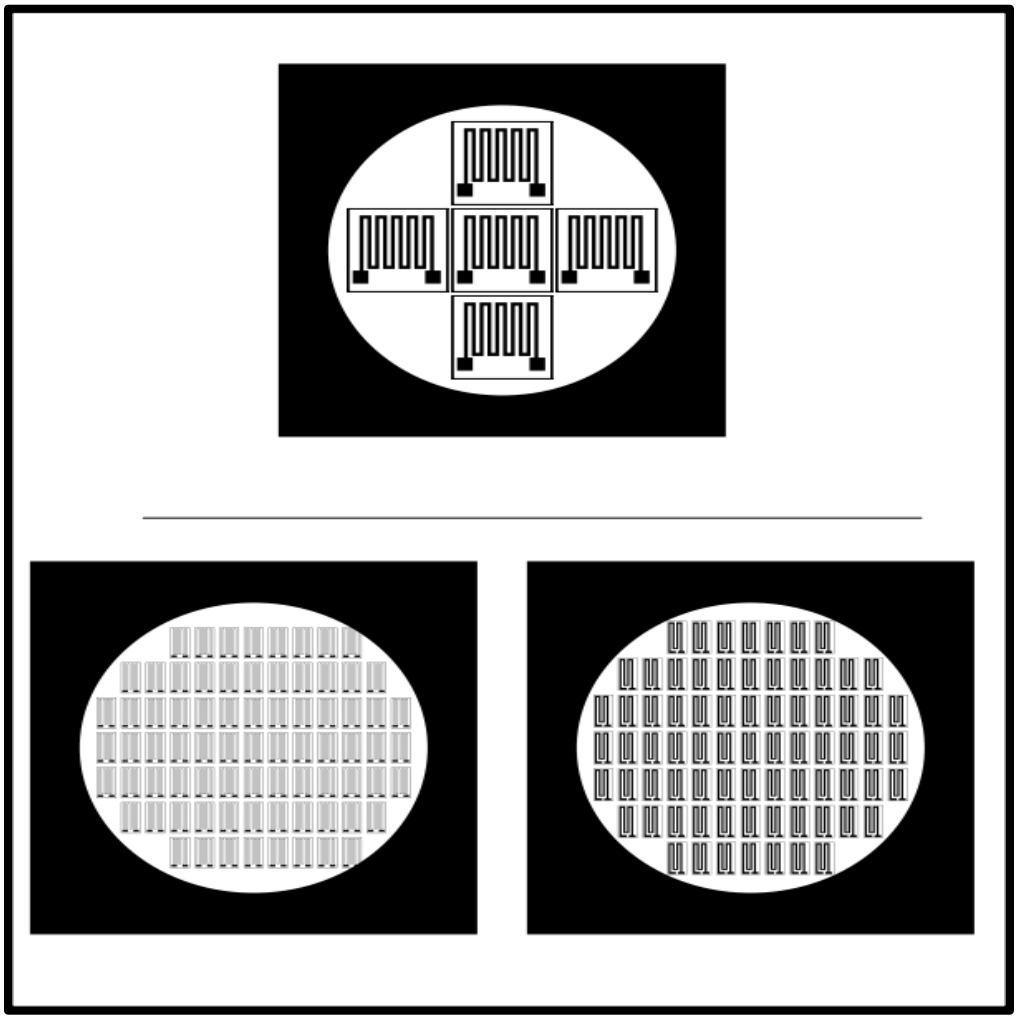

Figure 35: Pattern layout of the negative photo mask

5.2.8 Exposure

The image from the pattern from above mask needs to be transferred to the substrate. So, the mask is placed on mask aligner and UV rays are passed through it. Karl Suss MA45 mask aligner is used in this process shown in Figure 36.

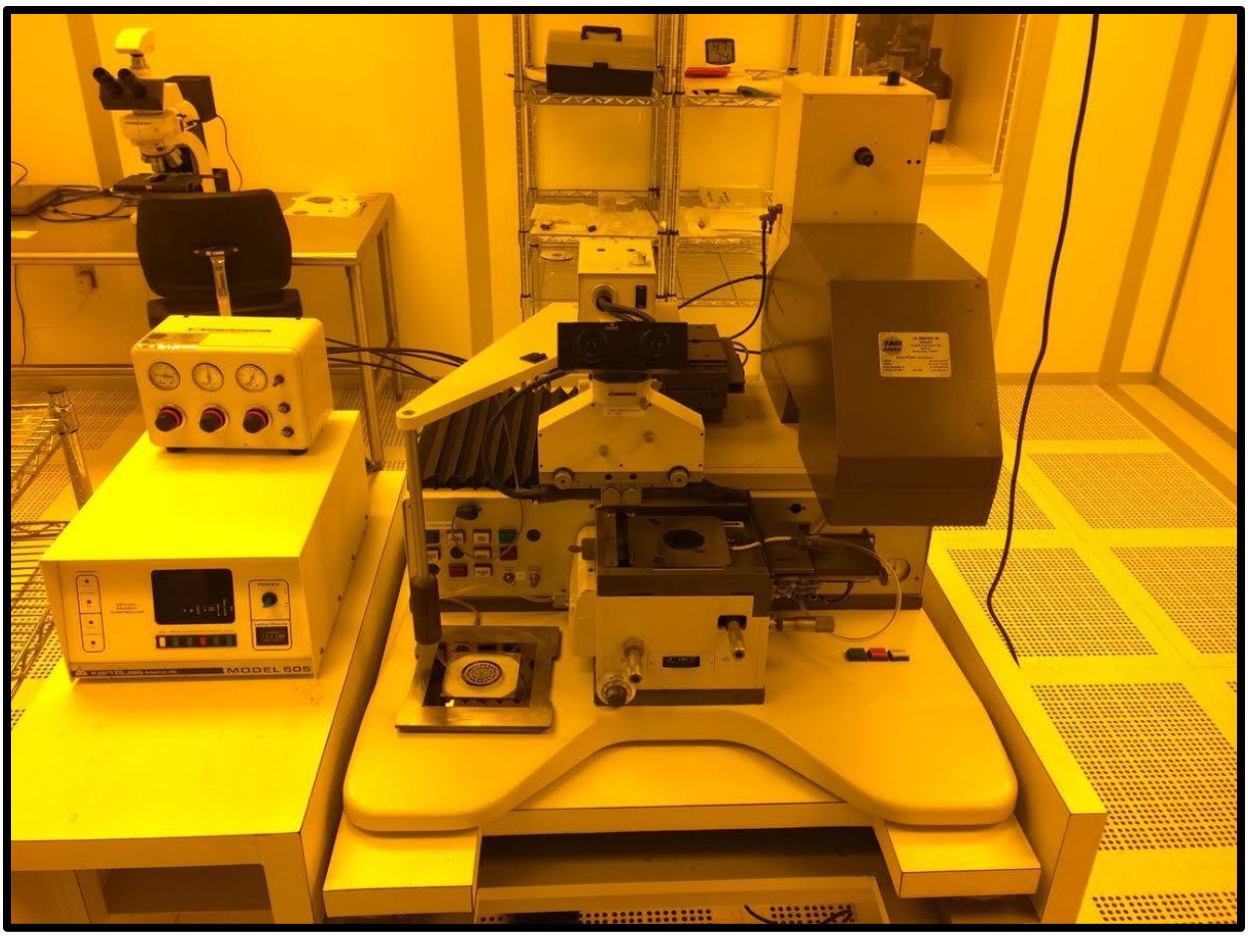

Figure 36: Karl Suss MA45 mask aligner

The substrate is placed on the substrate holder of the mask aligner. The mask is placed above the mask holder stage. The distance between the mask and the substrate should be minimal to prevent possible shadowing effects. When exposed, UV rays pass through the transparent regions of the mask and will be focused on the SU8 on the substrate, while the opaque regions block the UV light. The exposure dosage for this photoresist is 300mJ/cm^2 and the time of exposure is calculated as 30 seconds. Because this is a negative photoresist, UV light strengthens the exposed regions compared to the unexposed regions. Figure 37 shows the UV exposure process cross sectional view.

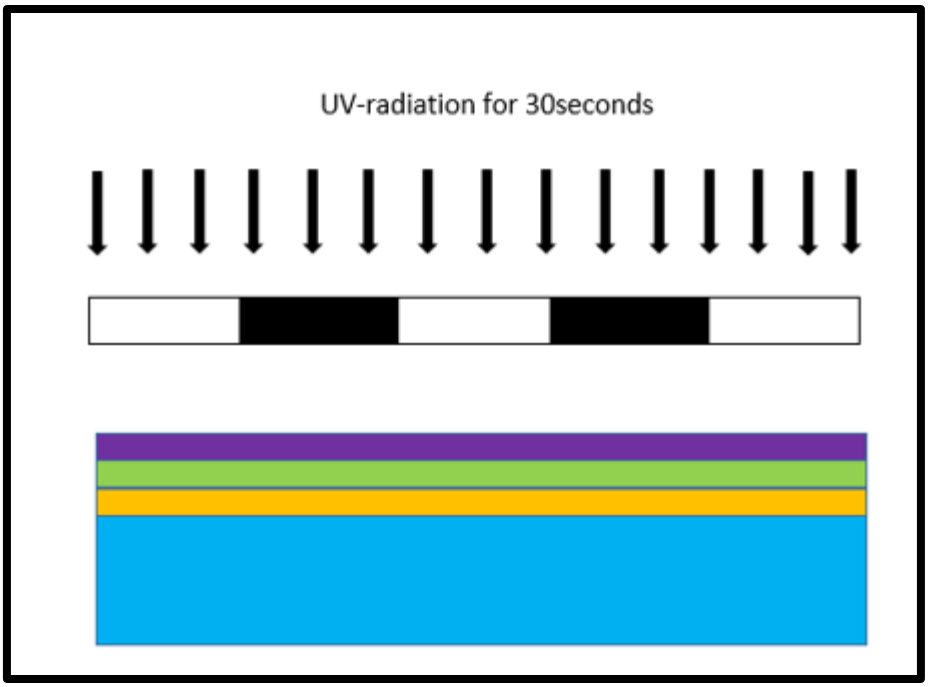

Figure 37: Cross sectional view of UV exposure process

5.2.9 Post exposure bake (PEB)

After the exposure process, the wafer is heated at 90°C for 5minutes. This step is needed to selectively crosslink exposed regions of SU8. It also helps in minimizing the residual stresses during cross-linking. This process help in fixing few dangling bonds present in between the exposed and unexposed regions. It also makes the strong bonds stronger and weak bonds much weaker, which will be useful in the development process.

5.2.10 Development of photo-resist

Dissolution of unpolymerized resist into an image, by the transformation of latent resist image is known as Development. In other words, the removal of weakly bonded regions, unexposed regions in this case. After post exposure bake, the substrate is immersed in photoresist developer. This developer removes the weakly bonded regions leaving the exposed regions of the resist which is strengthened after exposure. In order, to develop the substrate properly, strong agitation of substrate in the developer is required. Over developing the substrate results in removal of excess photoresist or under developing causes the weak bonds to stay in place. To avoid this, the developed structure is observed, at regular intervals, under an optical microscope. Figure 38 shows the optical microscope used in this process. Figure 39 show the cross sectional view of the substrate after developing photoresist. Figure 40 shows the SU8 patterned regions on the silicon substrate.

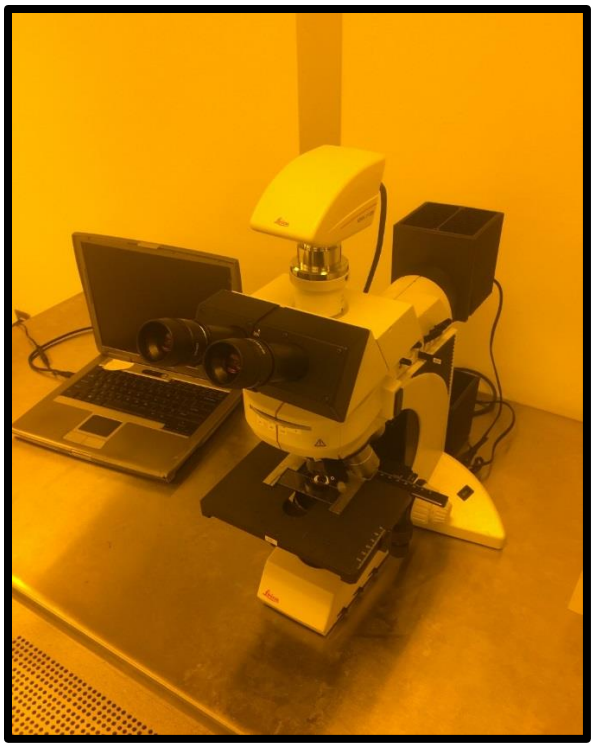

Figure 38: Optical microscope

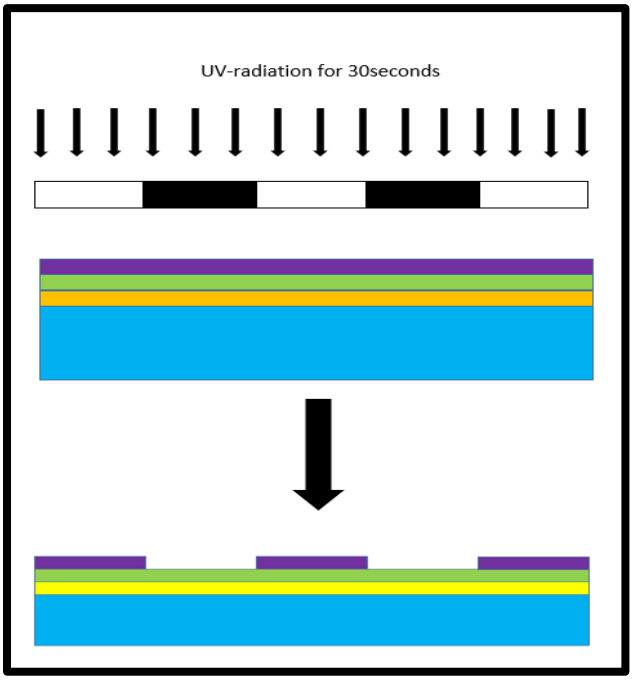

Figure 39: Cross-sectional view after exposing the substrate and developing it

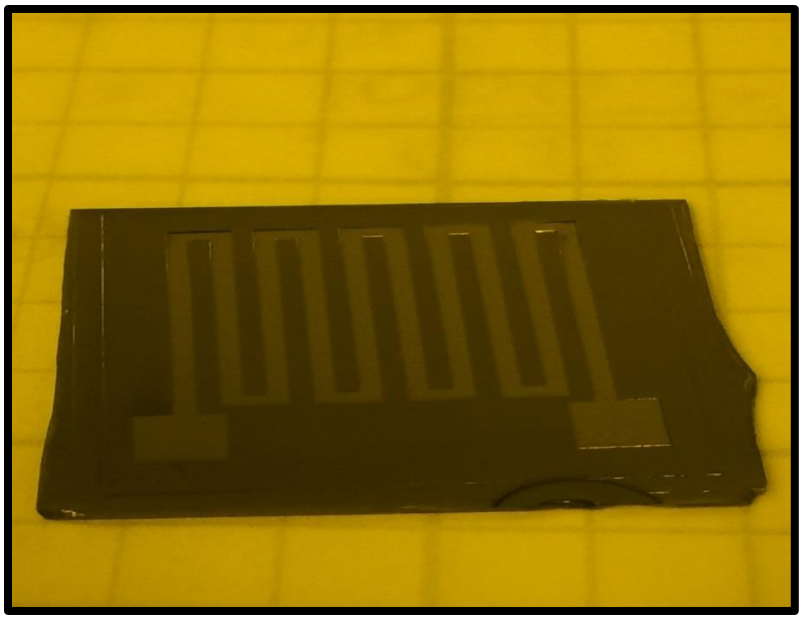

Figure 40: SU8 developed SiO2 substrate with engraved grooves

5.2.11 Etching of nickel

Nickel under the SU8 developed region, is etched using an acid solution which is a mixture of 10%HCl, 33% HNO_3 and 67% de-ionized water[143]. Etching process is performed by taking proper eye protection and extra safety gloves inside fume hood.

After preparing a fresh acid solution every time, the substrate is strongly agitated in this solution. Proper eye care and hands protection should be taken during solution preparation process or etching process. After taking the sample from the acid solution, they should be immediately immersed in DI water and cleaned thoroughly to ensure complete etch step. Then it is dried with air-gun to remove the moisture. The sample should be regularly observed under the microscope to stop etching as soon as the nickel layer is completely etched. It takes 5-10 minutes to etch 35-45nm of nickel. Figure 41 shows the cross sectional view after etching Nickel.

Figure 41: Cross sectional view after etching Nickel

5.2.12 Etching titanium

Titanium, under the etched nickel region, is etched using 10% hydrofluoric acid solution. It's prepared by adding 10% HF to 90%water[143].

After preparing a fresh HF solution, the substrate to be etched is strongly agitated in this HF solution. After completing the etching process, substrate is taken out and immersed in DI water. It is then dried with air-gun to remove traces of moisture. It takes 10minutes to 5-10nm of titanium.

In this step 100nm of SiO_2 which is present on the silicon substrate is also etched. Figure 42 shows the cross-sectional view after etching Titanium.

Figure 42: Cross sectional view after etching Titanium

5.2.13 Etching photoresist (second time)

After etching nickel and titanium, pattern is formed on the substrate. After etching both nickel and titanium, SU8 photoresist is removed using acetone. This process is done for 7-10minutes by agitating the substrate strongly in acetone. After this step, the substrate is left with pattern in between nickel and titanium thin films.

Titanium and nickel are deposited instead of just spin photoresist and expose it to UV and pattern it because CNT-polymer composite will be removed when it is treated with acetone. The substrate is treated with acetone, to remove non-patterned SU8, which removes the entire composite. Hence titanium and nickel are deposited and etched. Figure 43 shows the cross-sectional view after etching photoresist. Figure 44 shows the SiO_2 substrate after etching photoresist.

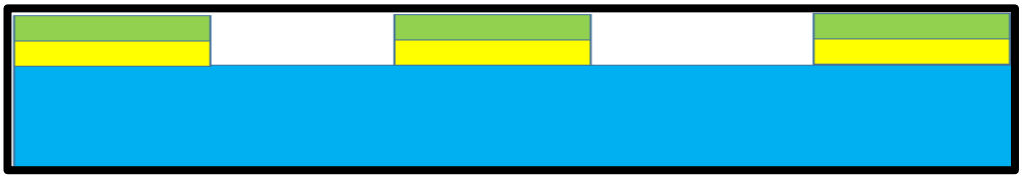

Figure 43: Cross sectional view after etching Photoresist (second time)

Figure 44: Schematic of SiO2 substrate after etching photoresist

5.2.14 Ultraviolet light exposure

Substrate with remaining titanium-nickel pattern is exposed to UV light to improve wetting characteristics of the substrate. This essentially makes the substrate more hydrophilic, the CNT-composite which will be deposited in the following step, sticks well to the substrate. This process is done for 20minutes. To understand this process, refer section 3.3 in chapter 3.

5.2.15 Spinning of CNT-polymer composite

After exposing the substrate to UVO, CNT polymer is spin coated on the substrate. This is done at 500rpm for 30 seconds using spinner. After this process, a thin film of CNT composite is deposited on the top of the substrate. The substrate is then at 80°C for 30minutes to remove moisture and harden the CNT composite. After the baking process, the film is porous which result in a discontinuous film. To overcome this, a second layer of CNT composite is deposited at same experimental conditions. A continuous thin CNT composite films is deposited at the end of this step. Figure 45 shows the cross-sectional view of the CNT-polymer spin coated substrate.

Figure 45: Cross-sectional view after spin coating with CNT-polymer composite

5.2.16 Etching nickel (second time)

At this stage, “lift-off process” is used to remove the CNT film in wanted areas so that, CNT composite is present in the strain gauge structure, which is the pattern present on the substrate. Same chemical solution which was prepared earlier, 10%HCl, 33% HNO_3 and 67% de-ionized water, was used. This region of etching has more surface area than the previous step. So, the etching time will vary around 10-15minutes. After the nickel is etched, the CNT composite present on it will be removed and only the composite present in the pattern will retain. Figure 46 shows the cross-sectional view after etching nickel.

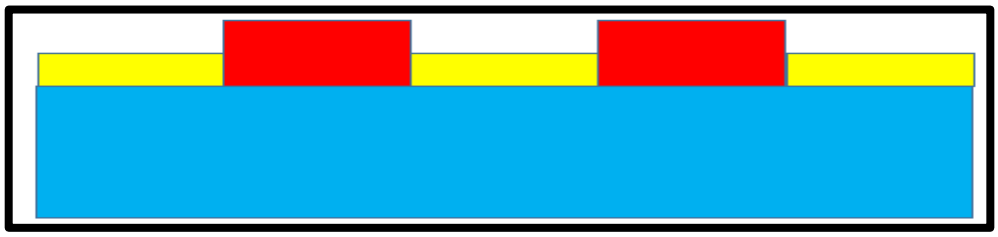

Figure 46: Cross-sectional view after etching nickel (second time)

5.2.17 Etching titanium (second time)

After etching nickel, left over titanium is etched using the same chemical solution prepared earlier, 10%HF and 90% DI water. The etching time will vary around 10-15 minutes because the etching region surface area is more than in the previous step. Figure 47 shows the cross-sectional view after etching titanium and Figure 48 shows the 3-D view after complete lithography process and Figure 49 shows the final fabricated sensor on the SiO_2 substrate.

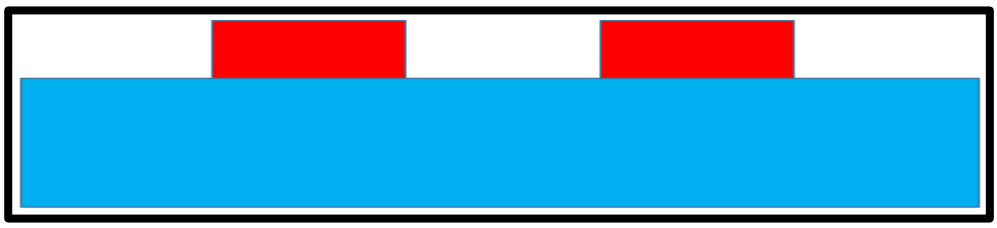

Figure 47: Cross-sectional view after etching titanium (second time)

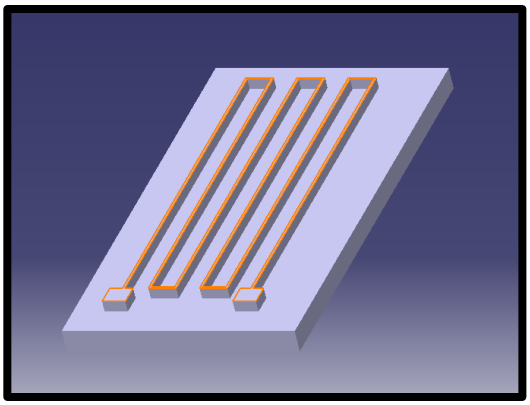

Figure 48: 3-D view after complete lithography process

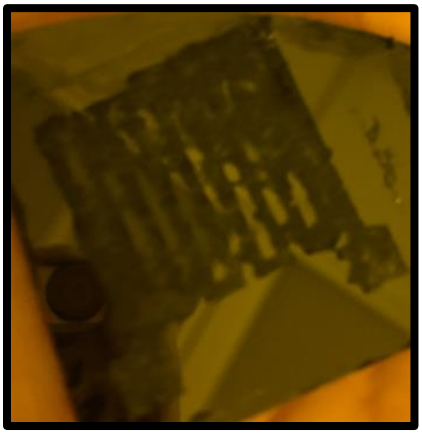

Figure 49: Final fabricated sensor on the SiO2 substrate

5.3 Summary

This chapter mainly focused on the design of strain sensor and fabrication of strain sensor using optical lithography technique. To investigate on this, finite element analysis was carried out using COMSOL Multiphysics. Hence in the next chapter, the concept of building the geometry and performing the finite element analysis is briefly discussed.

6 FINITE ELEMENT ANALYSIS OF STRAIN GAUGE

Previous chapter focused on fabrication of strain gauge using optical lithography technique. In this chapter, finite element analysis based simulation was carried out using COMSOL Multiphysics software 5.2a version. Once validated for a commercially available metal film strain gauge, the simulation of CNT-polymer based gauge and hence computed for gauge factor.

6.1 Defining the model

Simulations of the strain gauge requires a model that is like a gauge that is to be fabricated. To validate the simulation process, a commercially available sensor is used as the model. Analysis is performed on this modelled and compared the results with the technical specifications provided by the manufacturer. Then the model of the strain gauge that is to be fabricated is modelled and analyzed.

The model is assumed in such a way that; the sensor is initially modelled. Then it is placed on a cantilever beam which is subjected to point loads. The induced strain in the cantilever beam is measured using the sensor placed on the cantilever.

6.2 Building the geometric model

Metallic strain gauges are purchased from micro measurements. The dimensions of the conventional strain gauge were given in the previous chapter in figure 5.2. Now this sensor is modelled and is placed on an aluminum cantilever beam. A perfect surface contact is assumed between the two surfaces. The design modelling of this structure was done in Catia V5. Figure 50 shows the geometric model of sensor placed on cantilever beam.

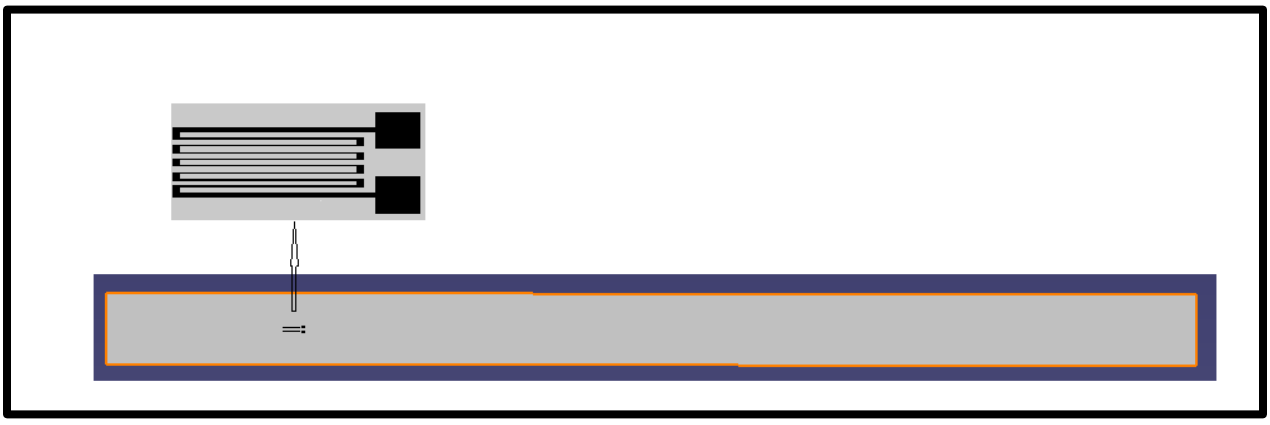

Figure 50: Schematic of strain gauge placed on cantilever beam. Exploded view of the sensor is shown in the inset

6.3 Multiphysics simulation

COMSOL Multiphysics is used to perform the multiphysics simulations. Geometric models prepared in Catia V5 are imported into COMSOL Multiphysics software using CAD geometry import module in COMSOL. The multiphysics simulation workflow is given in figure 51. Further they are discussed in detail.

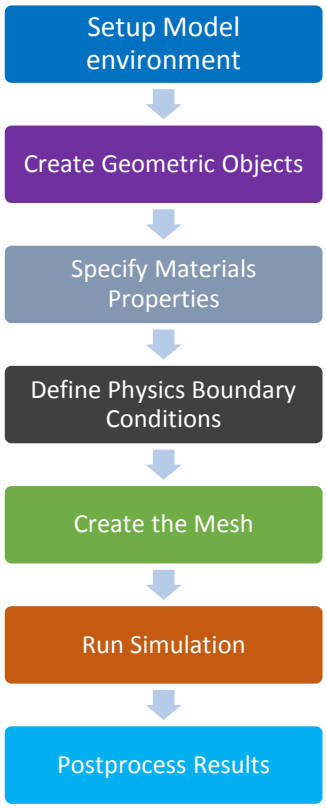

Figure 51: Multiphysics simulation workflow

6.3.1 Setting up model environment

In COMSOL Multiphysics software, the required model of the simulation is setup. A model wizard is used to define the physics, dimensions and study method. Multiphysics is added at this stage. Solid mechanics module (solid) and electric currents module (ec) are used to solve the model in a static loading condition using stationary study. The procedure followed to setup the model environment is shown in figures 52 a and b

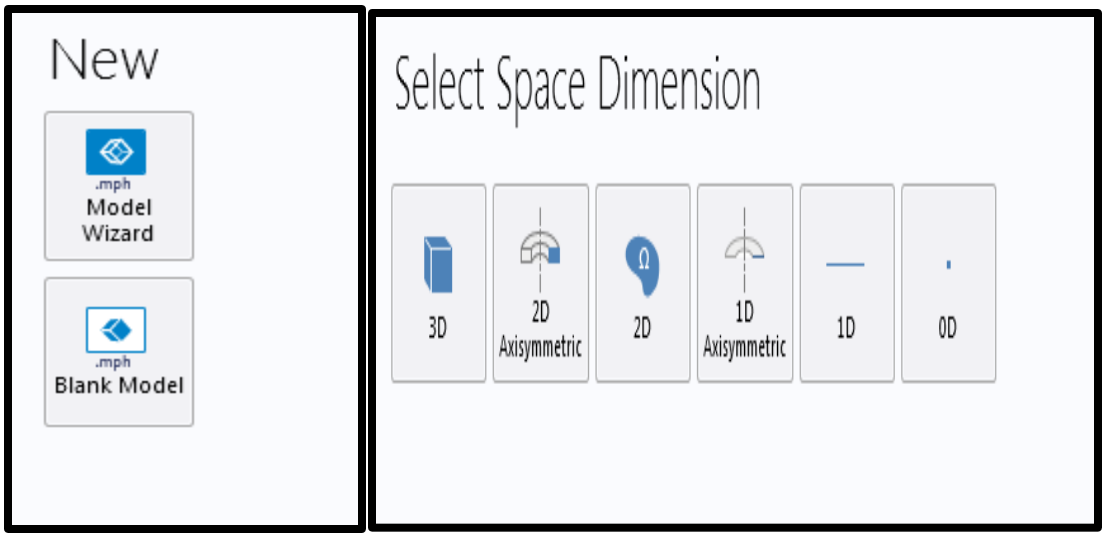

a) b)

Figure 52: a) Selection of type of model and b) space dimension

6.3.2 Create geometry objects

After the model is designed,it is imported to COMSOL using CAD import module feature in COMSOL software. COMSOL imports the geometry and translates the dimensions as initially specified in the original design. Figure 53 shows the geometric objects that are imported to COMSOL Multiphysics.

6.3.3 Specifying the material properties

COMSOL has got the builtin material properties library. It also allows to manually input the new material properties, if desired. Depending on the added physics, COMSOL prompts for some material properties. In this research, aluminum is defined for cantileverwhile the strain gauge is initially defined as CONSTANTAN and with CNT-polymer composite properties.

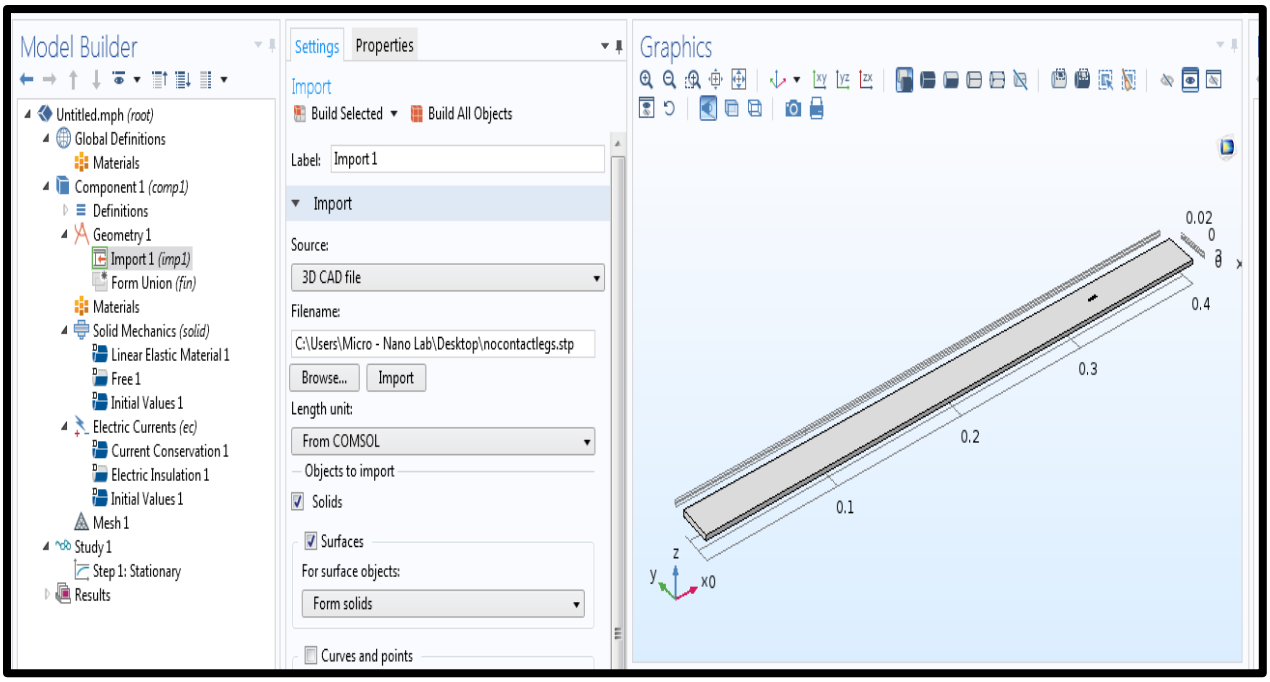

Figure 53: Importing geometric model from Catia V5 to COMSOL

6.3.4 Defining physics and boundary conditions

This is the key step to the complete finite element analysis. To perform the simulation correctly, one should understand the physics and working principal of the model in real time situation, without which the problem cannot be solved with accurate results. This process basically comprises of two steps which are defining the physics and setting up boundary conditions. After choosing the physics, boundary conditions for solid mechanics and electric currents modules are setup separately.

In solid mechanic's module, a fixed constraint is defined to fix the cantilever on one end and the application of point load on the other end of the cantilever. These point loads can be varied by using parametric sweep option in COMSOL Multiphysics.

In electric currents module, one of the contact pads, of the sensor, in grounded and the terminal boundary condition is assigned to the other contact pad. The boundary surface between the sensor and the cantilever beam is electrically insulated.

6.3.5 Creating mesh

The use a default physics controlled mesh is recommended in COMSOL. This generates a mesh adopted to the physics defined in the model. COMSOL decides the mesh suitable for a particular physics. Changing physics in your mesh will automatically update the adopted mesh required for

the respective physics. However, it is possible to define the user control mesh. This simulation used a physics controlled default ultrafine mesh given in COMSOL. Figure 54 shows the mesh used in the simulation.

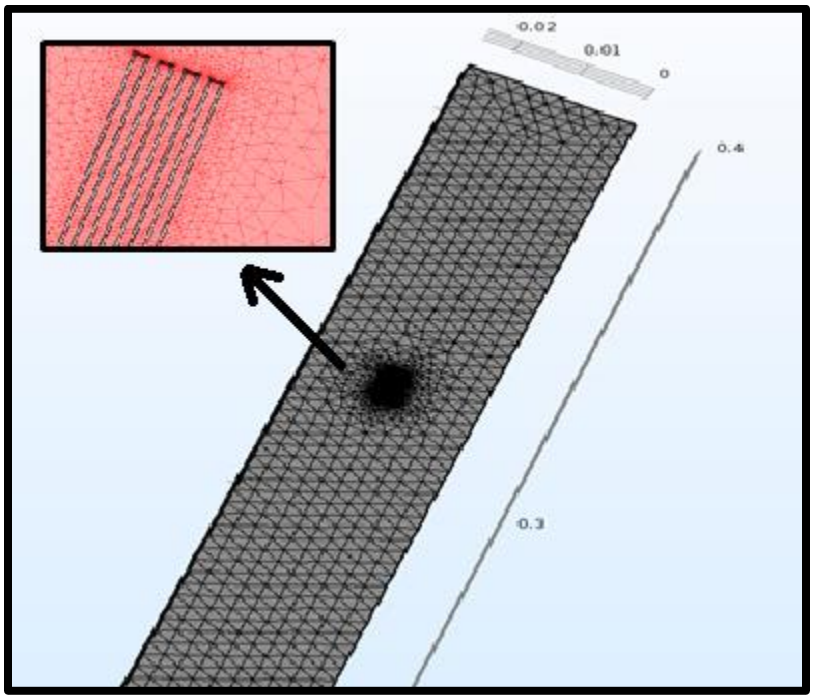

Figure 54: Ultra-fine physics controlled mesh of entire cantilever geometry. The inset of the figure shows the expanded view of strain gauge mesh

6.3.6 Simulating the model

Simulation was carried out after setting up the model completely. It was necessary to determine the relative tolerances, parametric sweeps and other required parameters. As this simulation mainly utilized solid mechanics and electric current modules, a plot of stress vs electric potential is plotted as the output.

6.3.7 Post processing the results

After solving the model, the post process of the generated results provided the plots of the chosen parameters. These can be depicted as volume plots and surface plots depending on the required output. Figure 55 shows the stress plot when a point load of 2N is applied on the cantilever which shows that stress is transferred from cantilever to the sensor. The cantilever has low strain regions compared to the sensor. Figure 56 shows the distribution of electric potential from ground to terminal region. Figure 57 shows the schematic of load vs. resistance plots which

is default output when solving for structural and electrical modules which shows the electro-mechanical nature of the material.

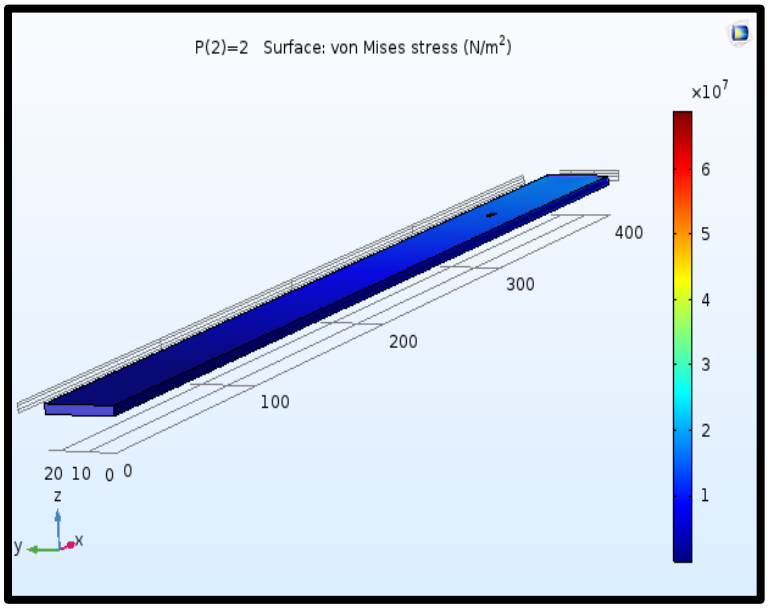

Figure 55: Stress plot

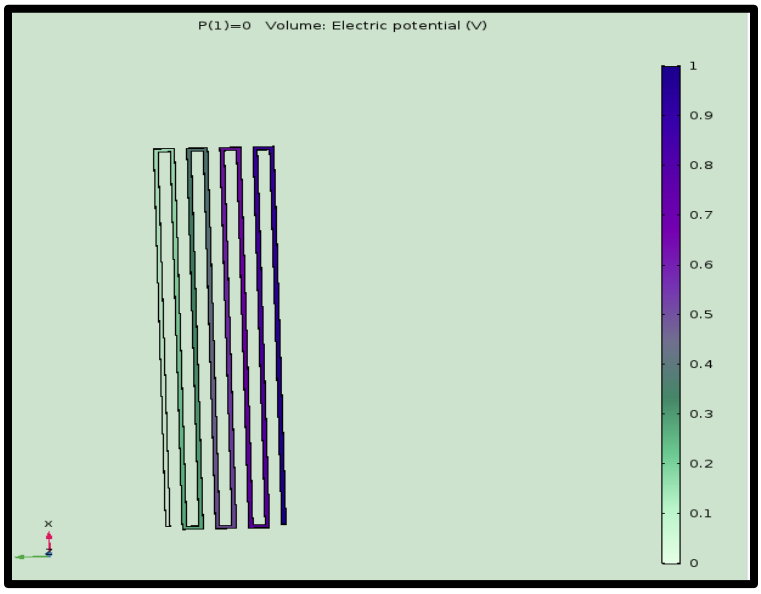

Figure 56: Electric potential plot

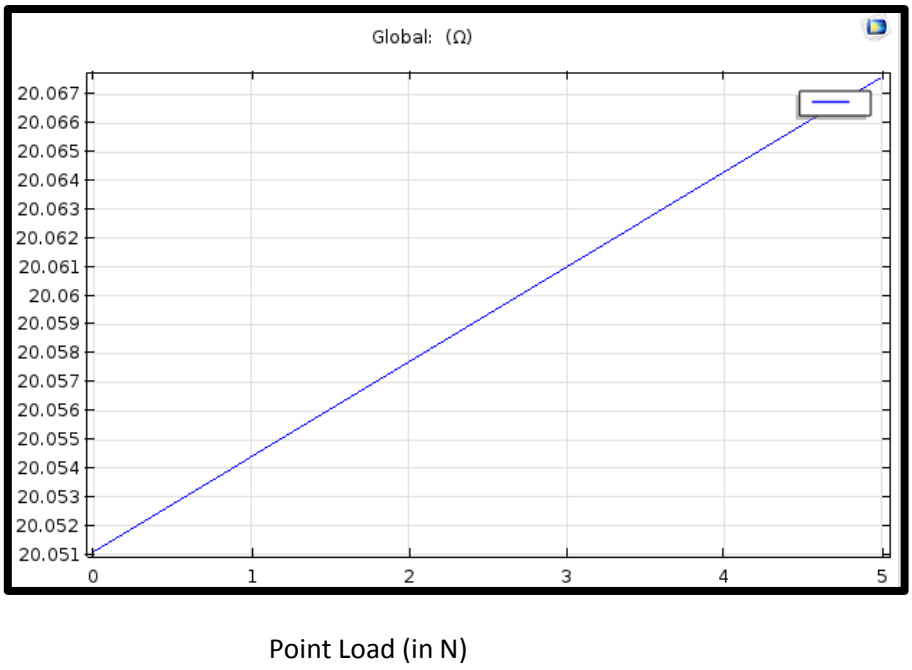

Figure 57: Load vs resistance plot

After post processing of results and calculating the gauge factor using the formula

$$\text{Gauge factor (G.F)} = \frac{\frac{\Delta R}{R0}}{\frac{\Delta L}{L}}$$

The gauge factor was found out to be around 2.2. The manufacturer provided information on gauge factor is 2.1$\pm$0.5%. Hence our model is validated.

After validating our model, the geometry of the conventional strain gauge is changed and replaced it with the CNT-polymer strain gauge pattern that was prepared for the fabrication process. The properties of CNTs with respective wt. % loading were obtained from the literature. The model is setup and analyzed as discussed earlier. Figure 58 shows the geometry with CNT-polymer strain gauge pattern.

Figure 58: Schematic of CNT-polymer strain gauge on cantilever beam

6.4 Summary

In this chapter, modelling of Strain sensor using CATIA V5 was discussed. This chapter also focused on the finite element analysis using COMSOL Multiphysics 5.2a. The analysis of conventional strain gauge was compared to the analysis of the CNT-composite strain gauge that was fabricated using optical lithography technique by computing the gauge factors of the strain gauges.

7 RESULTS, DISCUSSIONS AND CONCLUSIONS

In the previous chapter, finite element analysis of the strain gauge was detailed. This chapter focusses on the results obtained from each experimental technique for the CNTs grown using PECVD technique, CNT-polymer composite films. The discussion with relevant explanations are detailed. This chapter ends by stating the conclusions of our research.

The CNT based films deposited by MWCVD technique requires four major steps to achieve CNTs with desired properties. They include catalyst layer deposition, pre-annealing in H_2 environment, plasma treatment and further growth of CNTs in H_2 and CH_4 ambient at required pressure. As the first step is the catalyst layer deposition, titanium is deposited, on the Si with SiO_2 substrate, as the adhesion promoting layer and nickel was deposited as the catalyst layer. The thickness and composition of these metallic thin films are analyzed using Rutherford Backscattering Spectrometry.

7.1 Analysis of metallic thin films using Rutherford Backscattering Spectrometry (RBS)

Titanium and Nickel were deposited using magnetron sputtering technique. The growth and characteristics of CNTs depend on the properties and thickness of the thin films. In this study titanium and nickel films are deposited for different time intervals using magnetron sputtering technique. Three different sets of films were deposited for titanium and nickel which include Ti (1min)-Ni (1min), 3-3, 5-5 minute intervals respectively. It may be noted that a dual magnetron sputtering system with Ti and Ni sputtering targets was used for this purpose. Hence, Ti and Ni films were deposited in a single run sequentially with deposition of Ti followed by Nickel coating, without breaking the vacuum cycle. RBS determine the thickness and composition of these metallic films. The sharp silicon edge and Ni peak prove that there is no inter-atomic diffusion of metal atoms across the film. RBS used a 2MeV He^{2+} ion beam with scattering angle of 150°, exit angle of 30°, energy per channel of2.7521 Kev/channel. The film thickness was determined using SIMNRA software by computing the experimental data along with the fitted curves. The thickness of the thin film is determined from fitted experimental curve and simulated spectra obtained from SIMNRA. It is calculated by dividing the areal density of Ni peak(120.845E15 atoms/cm^2) which was given by SIMNRA with atomic density of bulk Ni (9.13E22 atoms/cm^2). Further a small peak is observed at channel 354 which indicates few traces of oxygen on the silicon background. Figure 59, 60 and 61 shows the experimental and simulated RBS data of 1min Ti-1min Ni, 3min Ti-3min Ni and 5minTi-5 min Ni respectively deposited thin films on silicon substrate.

In the RBS spectra, the channel number represented in x-axis corresponds to the energy of the back scattered helium ions.

As shown these spectra, Nickel being the largest atomic number (22), its peak is shown approximately at 560 channel number with titanium peak seen at channel number 510 followed by titanium peak. The peak width represents the thickness of the thin films. The smooth edges

of titanium and nickel peaks are indicative of the absence of any diffusion between the films. Comparing figures 7.1, 7.2, 7.3 it clearly shows that the relative peak width and intensities of Ti and Ni increased from 7.1 to 7.3 linearly, which clearly represents the increase in film thickness with increase in depositing time parameters. Though a small oxygen peak was observed in figure 7.1, it was not observed when the thickness of Ti and Ni are increased.

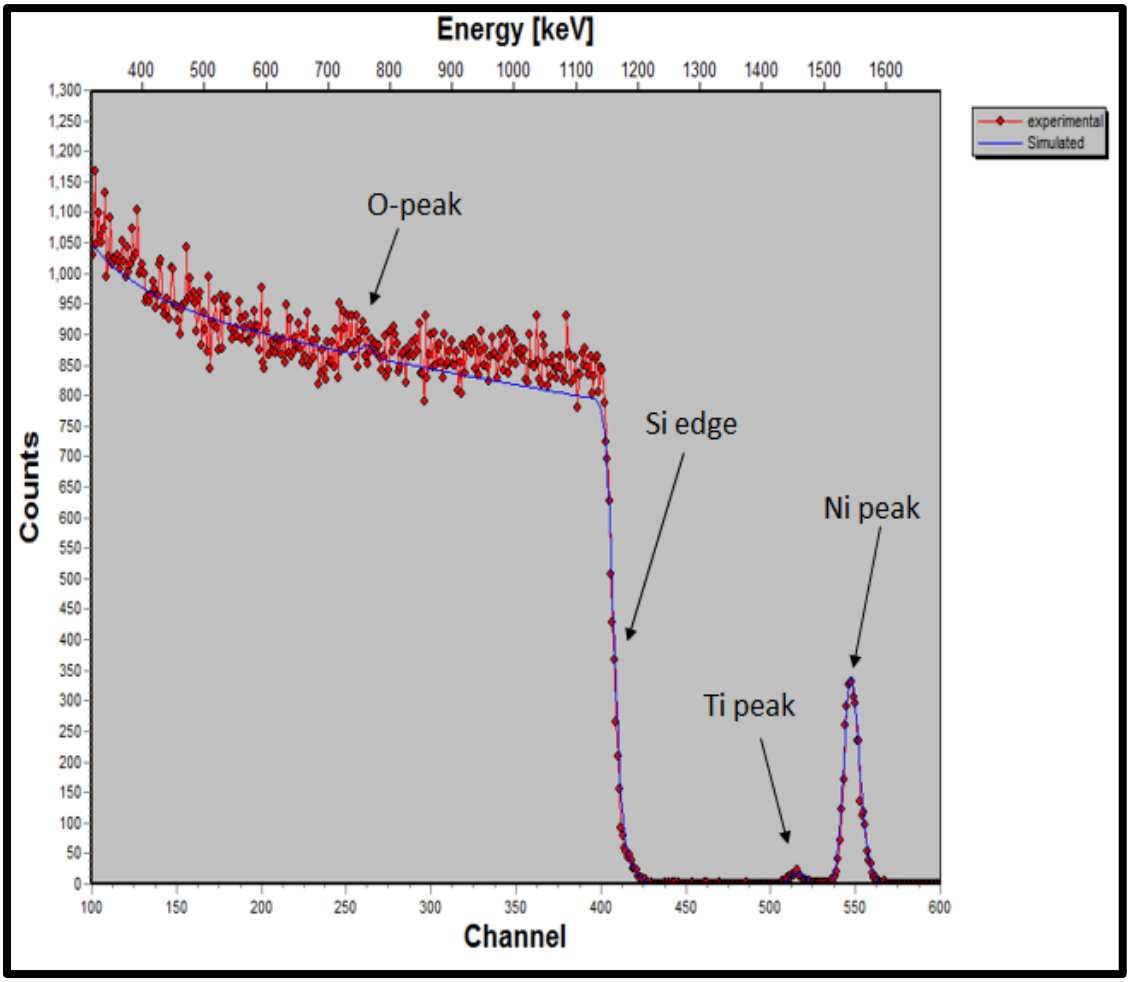

Figure 59: The experimental and simulated data of RBS spectra of 1min deposition of titanium and nickel respectively

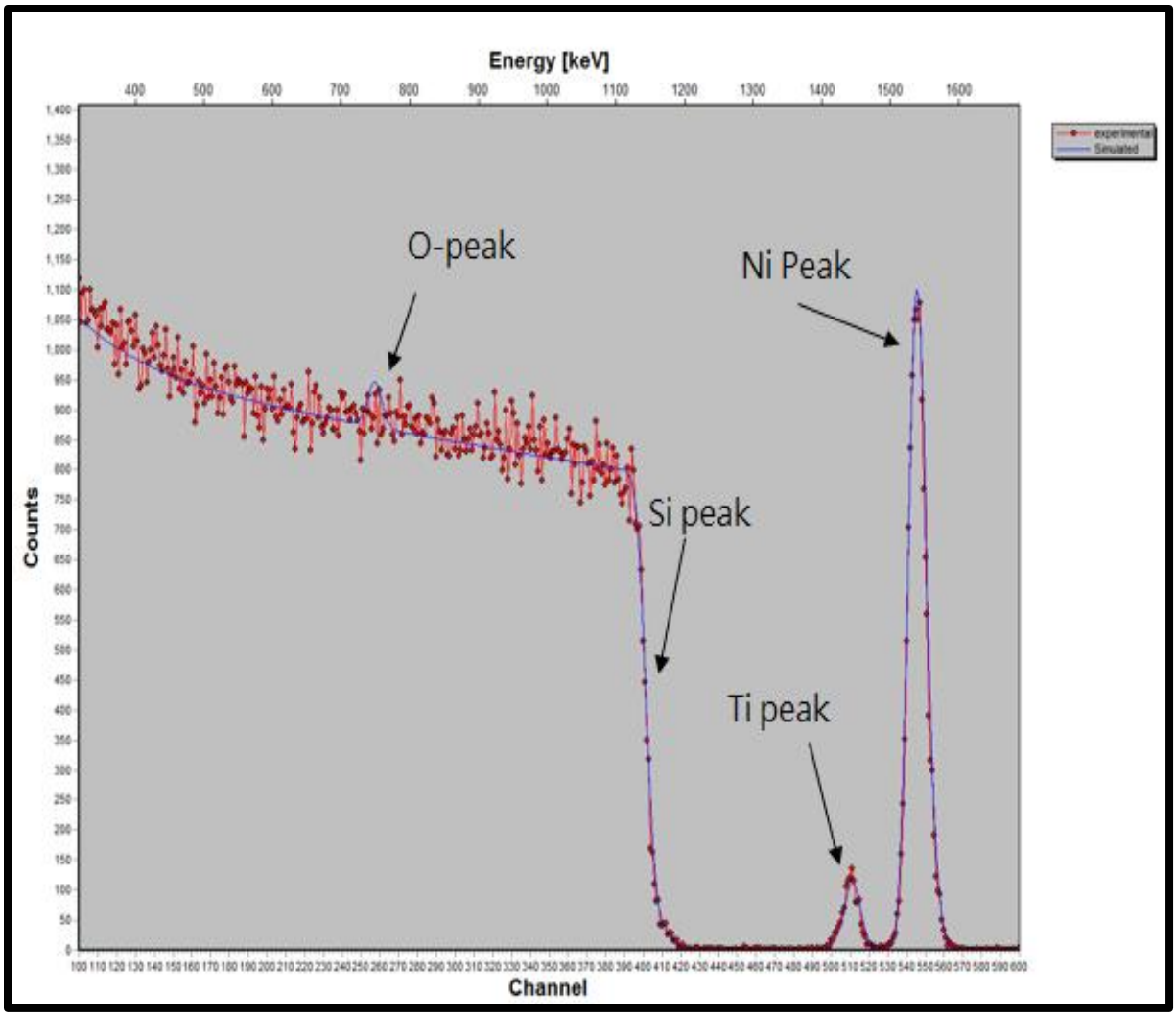

Figure 60: The experimental and simulated data of RBS spectra of 3min deposition of titanium and nickel respectively

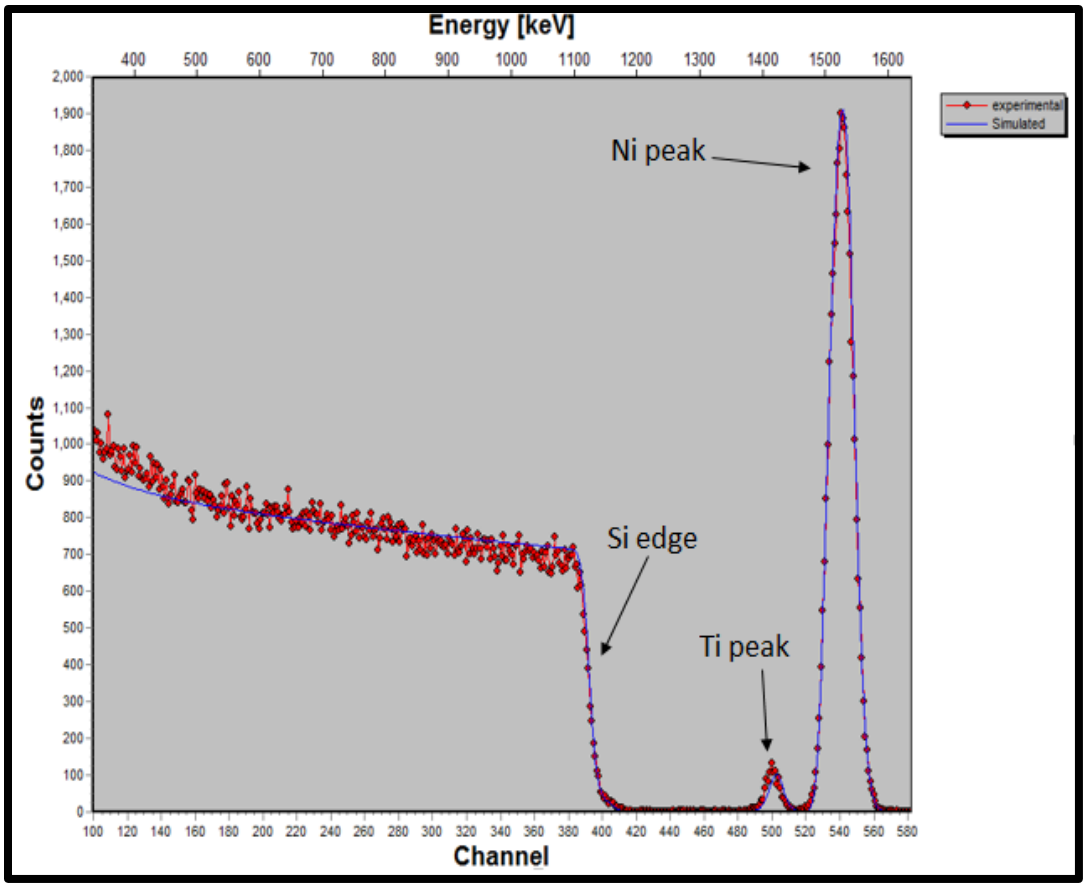

Figure 61: The experimental and simulated data of RBS spectra of 5min deposition of titanium and nickel respectively

Based on the RBS data calculations, the thickness of Ti thinfilms for 1 minute deposition was found to be 0.52nm and thickness of Nickel thinfilms for 1 minute depositions were found out to be as 2.63nm. The accuracy of the results were compared for the previous work[97]. The thickness of other deposited films are mentioned in table 3.

Table 3: Summary of thickness of titanium and nickel at various deposition times

Deposition time(in min.)	Ti thickness (in nm.) (± 1nm)	Ni thickness (in nm.) (± 2.9nm)
1	0.52	2.63
3	1.8	8.57
5	4.2	14.5

7.2 Scanning Electron Microscopy (SEM) analysis of CVD samples

After the evaluation of thickness of the thin films, substrates are placed inside the chamber, and using MWCVD technique, CNTs are deposited on the substrate with varying annealing time, plasma treatment time and growth parameters. Table 4 summarizes the details of different parameters that were varied during the deposition of CNT based films.

Table 4: Variation of experimental parameters in CVD process SEM images

Sample Name	Annealing time (in min.)	Plasma treatment time (in min.)	Growth time (in min.)
B	60	30	30
I	40	30	30
J	60	30	10
L	60	40	30

These samples were choosen from all the deposited samples to discuss their effects on the CNT films. Figure 62, 63, 64 and 65 shows the SEM images of all these samples.

Figure 62 and 63 are the SEM images of sample B and I, taken at 100,000 maginification, which are used to study used to study the properties of CNTs depending on the variation in hydrogen annealing treatment, and keeping plasma and growth times are constant. Hydrogen annealing is used to remove the oxide layer which might be formed on nickel thin film. This is carried out at 600°C. It is also used to break the nickel thin film into nickel nanoislands. Hence with increase in hydrogen annealing treatment time, the nickel oxide layer is completed removed and this promotes the growth of CNTs. From the pictures, it can be concluded that the growth and density of CNTs is higher with 40 minutes annealed sample than compared to high annealed sample. It may be due to agglomeration of nanoislands into a larger nanoisland which doesnot promote good growth of CNTs.

Figures 62 and 65 are the SEM images of sample B and L, taken at 100,000 magnification, which are used to study the effect of plasma treatment. The substrates are treated with different plasma treatment times, by keeping hydrogen annealing and growth times as constant. The flow rate of H_2 is 40sccm into the reaction chamber. Nickel nano islands are converted to nickel catalyst seeds which promote the growth of CNTs. Catalytic seeds are formed when the nickel nano-islands are bombarded with radicals, atoms, ions and electrons during hydrogen plasma treatment. When the plasma treatment is done for more time, the avaerage diameter of the catalytic seeds decreases, which further decreases the diameter of CNTs. From the figures, this phenomenon can be observed, when the average size of the CNTs decrease with increase in

hydrogen plasma treatment times. If the plasma treatment is done too long, there might be a chance of excessive deposition of active hydrogen radicals which attracts the hydrogen in the next steps and there seems to be a chance of deposition of excess hydrogen on the catalyst islands which ruin the growth of CNTs.

Figures 62 and 64 are the SEM images of sample B and J, taken at 100,000 magnification, which are used to study the effect of CNT growth times, by keeping the hydrogen annealing and plasma treatment times as constant. The flow rate of H_2 is 40sccm, Ar is 40sccm and CH_4 is 5sccm respectively. Different types of non-radicals, radicals, charged species and atomic hydrogen are present in plasma. The hydrocarbon gas gets disocciated into hydrogen and carbon, when treated with this plasma. Hydrogen generated from this process leaves the chamber while carbon gets settled or dissolved on the nickel nano catalyst seeds and the formation of CNTs take place. The growth of CNTs can be done by tip growth model or base growth model, which depends on the adhesion property of the catalyst layer with the substrate. This can be understood clearly from [141]. Sample J has 10 minute of growth process and B has 30minute growth process. By increasing the growth time parameters, the density of CNTs forest and number of CNTs increase on the film and this can be observed from the images and decreases after certain time due to excessive deposition of carbon on the catalyst islands. After the analysis of CNT based films using SEM, they are analyzed using Raman spectroscopy which is further discussed.

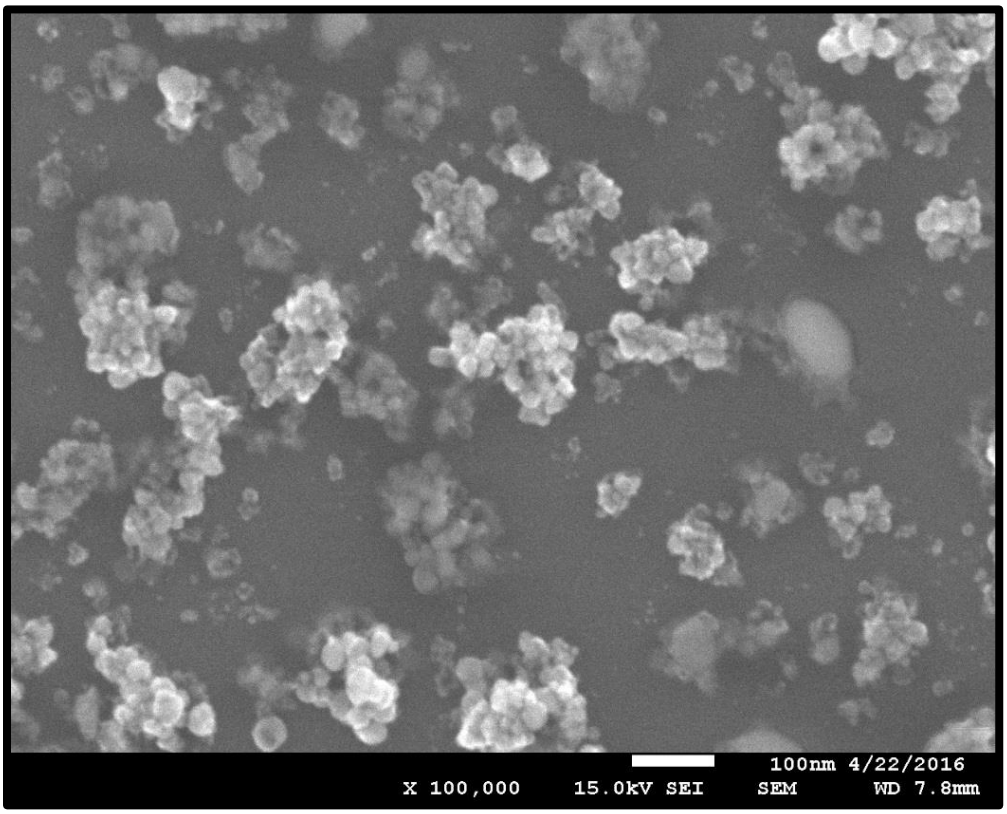

Figure 62: SEM image of sample B

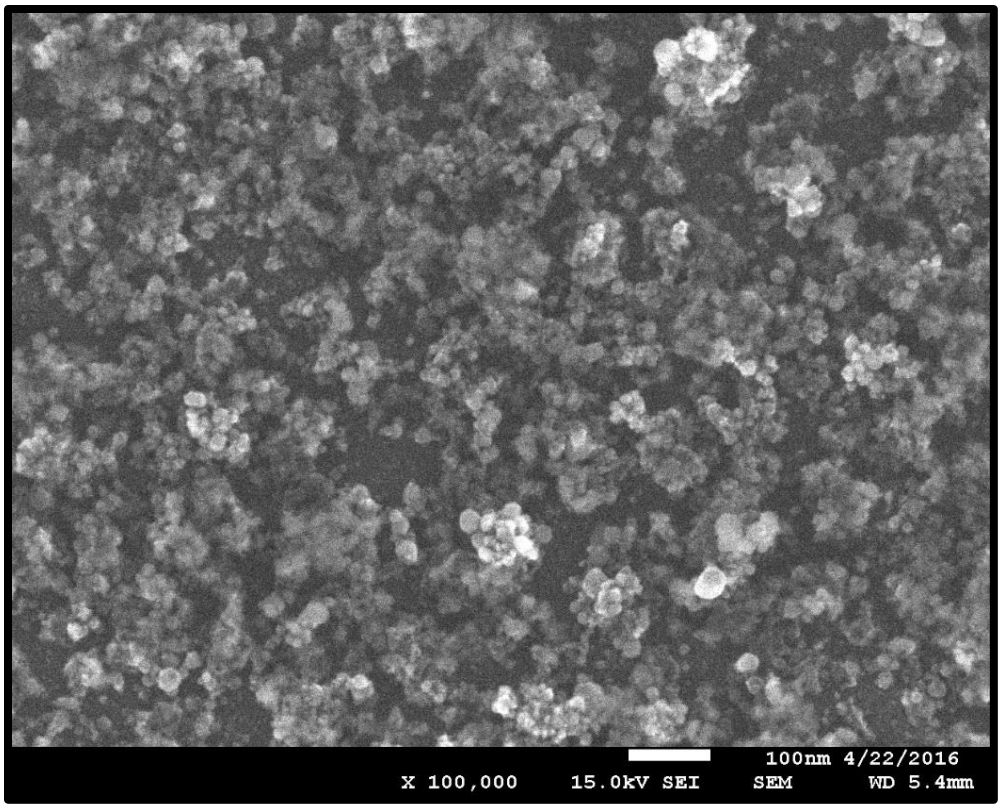

Figure 63: SEM image of sample I

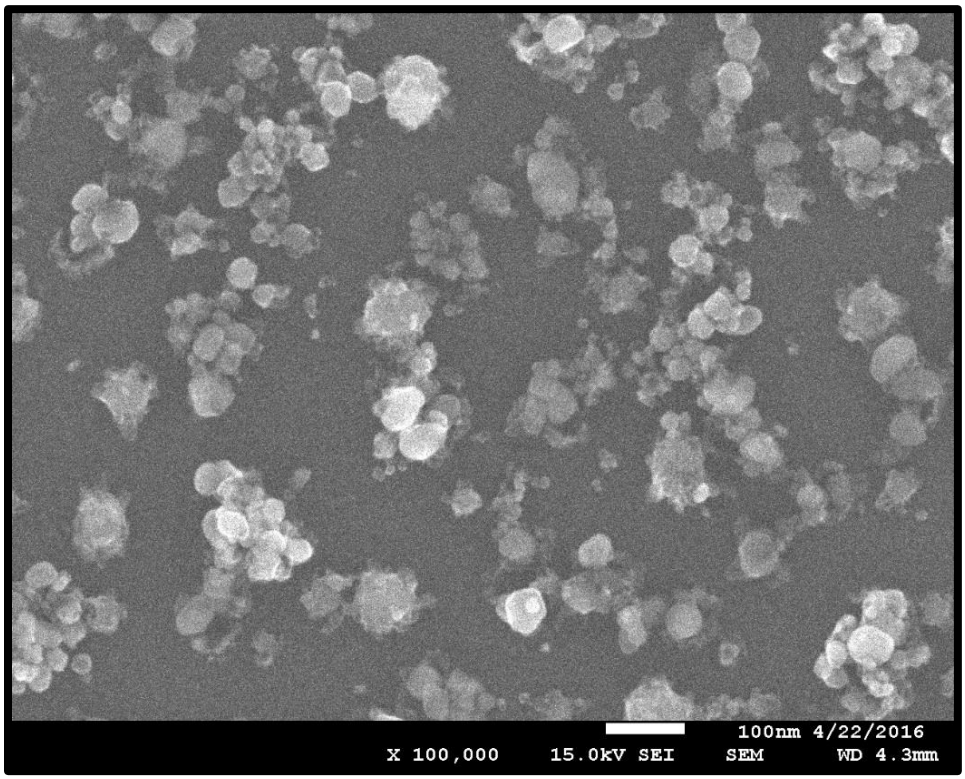

Figure 64: SEM image of sample J

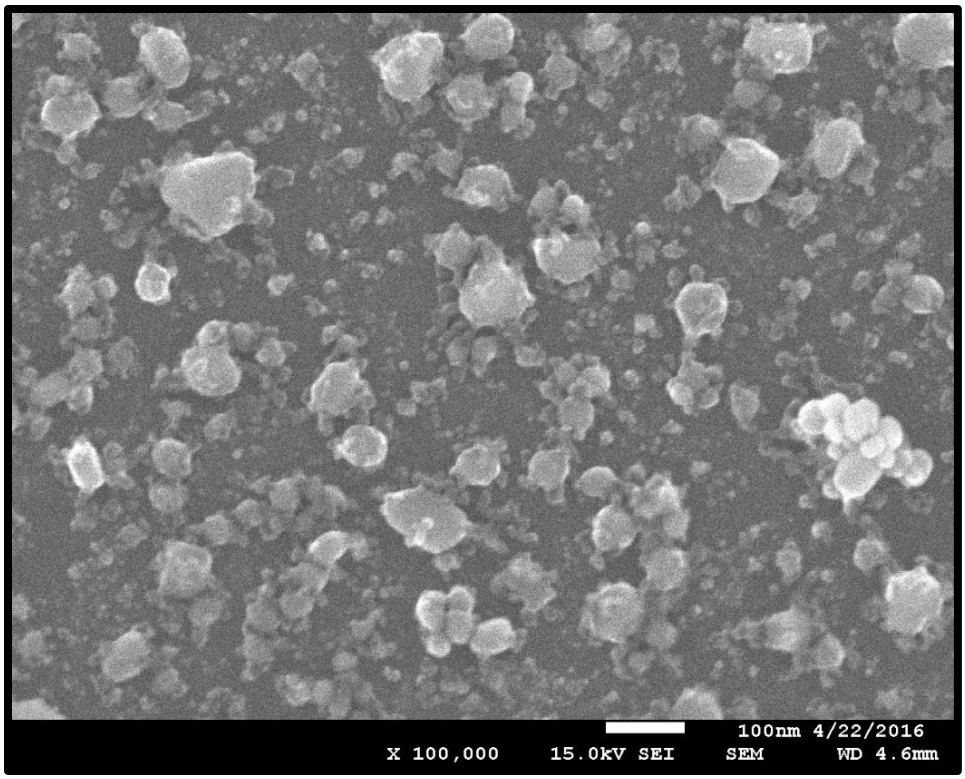

Figure 65: SEM image of sample L

7.3 Raman spectroscopy analysis of CVD samples

After the SEM analysis, CNT based films are characterized using Raman spectroscopy. Laser light is bombarded with the CNTs which have vibrating bonds in their molecules. After colliding with these vibrating bonds, they lose their energy and gets back scattered. The frequency of this backscattered laser is detected using a detector to find the bands present in the spectrum. This technique is mostly used to characterize carbonaceous materials.

Raman spectrum is plotted with Raman shift on x-axis and intensity on y-axis. To study CNTs using Raman spectroscopy, there are two important bands. G-band which is found at 1580cm^{-1} and D-band which is found at 1350cm^{-1}. G band represents graphitic nature or crystallinity of the CNTs and D band represents carbon impurities from sp^3 bonds or broken sp^2 bonds of CNTs. The intensity ratio of the bands (I_d / I_g) determine the quality of carbon nanotubes present in the sample. When the intensity of D-band is low compared to G-band it represents good quality of CNTs or CNTs with less defects. Figure 66 shows the Raman spectra of various CNT based films which are grown using MWCVD technique. The I_d / I_g ratio of the CNT based films grown using CVD are around 0.8-0.9 which prove the crystal nature and good quality of CNTs.

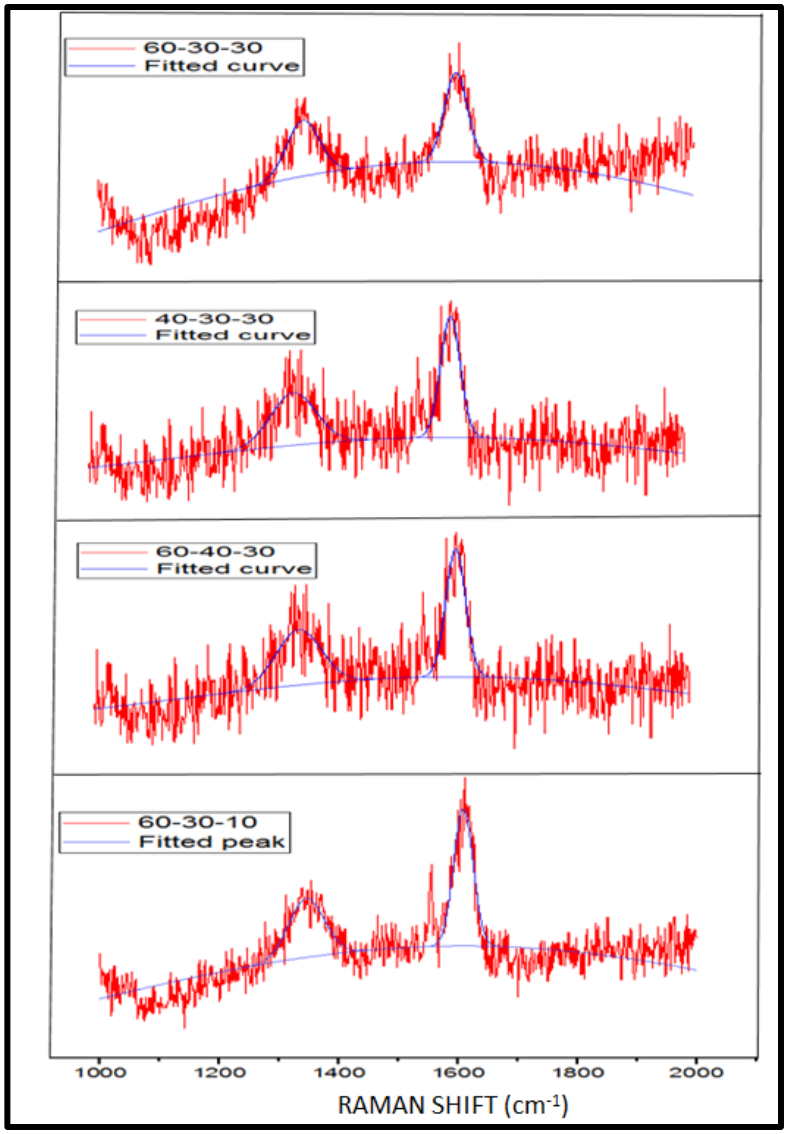

Figure 66: Raman spectra of B, I, J, L samples respectively

The numbers inside the picture (plotted in the legend) represent annealing time-plasma treatment time-growth time respectively. The experimental Raman spectra were simulated and fitted using Origin Pro 2016 software to determine the band positions and the intensity of the bands. Further the data is plotted in Microsoft excel by superimposing the Raman spectroscopy plots to determine the difference in plots due to hydrogen annealing times (figure 67), plasma treatment times (figure 68) and growth times (figure 69) respectively.

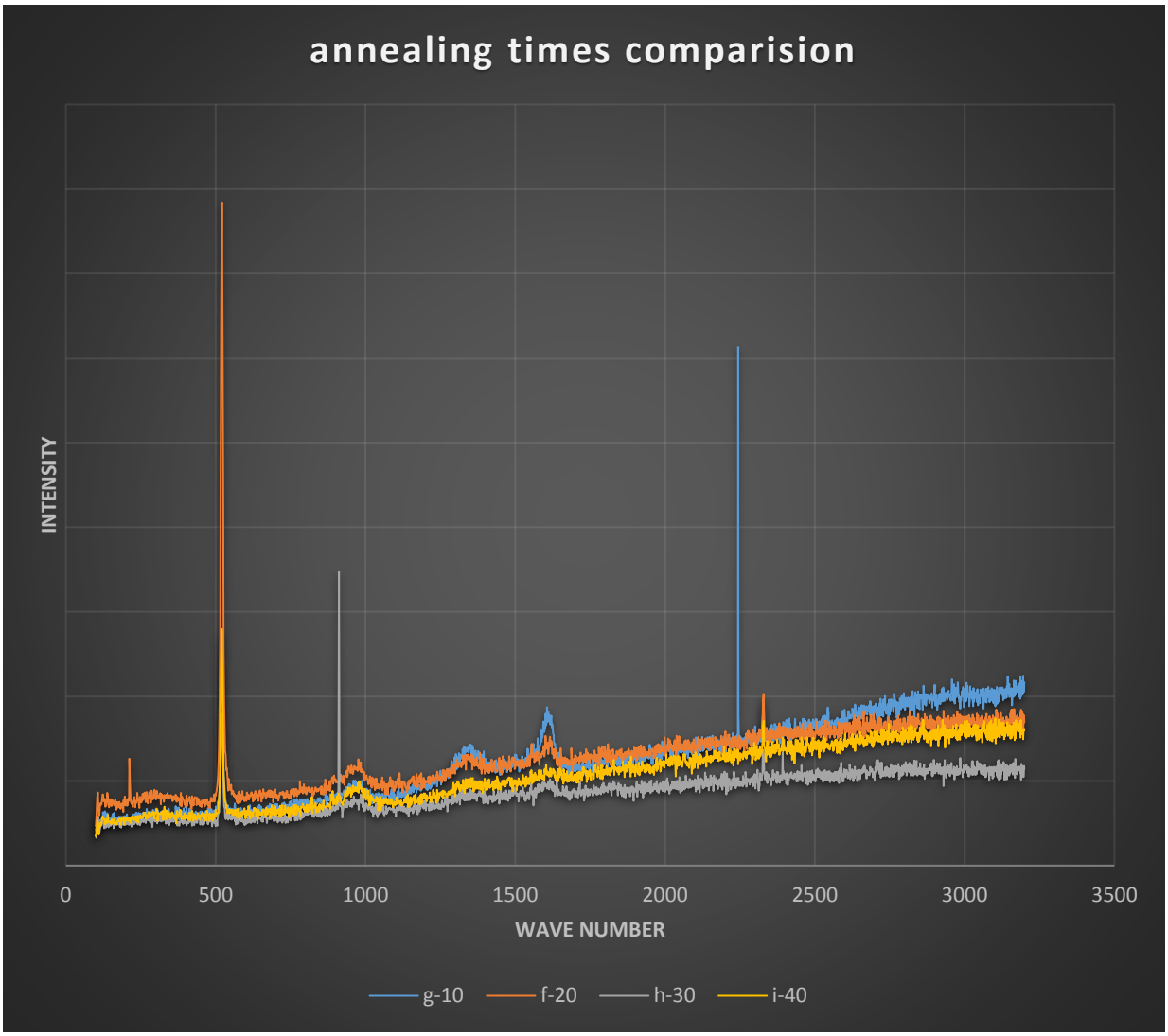

Figure 67: Raman plots of CVD samples varying annealing treatments times, while keeping plasma treatment and growth time constant

The alphabets mentioned inside the graphs, in the legend, represent our sample names and the numbers indicate the hydrogen annealing treatment times. The plasma treatment and growth times are kept constant during this study. In this graph, the Raman spectra of various samples are overlapped on one another to see the effect of hydrogen annealing times by keeping the plasma treatment time and growth time as constant. The peaks around 500 represent the silicon substrate peak.

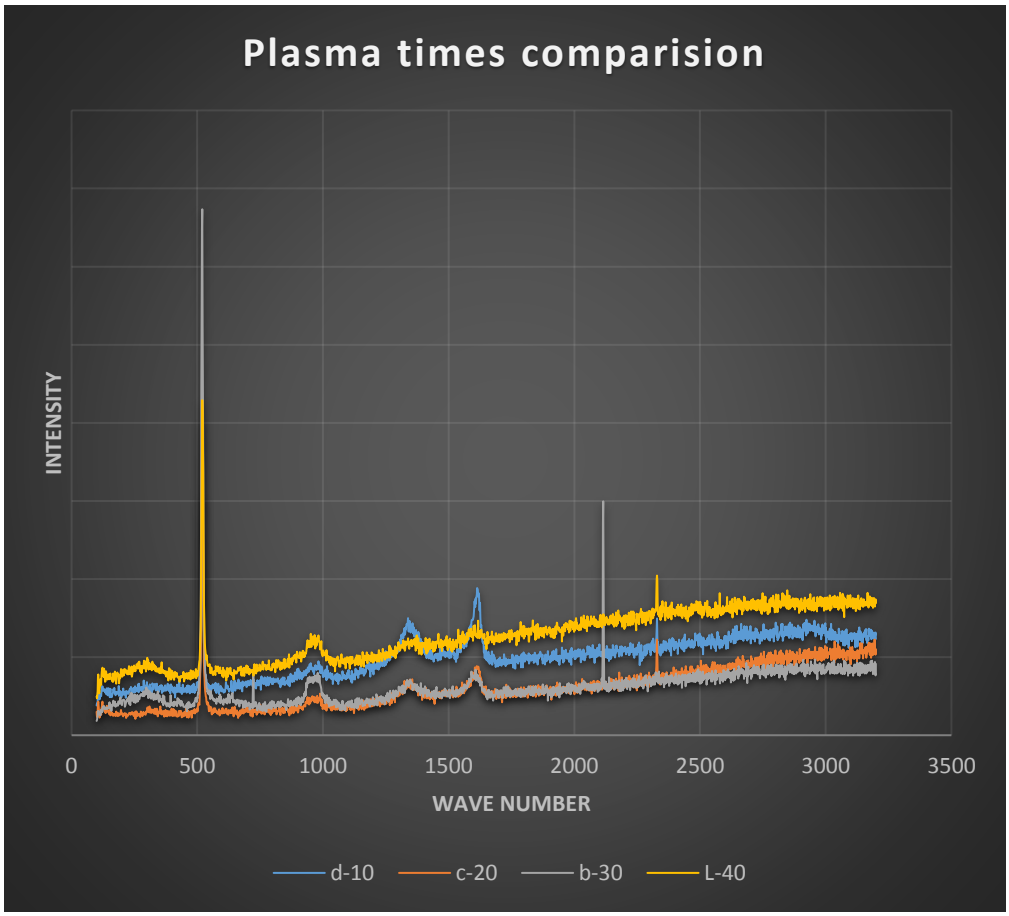

Figure 68: Raman plots of CVD samples varying plasma treatment times, while keeping annealing and growth time constant

The alphabets mentioned inside the graphs, in the legend, represent our sample names and the numbers indicate the plasma treatment times. The annealing and growth times are kept constant during this study. In this graph, the Raman spectra of various samples are overlapped on one another to see the effect of hydrogen plasma treatment times by keeping the annealing time and growth time as constant. The peaks around 500 represent the silicon substrate peak.

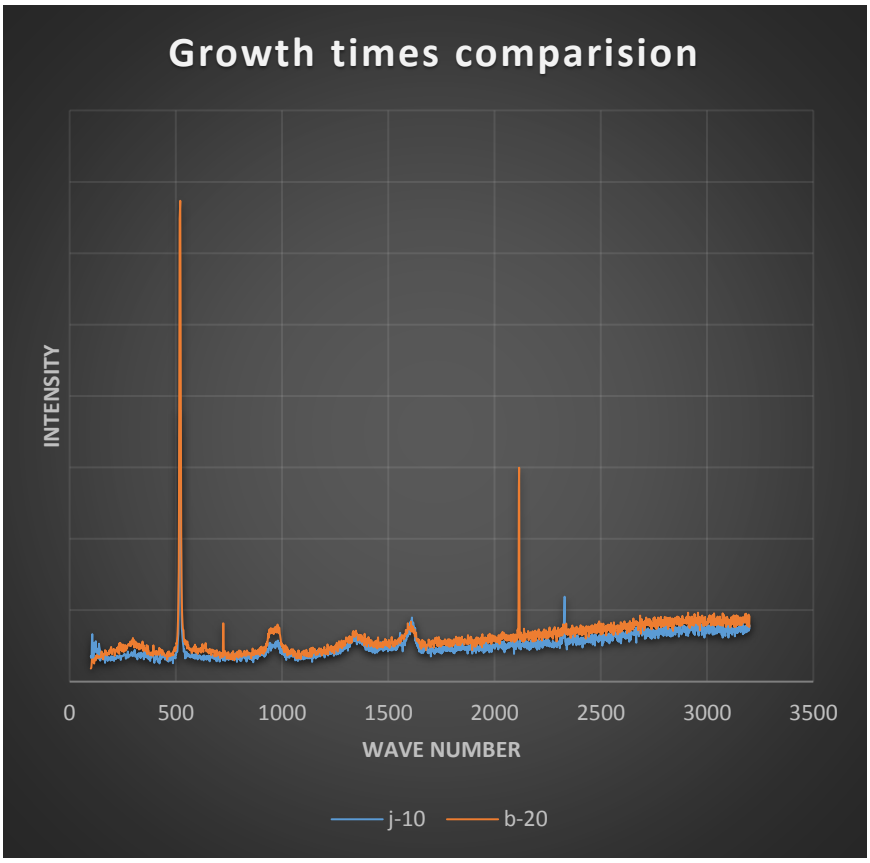

Figure 69: Raman plots of CVD samples varying growth times, while keeping annealing and plasma treatment time constant

The alphabets mentioned inside the graphs, in the legend, represent our sample names and the numbers indicate growth process times. Annealing time and plasma treatment times are kept constant during this study. In this graph, the Raman spectra of various samples are overlapped on one another to see the effect of CNTs growth times by keeping the annealing time and plasma treatment time as constant. The peaks around 500 represent the silicon substrate peak.

Further I_d / I_g ratios are calculated. They are the intensity ratios of D and G bands. These I_d / I_g ratios are calculated based on annealing treatment times, plasma treatment times and growth times. The trends of each parameter w.r.t. I_d / I_g are cleared understood from the plots. Figure 70, 71 and 72 plots the I_d / I_g data w.r.t. various parameters. I_d / I_g ratios show decreasing trend w.r.t. increase in hydrogen annealing times. I_d / I_g ratios show increasing trend with increase in plasma treatment time and growth time of the CVD samples.

Annealing reduces silicon oxide on the substrate and breaks down the nickel thin film into nickel nanoislands. Hence increasing the hydrogen annealing treatment enhances the growth of CNTs which can be represented with the decreasing trend of I_d / I_g ratios. Plasma treatment is used to convert nickel nano-islands to catalyst nano-island seeds. However, excessive plasma treatment results in the deposition of active hydrogen radical deposition on the nickel nanoislands, which

reduces the growth of CNTs. This effect can be seen in decreasing trend of I_d / I_g ratios. Growth of CNTs is done by admitting hydrocarbon gas and carrier gas into the reaction chamber. The carrier gas splits down the hydrocarbon gas into hydrogen and carbon. Hydrogen is sent out of chamber and carbon is deposited on the nickel catalyst seeds which grows out into CNTs. If the gases are admitted for long time and if the growth is performed for long time, there are chances for depositing hydrogen on the active radicals of hydrogen present due to excessive plasma treatment or deposition of excessive carbon on the catalyst seeds. This excessive deposition of radicals does not promote good growth and quality of CNTs.

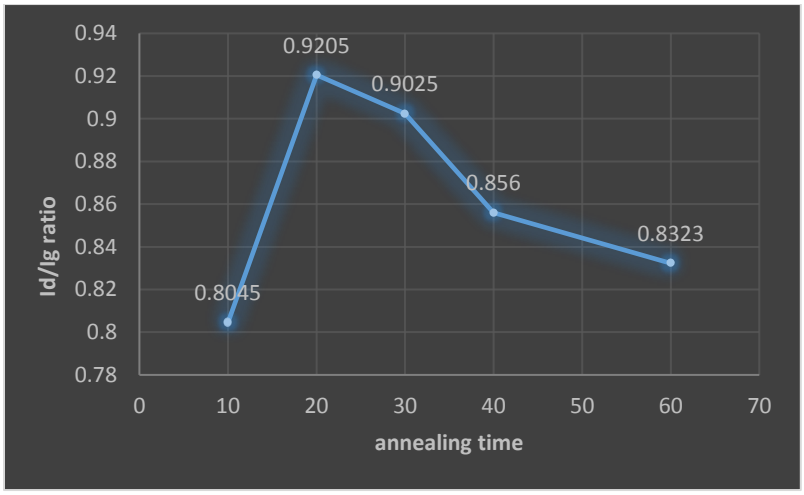

Figure 70: Id / Ig ratios vs. annealing treatment times

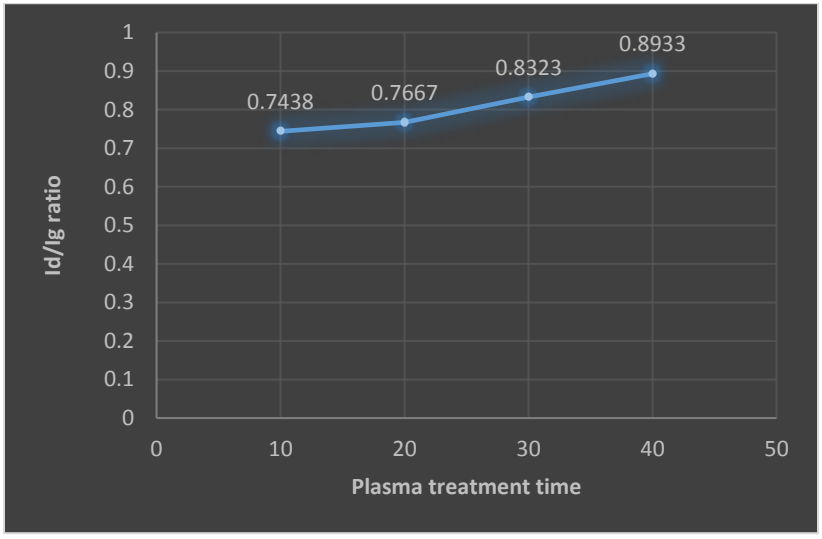

Figure 71: Id / Ig ratios vs. plasma treatment times

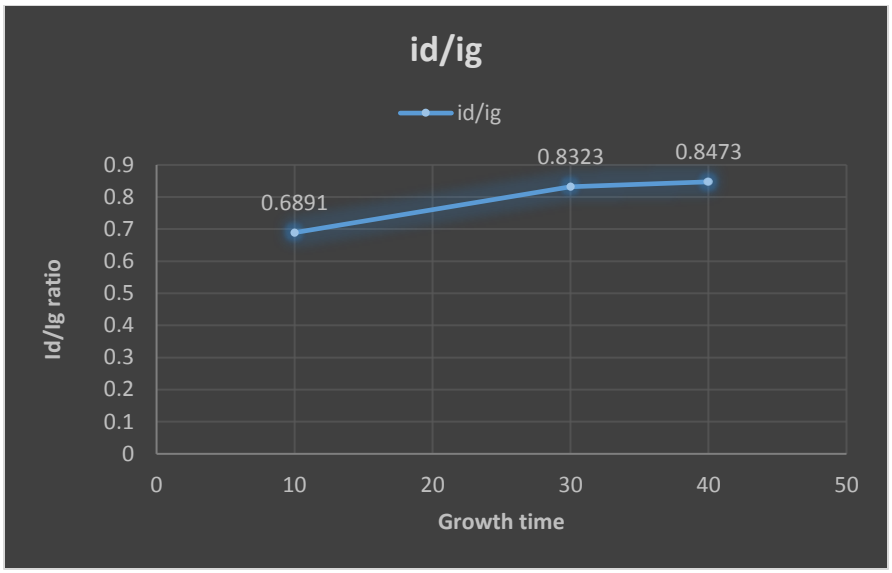

Figure 72: Id / Ig ratios vs. growth times

7.4 4-probe method analysis

The samples are characterized by linear 4-probe measurements to find out the electrical nature of the CNTs grown on the CNTs grown using PECVD technique. High impedance source is used to supply constant current through the outer probes. Digital voltmeter measures the voltage across two inner probes to determine resistance of the samples. This resistance can be used to understand the electrical conducting nature of films from the relation electrical conductivity is inversely proportional to resistance of the sample. This is a qualitative study of the samples. The results obtained are mentioned below in the table 5. It is to be noted that the resistance values are taken at different places in the sample and the average values are presented in the table.

Table 5: 4 probe measurement values of CVD samples

Sample Name	Annealing Time (in min.)	Plasma treatment Time (in min.)	Growth Time (in min.)	Resistance values (in KΩ)
B	60	30	30	144
C	60	20	30	111500
D	60	10	30	20
F	20	30	30	20
G	10	30	30	14.5

H	30	30	30	0.234
I	40	30	30	2.5
J	60	30	10	0.0096
K	60	30	40	0.89
L	60	40	30	0.25

After SEM, Raman and 4-probe analysis of CNT based films, the deposition parameters were analyzed and optimum parameters were found out. CNT based films were grown using the optimum parameters and 4-probe resistivity analysis was carried out to study the properties of optimized samples which are deposited. Table 6 shows the time intervals of various experimental optimized parameters and the resistance analysis are presented. These results shows that the resistance of CNT based films is very less which represents high electrical conductivity of the CNT based films of the samples which are deposited using the optimized parameters.

Table 6: 4 probe measurements of CNT based films with optimized parameters

Sample Name	Annealing Time (in min.)	Plasma treatment Time (in min.)	Growth Time (in min.)	Resistance values (in KΩ)
Optimized 1	20	40	30	0.049
Optimized 2	30	40	30	0.020

The SEM analysis, Raman spectroscopy analysis and 4-probe resistivity measurements helped us to conclude the optimized parameters for growth of CNT based films. However, it is to be noted that, the experimental parameters which are optimized are for the machine which was used in this research. Also, the properties of CNT based films are depend on each of the experimental parameters like annealing, plasma treatment and growth of CNTs. After the analysis of CNT based films grown using CVD technique, CNT-polymer based films are characterized further.

7.5 SEM analysis of CNT-polymer composite films

SEM analysis of CNT polymer based nanocomposite films was carried out to study the structure of films. After the deposition of CNT polymer composite thin films on glass substrates. They are cured at 80°C for 30minutes. SEM characterization was done to check the surface morphology and distribution of CNTs in the polymer matrix. Figure 73 and 74 shows the SEM images, at low and high magnifications, of 5wt. % CNT loaded composite sample which is spin coated onto a glass substrate at 500rpm for 30seconds. It was observed that; the surface of the CNT film is not

smooth. There are few pores on the top of thin film and CNTs are randomly distributed in the polymer matrix.

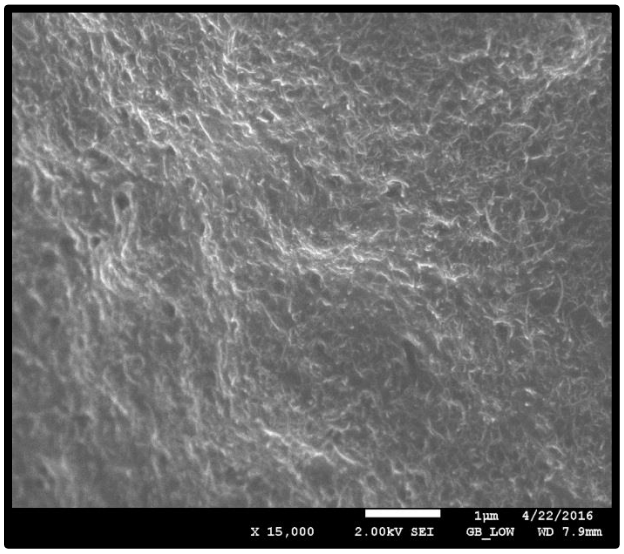

Figure 73: SEM image of 5wt. % CNT composite at low magnification

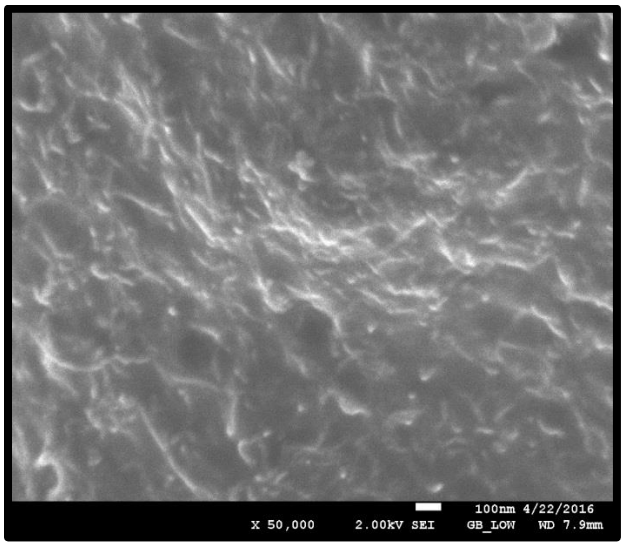

Figure 74: SEM image of 5wt. % CNT composite at high magnification

7.6 Experimental parameters

To study the characteristics of CNT-polymer based nanocomposite films, different experimental parameters are varied and the effects of these experimental parameters are discussed in the following sections. The experimental parameters which were varied during the experimental process are

1. UVO exposure time: varied from 0 to 14minutes.

2. CNT loading: varied amoung 1, 3, 5, 6.5 and 8 wt. % of CNT solution.
3. Spinning speeds: varied from 350, 500, 750 and 1000rpm for 30 seconds.
4. Number of layers: varied amoung single or double layer deposition.
5. Post deposition annealing temperatures: 80, 110 and 130°C for 10, 30 and 60minutes.

7.6.1 Effect of UVO exposure times

Deposition of films on any substrate should satisfy some requirements and conditions to enhance the adhesion related issues. The requirements vary based on the films, sbstrates, and the deposition methodology. Thin film deposition by physical and chemical methods require different conditions. In this case, as the film is coated using CNT-polymer based nanocomposite by spin coating based technique, the substrate surface should be hydrophillic so as to facilitate good bonding between the film and the substrate. In order to enhance the bonding properties, the substrate is exposed to ultra violet light for the required amount of time. The effect of UVO exposure is further discussed in this section.

Glass and PI substrates are initially cleaned with DI water and soap solution. This removes some the organic contaminants and dust from the substrate surface. In this experiment, the substrate is exposed to 10psi of compressed air. This UVO exposure excites the hydrocarbon contaminants on the surface by absorbing the short-wavelength UV radiation. At the same time, atomic oxygen is generated when the molecular oxygen is dissociated by smaller wavelength UV radiation. This atomic oxygen is combined with an oxygen molecule to synthesize ozone molecules which are subsequently dissociated by higher wavelength UV radiation. The products of excited and/or dissociated contaminant molecules react with an atomic oxygen molecule to form volatile molecules which desorb from the surface. Radicals such as *OH, COO*and CO* are also formed on the surface. Oxidation of the surface is responsible for the increase in the polar groups which is directly related to the adhesion properties of the material surface. The variation of the surface energy of the substrate with UVO cleaner time is very crucial to determine the point where surface energy reaches maximum value. Higher surface energy facilitates good adhesion properties between the nanocomposite film and the substrate. For polyimide substrates, after 14minutes of UVO plasma treatment, it reaches maximum surface energy of 86.5mN/m and after that no significant increase in surface energy is observed. The treatment was increased to 20 and 30minutes which didn't yield any further increase in surface energy. For glass substrates, the maximum energy was achieved after 10minutes of UVO treatment. However, in this case, to be consistent with the exposure times for different substrates, 14minutes exposure was used for all the substrates. In fact, the difference in surface energies of different substrates in given in the following table. From the table, it can be observed the variation in contact angle and surface energy before and after UVO exposure. However, for Si and Glass substrates, after the UVO treatment, the surface was completely hydrophilic which couldn't form a drop on the substrate instead it spread completely. This complete hydrophilic nature of substrate was used to form a film on the substrate with good adhesion bonding to film and the substrate. Figure 75 shows the

variation of surface energy with increase in UVO exposure. It can be observed that up to 14minutes of UVO exposure, the surface energy was increasing linearly and stopped further after reaching the maximum value which is about 86.5mN/m. These studies are extended to various substrates and the contact angle and surface energy variation of various substrates w.r.t. UVO treatment are listed in table 7.

Table 7: Variation of contact angle and surface energy before and after UVO treatments

Substrate	Before UVO contact angle	Before UVO surface energy	After UVO contact angle	After UVO surface energy
Polyimide	77.19 74.25	15.28 18.70	24.10 29.6	62.89 60
Si with SiO_2 with Ti and Ni	64.6 56.3	29.55 38.23	10 10.52	67.85 67.74
Si with SiO_2	20.35 18.9	64.60 65.19	16.5 15.2	66 66.49
Si	31.35 28.3	58.84 60.66	-	-
Glass	58.22 56.22	36.29 38.33	-	-

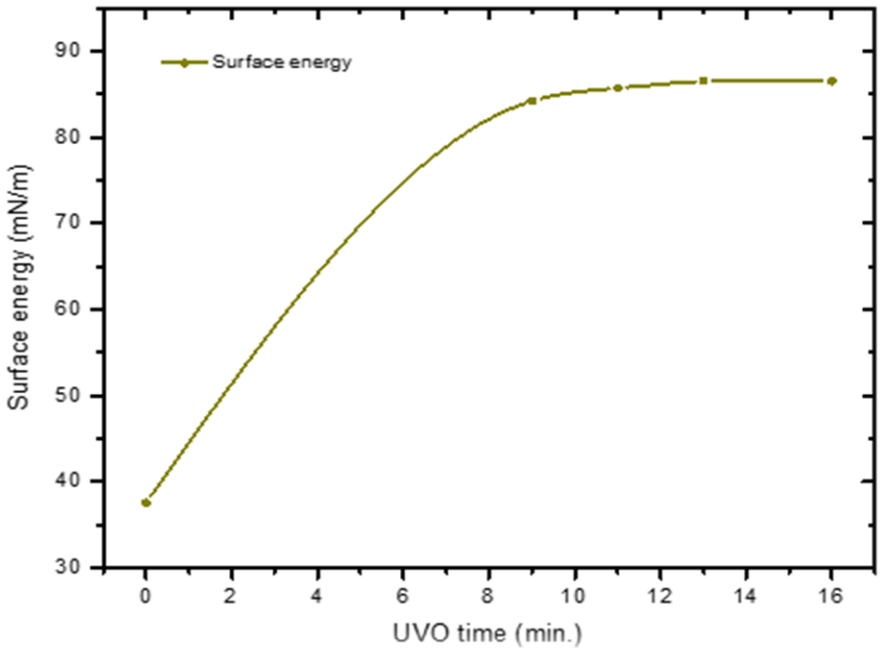

Figure 75: Effect of surface energy with respect to UVO time of deposition

7.6.2 Effect of CNT loading into the polymer composites

The proportion of CNTs in the nanocomposite changes its properties. Hence to study the effects of CNT loading in the polymer matrix, CNTs are added in various proportions. CNT quantity in PU matrix is varied in wt. % of the CNT-polyurethane solution. The loading varied from 1, 3, 5, 6.5 and 8 wt. % respectively. CNT solution is then spin coated on the UVO treated glass substrates at 500rpm for 30seconds. 1 and 3 wt. % solutions has very few CNTs dispersed in the solution, because of which the thin film is not uniform and it is highly porous. 6.5 and 8 wt. % loadings have large concentration of CNTs leading to agglomerations. So, when these solutions are deposited, they are not uniformly spread and hence result in agglomerations of CNTs on the substrate. 5wt. % CNT loading, seem to contain optimum CNT concentration in the nanocomposite solution. However, these films are porous. To get rid of pores and form a continuous film, a second layer is deposited on the top of first layer, after it is annealed. Figure 76 a, b, c, d, e shows 1, 3, 5, 6.5 and 8wt. % CNT single layer thin films respectively. From these films, it was observed that 1 and 3% films have very few CNTs and 5% solution have optimum CNTs and 5 and 8% have agglomerated CNTs on the film surface. The agglomerations of the CNTs in 6.5 and 8% solutions were observed by calculating the average surface roughness of 5, 6.5 and 8% films using surface profilometer. Figure 77 a, b and c show the increase in surface roughness of the 5%, 6.5% and 8 wt. % CNT based films respectively. The average surface roughness of these samples are 108.6, 145.5 and 151.5 micro inch respectively. This analysis was carried on Surface profilometer SJ-400 control unit.

a. b. c.

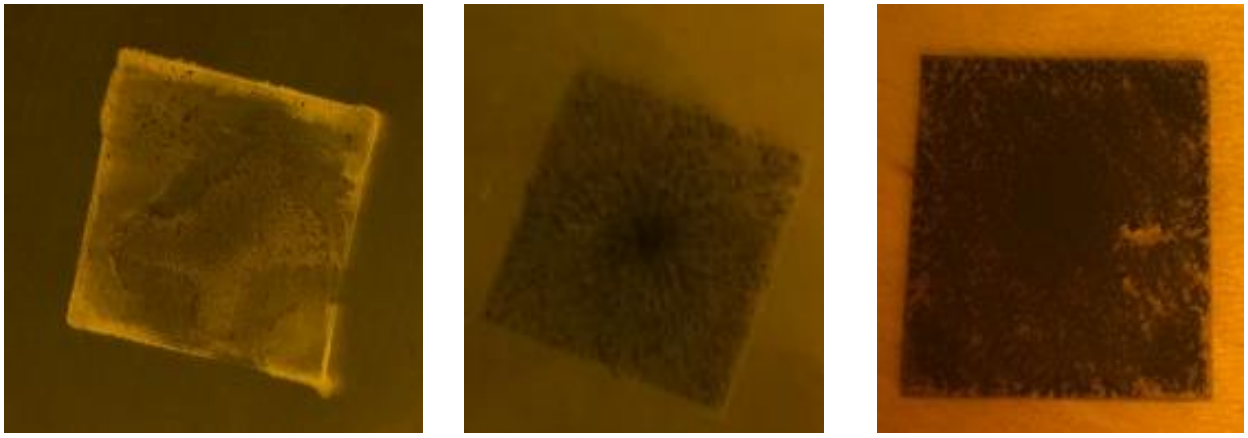

d. e.

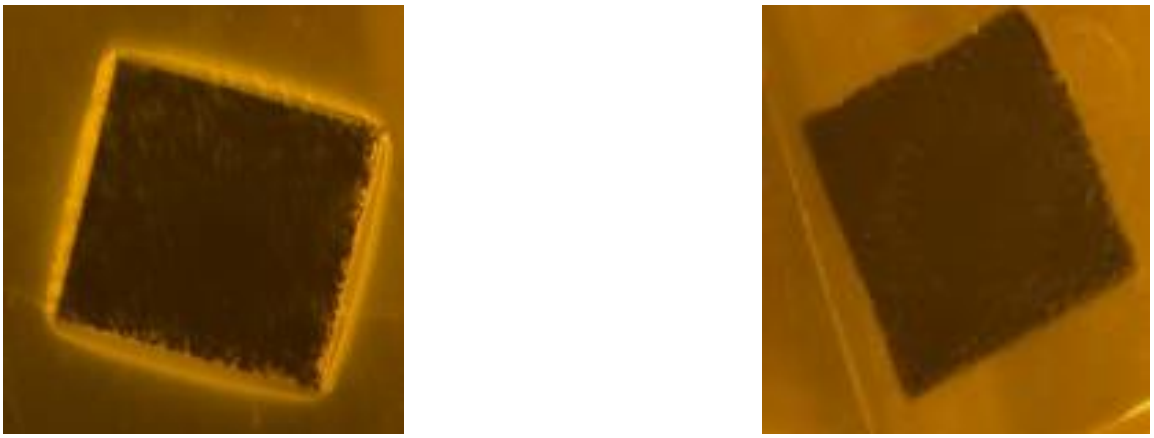

Figure 76: a, b, c, d and e represent 1, 3, 5, 6.5 and 8wt. % samples respectively

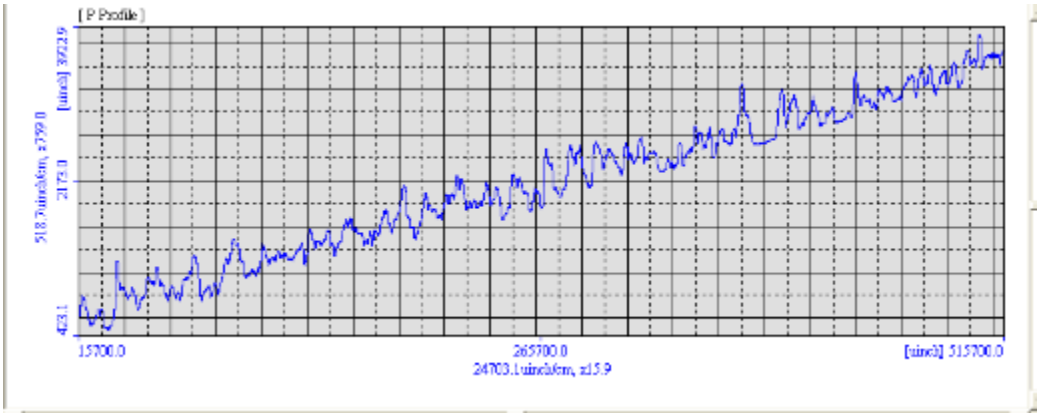

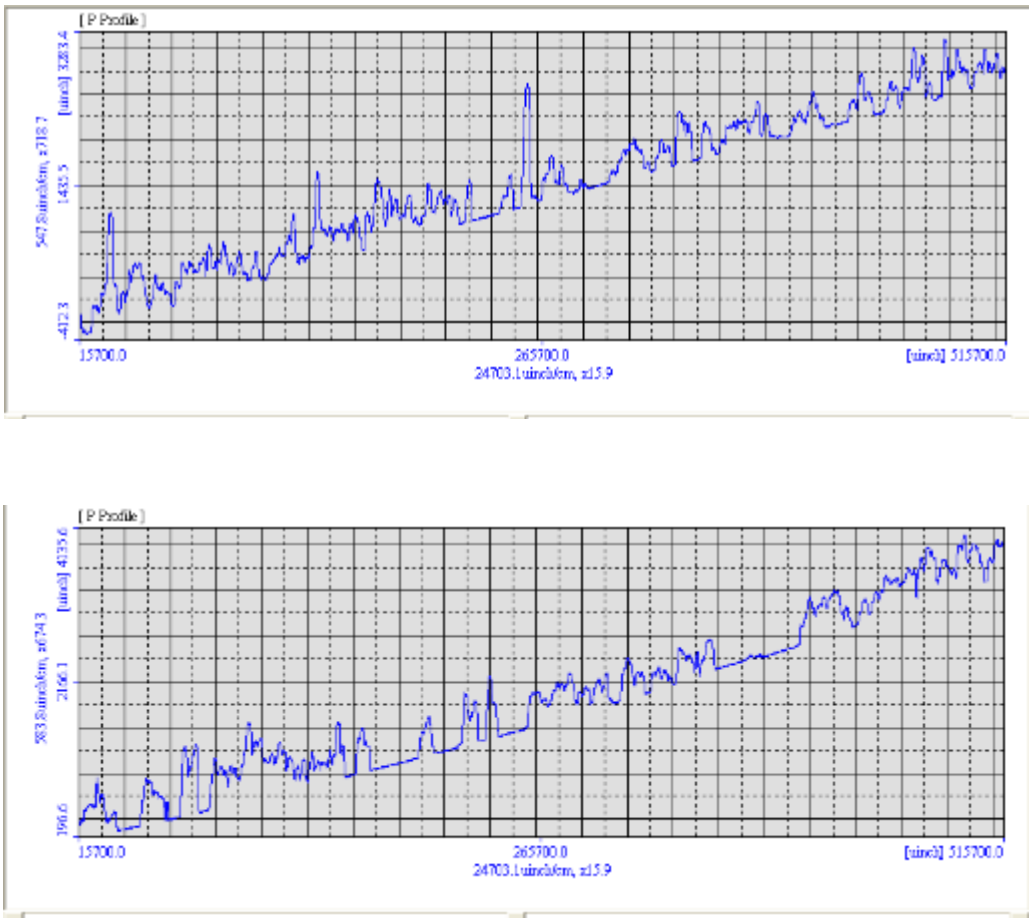

Figure 77: a, b, c depicts the average surface roughness of 5%, 6.5% and 8% CNT-polymer based films

7.6.3 Effect of spinning speeds

Nanocomposite films were prepared on various substrates using spin coating technique. The study of various spinning speeds on the film formation are studied to form a uniform film on the substrate. After the substrate is UVO treated and the CNT composite is synthesized, the substrate is placed on the spin coater. The spinning speeds are varied at 250, 500, 750 and 1000 rpm for 30 seconds. Figure 78 a, b, c, d shows 350, 500, 750 and 1000 rpm depositions of 5wt. % samples. It was observed that, at low spinning speeds, i.e. at 250 rpm, the composite doesn't uniformly spread on the substrate surface. At higher speeds, i.e. at 750 and 1000rpm, most of CNT composite tend to fly-off from the substrate and hence it doesn't form a uniform film. At 500rpm, the CNT composite spreads uniformly on the substrate and formed a film.

a. b.

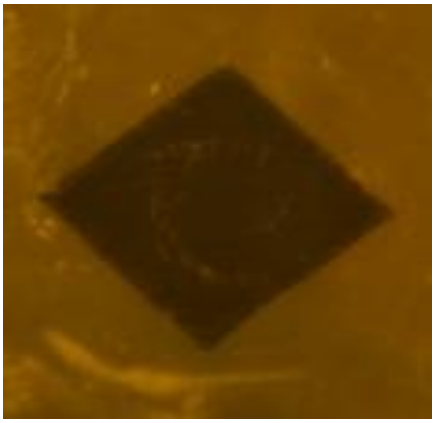

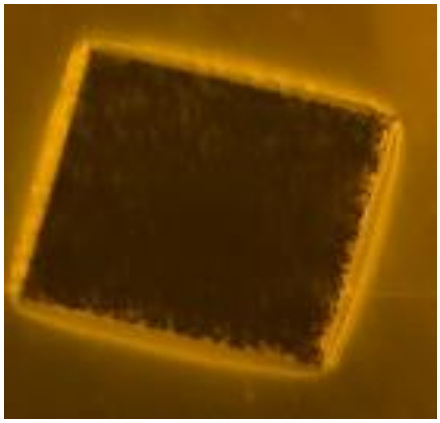

c. d.

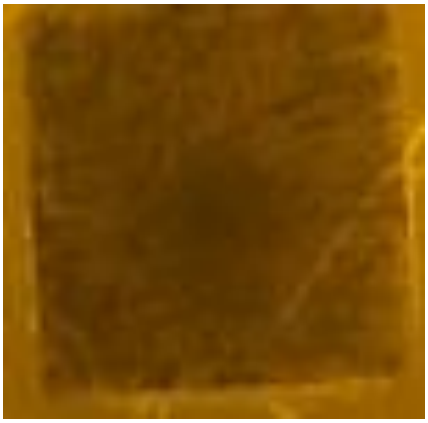

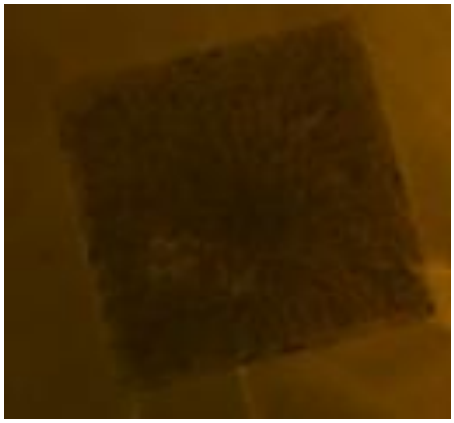

Figure 78: a, b, c, d shows 350, 500, 750 and 1000 rpm depositions for 30 seconds of 5wt. % solution

7.6.4 Multi-layer deposition

For all the 1-8wt. % CNT loading, deposited films are porous. The average size of the pores decreased with increase in the CNT loading. To improve the uniformity and formation of dense film, another layer is deposited on the top of the first layer. After the deposition of the first layer, the substrate with the nanocomposite film is annealed in an oven at 90°C for 30minutes. This helped to remove the moisture in the films and hence dry film was observed after annealing. This process is repeated for second time after drop casting on the first layer and spin coated again at same experimental conditions. After completing the second layer deposition, the substrate is once again placed in the oven for 30minutes and dried completely. After completing this process, a uniform thin film without any pores is obtained. Figure 79 and 80 shows the deposition of single layer and double layer of 5 wt. % CNT solution on the glass substrates respectively. These images were taken in transmission mode of the optical microscope. The black portion represents the film and the white portion represents the light transmitted below the substrate which is passing from

the pores of the film. It can be observed that, pore size on the films decreases with second layer deposition.

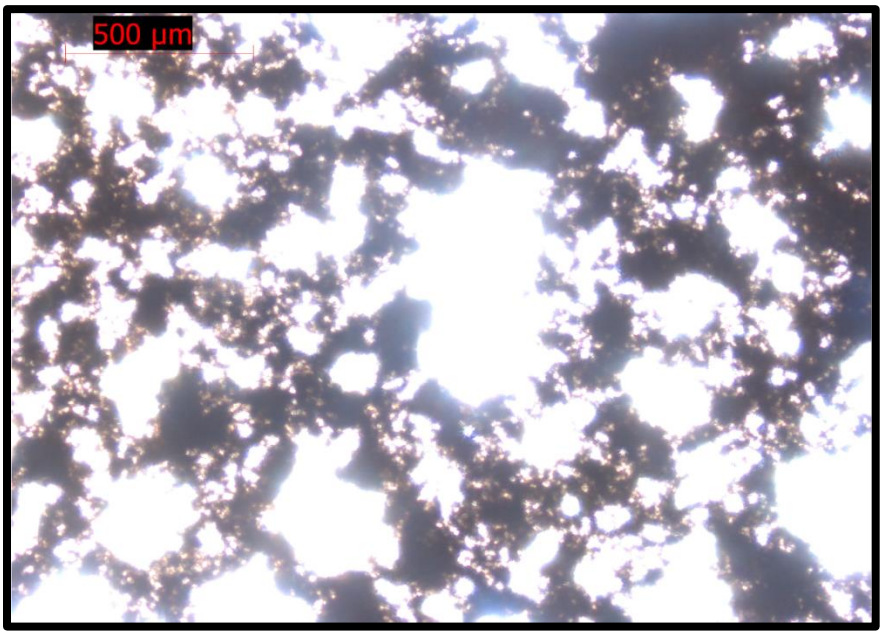

Figure 79: Single layer thin film of 5 wt. % CNT solution deposited on glass substrate

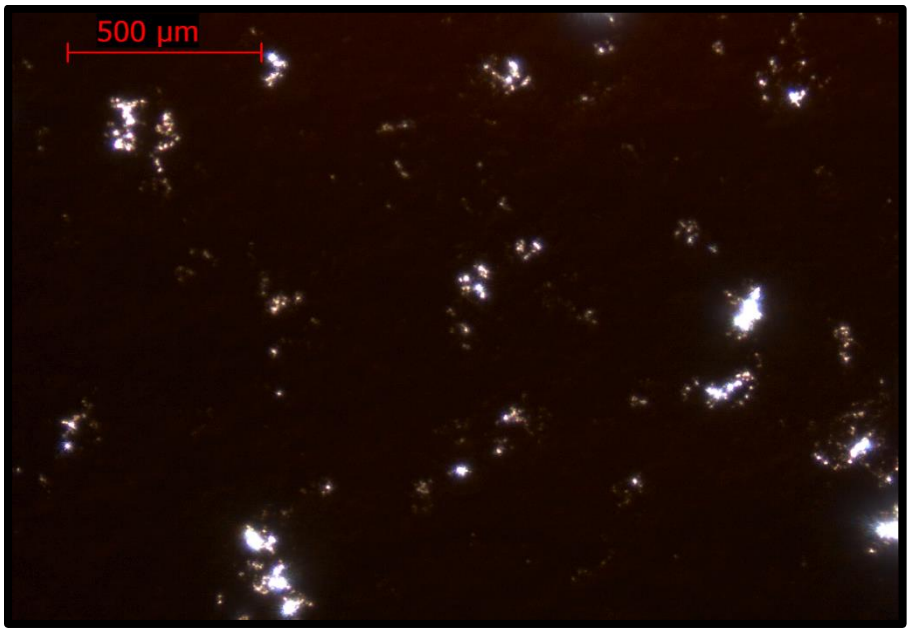

Figure 80: Double layer thin film of 5 wt. % CNT solution deposited on glass substrate

7.6.5 Effect of post deposition annealing temperatures

The films were annealed at different temperatures and times to remove moistures from the fabricated films. The single layer and double layer CNT nanocomposite films are post-annealed at temperatures varying from 80-130°C for 15-60mins to understand the effect of annealing on the films.

Initially the films are annealed at 80°C for 10 minutes and 30 minutes. The 5% films deposited on glass substrates are presented in figure 81 a and b. It was observed that after 10 and 20 minutes of annealing, the film was still wet and contained moisture. When the time was increased to 30 minutes the moisture in the films was removed and the film became totally dry and this was the scenario after annealing for higher durations. Then the temperature was increased to 110 and 130°C to observe the effect of temperature and this almost was like the above explanation. Hence annealing the sample at 80°C for 30minutes was optimum to prepare uniform CNT composite film on all the substrates.

a. b.

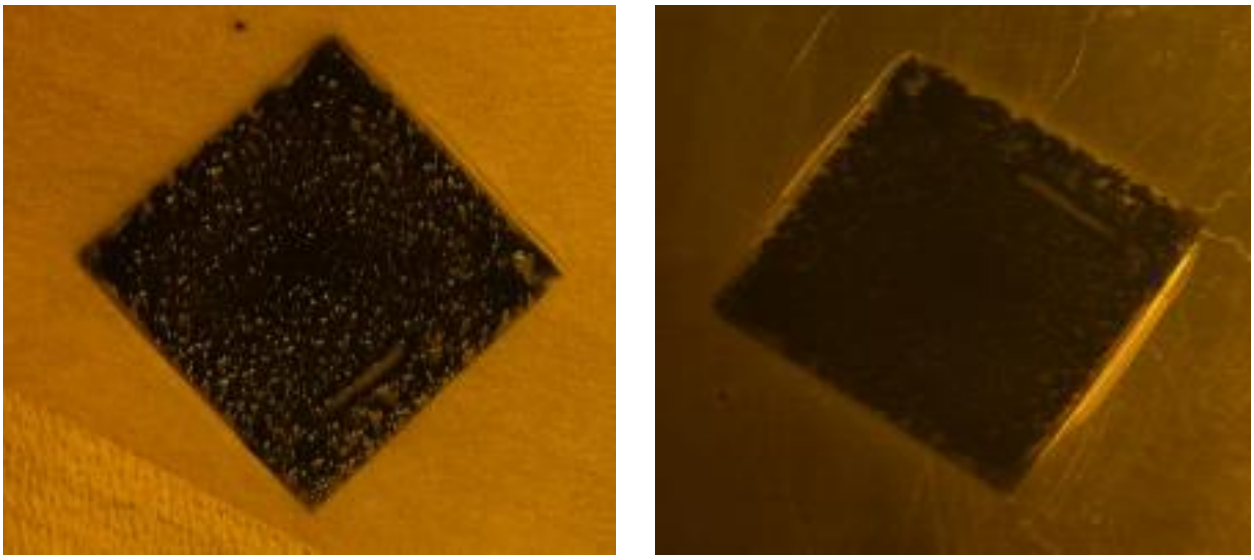

Figure 81: a and b shows post deposited annealing of samples at 80°C for 10 and 30minutes respectively

7.7 Raman spectroscopy analysis of CNT-polymer composites

Raman spectroscopy was carried on CNT based nanocomposite films to study the structural variations in the films. As discussed in the earlier sections G-band was found around 1580 cm^{-1} which is associated with longitudinal phonon mode and graphitic nature of sample. The presence of disorder sp^2 carbon atoms caused a D-band at 1345cm^{-1}. The relative intensity of these D and G bands indicates the quality of CNTs. Raw data was collected and plotted. I_d / I_g ratios are calculated and was observed to be greater than 1 which means that the D-band is dominating

over G-band. This might be because of the broken or defective sp^2 bonds which are formed when CNTs are dispersed in the polymer matrix. G prime peak was found around 2700 cm^{-1} which was assumed as the overtone of D-band. Figure 82 shows the superimposed Raman spectra of all the deposited CNT-polymer based films and respective bands of the spectra.

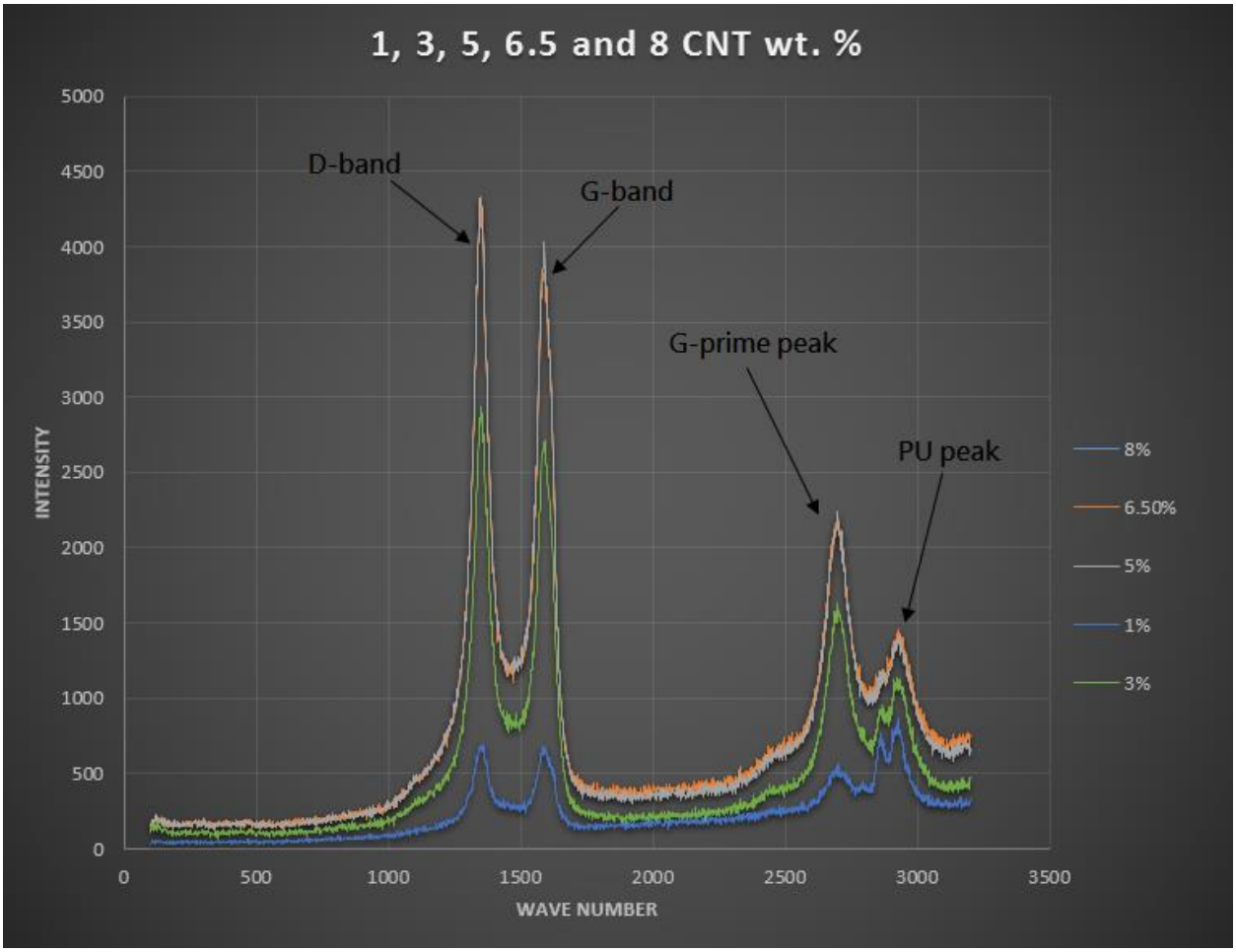

Figure 82: Raman spectroscopy graphs of 1, 3, 5, 6.5 and 8 wt. % CNT solutions superimposed on each other

7.8 4-probe characterization of CNT-polymer composites

4 pointer probe setup is used to characterize the electrical nature of the thin films. The analysis was done at 5- 6 places on the sample and the average resistance values are interpreted in table 8. Because 1% CNT film is not continuous, we could not obtain any conductivity on those samples. However other readings clearly explain the increase in electrical conductivity nature, with decrease in resistance, of CNT-polymer composite films with increase in CNT loading into

the solution. The resistance variation with increase in CNT loading was plotted in figure 83. It was observed that electrical conductivity increased with increase in CNT loading into the nanocomposite.

Table 8: CNT wt. % loading vs. 4-probe resistance values

CNT wt. % loading	Resistance (in K-ohms)
1	No conductivity
3	40
5	22
6.5	11.25
8	3.6

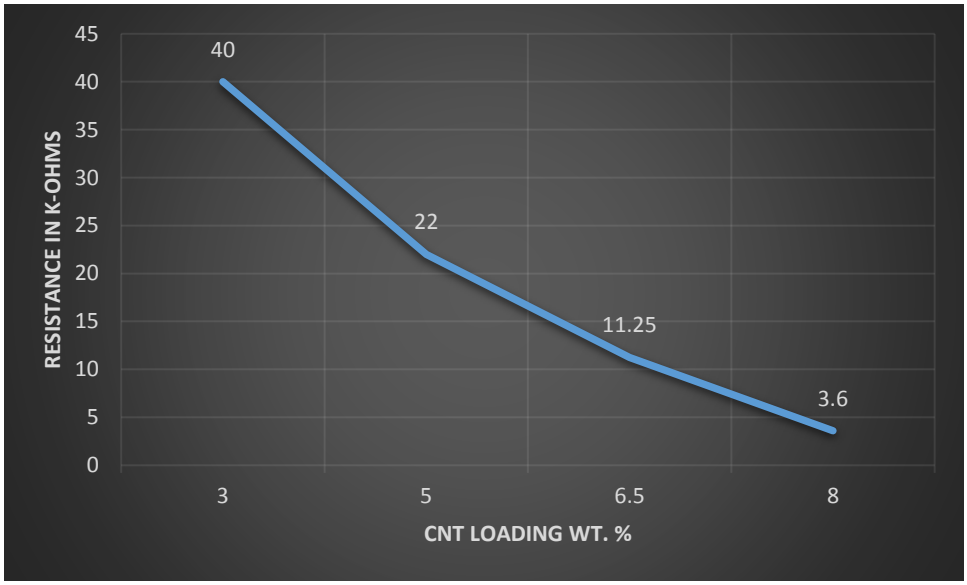

Figure 83: Resistance variation with increase in CNT loading

7.9 CONCLUSIONS

In this study, CNT based films are grown using two processes, viz., MWCVD and wet deposition of CNT-polyurethane nanocomposites. MWCVD required a Nickel Catalyst layer to facilitate the growth of CNTs on silicon substrates. Hence, the process optimization in the first method include the studies on the effect of Nickel catalyst layer, Hydrogen annealing time, pre-growth Hydrogen plasma treatment duration, CH_4+H_2 Plasma growth parameters. In the second method, synthesis of CNT-polyurethane nanocomposite constituted the major part, while the UVO substrate modification, composite spinning and annealing parameters formed the basic set of variables. The effect of these parameters on the structural phase, microstructure, uniformity, surface roughness and conductivity of the films was investigated using Rutherford Backscattering Spectroscopy (RBS), Scanning Electron Microscopy (SEM) and Optical Microscopy, Surface profilometry and four probe resistance measurement techniques respectively.

In Microwave CVD deposition of multiwall CNT films, this study showed that 20-30 minutes of annealing removed nickel oxide and formed nickel nano-islands, Plasma pre-treatment was found out to giver better catalyst nano seeds at 40 minutes treatment and 30minutes growth treatment provided CNTs with better structures. However these were observations for particular machine used in the research and also specific power used in the experiments. The CNTs prepared by using the optimum parameters yielded better results when characterized.

Carbon nanotubes are loaded in to the polymer matrix and it was observed that 5 wt. % CNT loading was optimum to synthesis the nanocomposite solution. 14 minutes of UVO treating the substrate, depositing the films at 500 rpm for 30 seconds and post annealing them at 80°C for 30minutes and depositing a double layer on the top was first layer were observed to be optimum conditions to form a continuous film with less pores.

COMSOL Multiphysics software was observed to be the best tool to analyze strain sensing films. The model is initially validated by solving the commercially purchased strain sensor and comparing the results with the manufacturer provided results. Then the nanocomposite strain sensor is analyzed by using its properties from the literature and observed that the values are in good agreement with the values from the literature.

CNT-polyurethane nanocomposite strain sensor was fabricated using optical lithography. However this process needs to be further optimized to form better strain gauge structures and utilize them in the commercial applications.

BIBLIOGRAPHY

[1] T. W. Chou, L. Gao, E. T. Thostenson, Z. Zhang, and J. H. Byun, "An assessment of the science and technology of carbon nanotube-based fibers and composites," *Compos. Sci. Technol.*, vol. 70, no. 1, pp. 1–19, 2010.

[2] N. Behabtu, M. J. Green, and M. Pasquali, "Carbon nanotube-based neat fibers," *Nano Today*, vol. 3, no. 5–6, pp. 24–34, 2008.

[3] S. N. Habisreutinger, T. Leijtens, G. E. Eperon, S. D. Stranks, R. J. Nicholas, and H. J. Snaith, "Carbon nanotube/polymer composites as a highly stable hole collection layer in perovskite solar cells," *Nano Lett.*, vol. 14, no. 10, pp. 5561–5568, 2014.

[4] M. F. L. De Volder, S. H. Tawfick, R. H. Baughman, and A. J. Hart, "Carbon Nanotubes: Present and Future Commercial Applications," *Science (80-.).*, vol. 339, no. 6119, pp. 535–539, 2013.

[5] S. Sorgenfrei, C. Chiu, R. L. Gonzalez, Y.-J. Yu, P. Kim, C. Nuckolls, and K. L. Shepard, "Label-free single-molecule detection of DNA-hybridization kinetics with a carbon nanotube field-effect transistor.," *Nat. Nanotechn.*, vol. 6, no. 2, pp. 126–32, 2011.

[6] P. Chen, H. Chen, J. Qiu, and C. Zhou, "Inkjet printing of single-walled carbon nanotube/RuO2 nanowire supercapacitors on cloth fabrics and flexible substrates," *Nano Res.*, vol. 3, no. 8, pp. 594–603, 2010.

[7] X. Xie, M. Ye, L. Hu, N. Liu, J. R. McDonough, W. Chen, H. N. Alshareef, C. S. Criddle, and Y. Cui, "Carbon nanotube-coated macroporous sponge for microbial fuel cell electrodes," *Energy Environ. Sci.*, vol. 5, no. 1, p. 5265, 2012.

[8] M. Ghasemi, M. Ismail, S. K. Kamarudin, K. Saeedfar, W. R. W. Daud, S. H. A. Hassan, L. Y. Heng, J. Alam, and S. E. Oh, "Carbon nanotube as an alternative cathode support and catalyst for microbial fuel cells," *Appl. Energy*, vol. 102, pp. 1050–1056, 2013.

[9] J. Qi, L. Xin, Z. Zhang, K. Sun, H. He, F. Wang, D. Chadderdon, Y. Qiu, C. Liang, and W. Li, "Surface dealloyed PtCo nanoparticles supported on carbon nanotube: facile synthesis and promising application for anion exchange membrane direct crude glycerol fuel cell," *Green Chem.*, vol. 15, no. 5, p. 1133, 2013.

[10] Z. Xiang, Z. Hu, D. Cao, W. Yang, J. Lu, B. Han, and W. Wang, "Metal-organic frameworks with incorporated carbon nanotubes: Improving carbon dioxide and methane storage capacities by lithium doping," *Angew. Chemie - Int. Ed.*, vol. 50, no. 2, pp. 491–494, 2011.

[11] M. Kinoshita, M. Steiner, M. Engel, J. P. Small, A. a Green, M. C. Hersam, R. Krupke, E. E. Mendez, and P. Avouris, "The polarized carbon nanotube thin film LED.," *Opt. Express*, vol. 18, no. 25, pp. 25738–45, 2010.

[12] P. Egan and J. a Stone, “Weak-value thermostat with 0.2 mK precision.,” *Opt. Lett.*, vol. 37, no. 23, pp. 4991–3, 2012.

[13] X. Fang, Y. Bando, M. Liao, T. Zhai, U. K. Gautam, A. Li, Y. Koide, and D. Golberg, “An efficient way to assemble ZnS Nanobelts as ultraviolet-light sensors with enhanced photocurrent and stability by,” *Adv. Funct. Mater.*, vol. 20, no. 3, pp. 500–508, 2010.

[14] Y. He, Y. Liu, X. Shen, L. Mo, and G. Dai, “Noninteractive localization of wireless camera sensors with mobile beacon,” *IEEE Trans. Mob. Comput.*, vol. 12, no. 2, pp. 333–345, 2013.

[15] M. Belsante, J. P. Selph, J. Lloyd, D. Ajay, G. Webster, N.-B. Le, and A. Peterson, “V3-01 Use of the Ohmmeter To Identify the Site of Fluid Leak During Artificial Urinary Sphincter Revision Surgery,” *J. Urol.*, vol. 193, no. 4, p. e335, 2015.

[16] B. E. N. Collen and J. E. M. Baillie, “edited by Jennifer Sills Barometer of Life : Sampling Barometer of Life :,” *Science (80-.).*, vol. 329, no. ii, p. 140, 2010.

[17] Q. Zeng, S. Wang, L. Yang, Z. Wang, T. Pei, Z. Zhang, L.-M. Peng, W. Zhou, J. Liu, W. Zhou, and S. Xie, “Carbon nanotube arrays based high-performance infrared photodetector [Invited],” *Opt. Mater. Express*, vol. 2, no. 6, p. 839, 2012.

[18] Y. C. Choi, Y. M. Shin, Y. H. Lee, B. S. Lee, G.-S. Park, W. B. Choi, N. S. Lee, and J. M. Kim, “Controlling the diameter, growth rate, and density of vertically aligned carbon nanotubes synthesized by microwave plasma-enhanced chemical vapor deposition,” *Appl. Phys. Lett.*, vol. 76, no. 17, p. 2367, 2000.

[19] C. Kingston, R. Zepp, A. Andrady, D. Boverhof, R. Fehir, D. Hawkins, J. Roberts, P. Sayre, B. Shelton, Y. Sultan, V. Vejins, and W. Wohlleben, “Release characteristics of selected carbon nanotube polymer composites,” *Carbon N. Y.*, vol. 68, pp. 33–57, 2014.

[20] H. W. Kroto, J. R. Heath, S. C. O’Brien, R. F. Curl, and R. E. Smalley, “C 60: buckminsterfullerene,” *Nature*, vol. 318, p. 162, 1985.

[21] S. Iijima, “Helical microtubules of graphitic carbon,” *Nature*, vol. 354, no. 6348. pp. 56–58, 1991.

[22] S. Karthikeyan, P. Mahalingam, and M. Karthik, “Large Scale Synthesis of Carbon Nanotubes,” *E-Journal Chem.*, vol. 6, no. 1, pp. 1–12, 2009.

[23] J. W. G. Wilder, L. C. Venema, A. G. Rinzler, R. E. Smalley, and C. Dekker, “Electronic structure of atomically resolved carbon nanotubes,” *Nature*, vol. 391, no. 6662, pp. 59–62, 1998.

[24] A. M. Yu, O. Lourie, M. J. Dyer, K. Moloni, T. F. Kelly, R. S. Ruoff, M. Yu, O. Lourie, M. J. Dyer, K. Moloni, T. F. Kelly, and R. S. Ruoff, “Linked references are available on JSTOR for this article : Strength and Breaking Mechanism of Multiwalled Carbon Nanotubes Under Tensile Load,” vol. 287, no. 5453, pp. 637–640, 2016.

[25] D. P. Cruikshank, R. H. Brown, L. P. Giver, and A. T. Tokunaga, “Triton : Do We See to the

Surface ? Author (s): D . P . Cruikshank , R . H . Brown , L . P . Giver and A . T . Tokunaga Published by : American Association for the Advancement of Science Stable URL : http://www.jstor.org/stable/1704425 REFERENCES Linked," vol. 245, no. 4915, pp. 283–286, 2016.

[26] Q. H. Wang, T. D. Corrigan, J. Y. Dai, R. P. H. Chang, and a. R. Krauss, "Field emission from nanotube bundle emitters at low fields," *Appl. Phys. Lett.*, vol. 70, no. 24, p. 3308, 1997.

[27] L. Chernozatonskii, Y. Gulyaev, Zj. Kosakovskaja, N. Sinitsyn, G. Torgashov, Y. Zakharchenko, E. Fedorov, and V. Val, "Electron field emission from nanofilament carbon films," *Chem. Phys. Lett.*, vol. 233, no. February, pp. 63–68, 1995.

[28] J.-M. Bonard, J.-P. Salvetat, T. Stöckli, W. A. de De, L. Forró, and A. Châtelain, "Field emission from single-wall carbon nanotube films," *Appl. Phys. Lett.*, vol. 73, no. 7, pp. 918–920, 1998.

[29] O. M. Küttel, O. Groening, C. Emmenegger, and L. Schlapbach, "Electron field emission from phase pure nanotube films grown in a methane/hydrogen plasma," *Appl. Phys. Lett.*, vol. 73, no. 15, pp. 2113–2115, 1998.

[30] R. Martel, T. Schmidt, H. R. Shea, T. Hertel, and P. Avouris, "Single- and multi-wall carbon nanotube field-effect transistors," *Appl. Phys. Lett.*, vol. 73, no. 17, pp. 2447–2449, 1998.

[31] A. Merkoci, "Nanobiomaterials in Electroanalysis," *Electroanalysis*, vol. 19, no. 7, pp. 739–741, 2007.

[32] E. Frackowiak, K. Metenier, V. Bertagna, and F. Beguin, "Supercapacitor electrodes from multiwalled carbon nanotubes," *Appl. Phys. Lett.*, vol. 77, no. 15, p. 2421, 2000.

[33] H. Dai, N. Franklin, and J. Han, "Exploiting the properties of carbon nanotubes for nanolithography," *Appl. Phys. Lett.*, vol. 73, no. 11, pp. 1508–1510, 1998.

[34] M. Yu, "Strength and Breaking Mechanism of Multiwalled Carbon Nanotubes Under Tensile Load," *Science (80-.).*, vol. 287, no. 5453, pp. 637–640, 2000.

[35] W. Callister and D. Rethwisch, *Materials science and engineering: an introduction*, vol. 94. 2007.

[36] J.-P. Salvetat, J.-M. Bonard, and N. H. Thomson, "Mechanical properties of carbon nanotubes," *Appl. Phys. A*, vol. 69, no. 3, pp. 255–260, 1999.

[37] R. S. Ruoff and D. C. Lorents, "Mechanical and thermal properties of carbon nanotubes," *Carbon N. Y.*, vol. 33, no. 7, pp. 925–930, 1995.

[38] V. N. Popov, "Carbon nanotubes: Properties and application," *Mater. Sci. Eng. R Reports*, vol. 43, no. 3, pp. 61–102, 2004.

[39] J. P. Lu, "Elastic properties of carbon nanotubes and nanoropes," *Phys. Rev. Lett.*, vol. 79, no. 7, pp. 1297–1300, 1997.

[40] H. Ye, H. Lam, N. Titchenal, Y. Gogotsi, and F. Ko, "Reinforcement and rupture behavior

of carbon nanotubes-polymer nanofibers," *Appl. Phys. Lett.*, vol. 85, no. 10, pp. 1775–1777, 2004.

[41] Y. T. Ong, A. L. Ahmad, S. Hussein, S. Zein, and S. H. Tan, "A review on carbon nanotubes in an environmental protection and gree engineering perspective.," *Brazilian J Chem Engi*, vol. 27, no. 2, pp. 227–242, 2010.

[42] C. Kittel and P. McEuen, "Introduction to solid state physics," vol. 8, 1986.

[43] J. W. Mintmire, B. I. Dunlap, and C. T. White, "Are fullerene tubules metallic?," *Phys. Rev. Lett.*, vol. 68, no. 5, pp. 631–634, 1992.

[44] N. Hamada, S. I. Sawada, and A. Oshiyama, "New one-dimensional conductors: Graphitic microtubules," *Phys. Rev. Lett.*, vol. 68, no. 10, pp. 1579–1581, 1992.

[45] R. Saito, M. Fujita, G. Dresselhaus, and M. S. Dresselhaus, "Electronic structure of chiral graphene tubules," *Appl. Phys. Lett.*, vol. 60, no. 18, pp. 2204–2206, 1992.

[46] P. Poncharal, C. Berger, Y. Yi, Z. L. Wang, and W. A. De Heer, "Room temperature ballistic conduction in carbon nanotubes," *J. Phys. Chem. B*, vol. 106, no. 47, pp. 12104–12118, 2002.

[47] C. L. Kane and E. J. Mele, "Size, Shape, and Low Energy Electronic Structure of Carbon Nanotubes," *Phys. Rev. Lett.*, vol. 78, no. 10, pp. 1932–1935, 1997.

[48] A. Kleiner and S. Eggert, "Band gaps of primary metallic carbon nanotubes," *Phys. Rev. B*, vol. 63, no. 7, p. 73408, 2001.

[49] M. B. Nardelli, "Electronic transport in extended systems: Application to carbon nanotubes," *Phys. Rev. B*, vol. 60, no. 11, pp. 7828–7833, 1999.

[50] A. Maiti, A. Svizhenko, and M. P. Anantram, "Electronic transport through carbon nanotubes: effects of structural deformation and tube chirality.," *Phys. Rev. Lett.*, vol. 88, no. 12, p. 126805, 2002.

[51] L. Yang and J. Han, "Electronic structure of deformed carbon nanotubes," *Phys. Rev. Lett.*, vol. 85, no. 1, pp. 154–157, 2000.

[52] T. Tombler, C. Zhou, L. Alexseyev, J. Kong, H. Dai, L. Liu, C. Jayanthi, M. Tang, and S. Wu, "Reversible electromechanical characteristics of carbon nanotubes under local-probe manipulation," *Nature*, vol. 405, no. 6788, pp. 769–772, 2000.

[53] E. D. Minot, Y. Yaish, V. Sazonova, J.-Y. Park, M. Brink, and P. L. McEuen, "Tuning carbon nanotube band gaps with strain.," *Phys. Rev. Lett.*, vol. 90, no. April, p. 156401, 2003.

[54] T. Fukuda, F. Arai, and L. Dong, "Assembly of nanodevices with carbon nanotubes through nanorobotic manipulations," *Proc. IEEE*, vol. 91, no. 11, pp. 1803–1818, 2003.

[55] S. Iijima and T. Ichihashi, "Single-shell carbon nanotubes of 1-nm diameter," *Nature*, vol. 363, pp. 603–605, 1993.

[56] A. R. Library, “Cobalt-catalysed growth of carbon nanotubes with single-atom,” *Library (Lond).*, 1993.

[57] L. C. Qin, D. Zhou, A. R. Krauss, and D. M. Gruen, “Growing carbon nanotubes by microwave plasma-enhanced chemical vapor deposition,” *Appl. Phys. Lett.*, vol. 72, no. 26, pp. 3437–3439, 1998.

[58] M. Okai, T. Muneyoshi, T. Yaguchi, and S. Sasaki, “Structure of carbon nanotubes grown by microwave-plasma-enhanced chemical vapor deposition,” *Appl. Phys. Lett.*, vol. 77, no. 21, p. 3468, 2000.

[59] H. Cui, O. Zhou, and B. R. Stoner, “Deposition of aligned bamboo-like carbon nanotubes via microwave plasma enhanced chemical vapor deposition,” *J. Appl. Phys.*, vol. 88, no. 10, p. 6072, 2000.

[60] V. I. Merkulov, D. H. Lowndes, Y. Y. Wei, G. Eres, E. Voelkl, V. I. Merkulov, D. H. Lowndes, Y. Y. Wei, and G. Eres, “Patterned growth of individual and multiple vertically aligned carbon nanofibers Patterned growth of individual and multiple vertically aligned carbon nanofibers,” vol. 3555, no. 2000, pp. 10–13, 2016.

[61] M. Chhowalla, K. B. K. Teo, C. Ducati, N. L. Rupesinghe, G. A. J. Amaratunga, A. C. Ferrari, D. Roy, and W. I. Milne, “Growth process conditions of vertically aligned carbon nanotubes using plasma enhanced chemical vapor deposition Growth process conditions of vertically aligned carbon nanotubes using plasma enhanced chemical vapor deposition,” vol. 5308, no. 2001, 2011.

[62] L. Delzeit, C. V. Nguyen, B. Chen, R. Stevens, A. Cassell, J. Han, and M. Meyyappan, “Multiwalled Carbon Nanotubes by Chemical Vapor Deposition Using Multilayered Metal Catalysts,” *J. Phys. Chem. B*, vol. 106, pp. 5629–5635, 2002.

[63] C. Bower, W. Zhu, S. Jin, and O. Zhou, “Plasma-induced alignment of carbon nanotubes,” *Appl. Phys. Lett.*, vol. 77, no. 6, p. 830, 2000.

[64] F. Ding, “The importance of strong-carbon-metal adhesion for catalytic nucleation of single-walled carbon nanotubes,” *Nano Lett.*, vol. 8, pp. 463–468, 2008.

[65] I. Kang, M. J. Schulz, J. H. Kim, V. Shanov, and D. Shi, “A carbon nanotube strain sensor for structural health monitoring,” *Smart Mater. Struct*, vol. 15, pp. 737–748, 2006.

[66] O. Breuer and U. Sundararaj, “Big returns from small fibers: A review of polymer/carbon nanotube composites,” *Polym. Compos.*, vol. 25, no. 6, pp. 630–645, 2004.

[67] S. Shang, L. Li, X. Yang, and Y. Wei, “Polymethylmethacrylate-carbon nanotubes composites prepared by microemulsion polymerization for gas sensor,” *Compos. Sci. Technol.*, vol. 69, no. 7–8, pp. 1156–1159, 2009.

[68] D. E. Hill, Y. Lin, A. M. Rao, L. F. Allard, and Y. P. Sun, “Functionalization of carbon nanotubes with polystyrene,” *Macromolecules*, vol. 35, no. 25, pp. 9466–9471, 2002.

[69] T. Liu, I. Y. Phang, L. Shen, S. Y. Chow, and W. De Zhang, “Morphology and mechanical

properties of multiwalled carbon nanotubes reinforced nylon-6 composites," *Macromolecules*, vol. 37, no. 19, pp. 7214–7222, 2004.

[70] M. Baibarac, I. Baltog, S. Lefrant, J. Y. Mevellec, and O. Chauvet, "Polyaniline and Carbon Nanotubes Based Composites Containing Whole Units and Fragments of Nanotubes," *Chem. Mater.*, vol. 15, no. 21, pp. 4149–4156, 2003.

[71] T. McNally, P. Pötschke, P. Halley, M. Murphy, D. Martin, S. E. J. Bell, G. P. Brennan, D. Bein, P. Lemoine, and J. P. Quinn, "Polyethylene multiwalled carbon nanotube composites," *Polymer (Guildf).*, vol. 46, no. 19 SPEC. ISS., pp. 8222–8232, 2005.

[72] S. Kanagaraj, F. R. Varanda, T. V. Zhil'tsova, M. S. A. Oliveira, and J. A. O. Simões, "Mechanical properties of high density polyethylene/carbon nanotube composites," *Compos. Sci. Technol.*, vol. 67, no. 15–16, pp. 3071–3077, 2007.

[73] L. D. Tijing, C. H. Park, W. L. Choi, M. T. G. Ruelo, A. Amarjargal, H. R. Pant, I. T. Im, and C. S. Kim, "Characterization and mechanical performance comparison of multiwalled carbon nanotube/polyurethane composites fabricated by electrospinning and solution casting," *Compos. Part B Eng.*, vol. 44, no. 1, pp. 613–619, 2013.

[74] F. H. Gojny, M. H. G. Wichmann, U. Köpke, B. Fiedler, and K. Schulte, "Carbon nanotube-reinforced epoxy-composites: Enhanced stiffness and fracture toughness at low nanotube content," *Compos. Sci. Technol.*, vol. 64, no. 15 SPEC. ISS., pp. 2363–2371, 2004.

[75] W. Chen, X. Tao, P. Xue, and X. Cheng, "Enhanced mechanical properties and morphological characterizations of poly(vinyl alcohol)-carbon nanotube composite films," *Appl. Surf. Sci.*, vol. 252, no. 5, pp. 1404–1409, 2005.

[76] J. Sandler, M. S. . Shaffer, T. Prasse, W. Bauhofer, K. Schulte, and a. . Windle, "Development of a dispersion process for carbon nanotubes in an epoxy matrix and the resulting electrical properties," *Polymer (Guildf).*, vol. 40, no. 21, pp. 5967–5971, 1999.

[77] Y. Pan, L. Li, S. H. Chan, and J. Zhao, "Correlation between dispersion state and electrical conductivity of MWCNTs/PP composites prepared by melt blending," *Compos. Part A Appl. Sci. Manuf.*, vol. 41, no. 3, pp. 419–426, 2010.

[78] P. Pötschke, A. R. Bhattacharyya, and A. Janke, "Melt mixing of polycarbonate with multiwalled carbon nanotubes: Microscopic studies on the state of dispersion," *Eur. Polym. J.*, vol. 40, no. 1, pp. 137–148, 2004.

[79] E. Assouline, a Lustiger, a H. Barber, C. a Cooper, E. Klein, E. Wachtel, and H. D. Wagner, "Nucleation ability of multiwall carbon nanotubes in\rpolypropylene composites," *J. Polym. Sci. B Polym. Phys. Ed.*, vol. 41, pp. 520–527, 2003.

[80] R. Andrews, D. Jacques, M. Minot, and T. Rantell, "Fabrication of carbon multiwall nanotube/polymer composites by shear mixing," *Macromol. Mater. Eng.*, vol. 287, no. 6, pp. 395–403, 2002.

[81] A. Sesis, M. Hodnett, G. Memoli, A. J. Wain, I. Jurewicz, A. B. Dalton, J. D. Carey, and G. Hinds, "Influence of acoustic cavitation on the controlled ultrasonic dispersion of carbon nanotubes," *J. Phys. Chem. B*, vol. 117, no. 48, pp. 15141–15150, 2013.

[82] M. Njuguna, "Characterisation of multi wall carbon nanotube–polymer composites for strain sensing applications," p. 210, 2012.

[83] A. H. Barber, Q. Zhao, H. D. Wagner, and C. A. Baillie, "Characterization of E-glass-polypropylene interfaces using carbon nanotubes as strain sensors," *Compos. Sci. Technol.*, vol. 64, no. 13–14, pp. 1915–1919, 2004.

[84] T. Yamada, Y. Hayamizu, Y. Yamamoto, Y. Yomogida, A. Izadi-Najafabadi, D. N. Futaba, and K. Hata, "A stretchable carbon nanotube strain sensor for human-motion detection," *Nat. Nanotechnol.*, vol. 6, no. 5, pp. 296–301, 2011.

[85] E. T. Thostenson and T. Chou, "Aligned multi-walled carbon nanotube-reinforced composites : processing and mechanical characterization," vol. 77.

[86] J. O. Aguilar, J. R. Bautista-Quijano, and F. Avilés, "Influence of carbon nanotube clustering on the electrical conductivity of polymer composite films," *Express Polym. Lett.*, vol. 4, no. 5, pp. 292–299, 2010.

[87] Y. Zeng, P. Liu, J. Du, L. Zhao, P. M. Ajayan, and H. M. Cheng, "Increasing the electrical conductivity of carbon nanotube/polymer composites by using weak nanotube-polymer interactions," *Carbon N. Y.*, vol. 48, no. 12, pp. 3551–3558, 2010.

[88] M. K. Shin, J. Oh, M. Lima, M. E. Kozlov, S. J. Kim, and R. H. Baughman, "Elastomeric conductive composites based on carbon nanotube forests," *Adv. Mater.*, vol. 22, no. 24, pp. 2663–2667, 2010.

[89] Z. Spitalsky, D. Tasis, K. Papagelis, and C. Galiotis, "Carbon nanotube–polymer composites: Chemistry, processing, mechanical and electrical properties," *Prog. Polym. Sci.*, vol. 35, no. 3, pp. 357–401, 2010.

[90] W. Cui, F. Du, J. Zhao, W. Zhang, Y. Yang, X. Xie, and Y. W. Mai, "Improving thermal conductivity while retaining high electrical resistivity of epoxy composites by incorporating silica-coated multi-walled carbon nanotubes," *Carbon N. Y.*, vol. 49, no. 2, pp. 495–500, 2011.

[91] A. I. Oliva-Avilés, F. Avilés, and V. Sosa, "Electrical and piezoresistive properties of multi-walled carbon nanotube/polymer composite films aligned by an electric field," *Carbon N. Y.*, vol. 49, no. 9, pp. 2989–2997, 2011.

[92] M. Mahmoodi, M. Arjmand, U. Sundararaj, and S. Park, "The electrical conductivity and electromagnetic interference shielding of injection molded multi-walled carbon nanotube/polystyrene composites," *Carbon N. Y.*, vol. 50, no. 4, pp. 1455–1464, 2012.

[93] Q. Liu, J. Tu, X. Wang, W. Yu, W. Zheng, and Z. Zhao, "Electrical conductivity of carbon nanotube/poly(vinylidene fluoride) composites prepared by high-speed mechanical

mixing," *Carbon N. Y.*, vol. 50, no. 1, pp. 339–341, 2012.

[94] L. C. Tang, Y. J. Wan, K. Peng, Y. B. Pei, L. Bin Wu, L. M. Chen, L. J. Shu, J. X. Jiang, and G. Q. Lai, "Fracture toughness and electrical conductivity of epoxy composites filled with carbon nanotubes and spherical particles," *Compos. Part A Appl. Sci. Manuf.*, vol. 45, pp. 95–101, 2013.

[95] F. Gardea and D. C. Lagoudas, "Characterization of electrical and thermal properties of carbon nanotube/epoxy composites," *Compos. Part B Eng.*, vol. 56, pp. 611–620, 2014.

[96] S. Gong, Z. H. Zhu, and S. A. Meguid, "Anisotropic electrical conductivity of polymer composites with aligned carbon nanotubes," *Polymer (Guildf).*, vol. 56, pp. 498–506, 2015.

[97] A. C. Dissanayake, "Deposition and Characterization of Carbon Nanotubes (CNTS) Based Films for Sensing Applications," 2015.

[98] C. Li, E. T. Thostenson, and T. W. Chou, "Dominant role of tunneling resistance in the electrical conductivity of carbon nanotube-based composites," *Appl. Phys. Lett.*, vol. 91, no. 22, pp. 17–20, 2007.

[99] McCullough RL, *Micro-models for composite materials—particulate and discontinuous fiber composites*, 2nd ed. 1990.

[100] McCullough RL., *Micro-models for composite materials—continuous fiber composites*, 2nd ed. Delaware composites design encyclopedia, 1990.

[101] Y. J. Liu and X. L. Chen, "Evaluations of the effective material properties of carbon nanotube-based composites using a nanoscale representative volume element," *Mech. Mater.*, vol. 35, no. 1–2, pp. 69–81, 2003.

[102] X. L. Chen and Y. J. Liu, "Square representative volume elements for evaluating the effective material properties of carbon nanotube-based composites," *Comput. Mater. Sci.*, vol. 29, no. 1, pp. 1–11, 2004.

[103] X. Chen and Y. Liu, "Multiple-cell modeling of fiber-reinforced composites with the presence of interphases using the boundary element method," *Comput. Mater. Sci.*, vol. 21, no. 1, pp. 86–94, 2001.

[104] R. Zeiser, T. Fellner, and J. Wilde, "Development and testing of capacitive strain gauges," *Acad. day*, pp. 1–6, 2011.

[105] E. R. Silva, W. C. Oliveira, L. O. Arruda, R. Bonadiman, J. Quintero, R. Mancosu, and J. M. Silva Neto, "Finite element simulation of inkjet printed strain gage on polyimide substrates applied to flexible boards," *Proc. Electron. Packag. Technol. Conf. EPTC*, pp. 607–611, 2009.

[106] N. F. Deroller, "Finite Element Analysis Simulations of Micro and Nano-Electromechanical Sensors for Design Optimization," 2014.

[107] R. Zeiser, T. Fellner, and J. Wilde, “Capacitive strain gauges on flexible polymer substrates for wireless, intelligent systems,” *J. Sensors Sens. Syst.*, vol. 3, no. 1, pp. 77–86, 2014.

[108] “Finite Element Model of the Strain Gauge for Determining 1 Introduction 2 Principle of the Strain Gauge Measurement,” vol. LIX, no. 2, pp. 67–73, 2013.

[109] J. Vuillod, “<Properties of ZnO Films Prepared by dc and rf Diode Sputtering.pdf>,” vol. 87, no. 1972, 2013.

[110] Fridman, “Magnetron sputtering: basic physics and application to cylindrical magnetrons,” *J. Vac. Sci. Technol.*, vol. 15, no. 2, pp. 171–177, 1978.

[111] J. M. Poitevin and G. Lempkriere, “Pulverisation cathodique du titane : etude electrique et spectrometrique de la decharge pour les conditions optimales de depot (DC diode sputtering of titanium : determination of optimal deposition conditions by electrical and spectroscopic investigation,” vol. 9, pp. 1783–1795, 1976.

[112] S. Yamamichi, T. Sakuma, K. Takemura, and Y. Miyasaka, “SrTiO3 thin film preparation by Ion beam sputtering and its dielectric properties,” *Japanese J. Appl. Physics, Part 1 Regul. Pap. Short Notes Rev. Pap.*, vol. 30, pp. 2193–2196, 1991.

[113] N. Smyth, “Introduction,” *J. Hum. Behav. Soc. Environ.*, pp. 47–118, 2004.

[114] H. Ur Rashid, K. Yu, M. Naveed Umar, M. Naveed Anjum, K. Khan, N. Ahmad, and M. Tariq Jan, “Catalyst Role in Chemical Vapor Deposition (Cvd) Process: a Review,” *Rev. Adv. Mater. Sci*, vol. 40, pp. 235–248, 2015.

[115] M. Chhowalla, K. B. K. Teo, C. Ducati, N. L. Rupesinghe, G. A. J. Amaratunga, A. C. Ferrari, D. Roy, J. Robertson, and W. I. Milne, “Growth process conditions of vertically aligned carbon nanotubes using plasma enhanced chemical vapor deposition,” *J. Appl. Phys.*, vol. 90, no. 10, pp. 5308–5317, 2001.

[116] Z. Ren, Z. Huang, J. Xu, J. Wang, P. Bush, M. Siegal, and P. Provencio, “Synthesis of large arrays of well-aligned carbon nanotubes on glass,” *Science*, vol. 282, no. 5391, pp. 1105–7, 1998.

[117] R. Philippe, A. Morançais, M. Corrias, B. Caussat, Y. Kihn, P. Kalck, D. Plee, P. Gaillard, D. Bernard, and P. Serp, “Catalytic production of carbon nanotubes by fluidized-bed CVD,” *Chem. Vap. Depos.*, vol. 13, no. 9, pp. 447–457, 2007.

[118] S. Hofmann, C. Ducati, J. Robertson, and B. Kleinsorge, “Low-temperature growth of carbon nanotubes by plasma-enhanced chemical vapor deposition,” *Appl. Phys. Lett.*, vol. 83, no. 1, pp. 135–137, 2003.

[119] V. I. Merkulov, A. V. Melechko, M. A. Guillorn, D. H. Lowndes, and M. L. Simpson, “Alignment mechanism of carbon nanofibers produced by plasma-enhanced chemical-vapor deposition,” *Appl. Phys. Lett.*, vol. 79, no. 18, pp. 2970–2972, 2001.

[120] M. Dunlap and J. E. Adaskaveg, “Introduction to the Scanning Electron Microscope,” *Microsc. Microanal.*, p. 52, 1997.

[121] JEOL, “Scanning Electron Microscope A To Z,” *Serv. Adv. Technol.*, p. 32, 2006.

[122] B. Hafner and B. Hafner, “Scanning Electron Microscopy Primer,” *Cities*, pp. 1–29, 2007.

[123] L. Jacob, *An Introduction to Electron Optics*, vol. 20, no. 1. 1952.

[124] L. Reimer, *Scanning Electron Microscopy*, vol. 45, no. 9. 1998.

[125] W. Zhou, R. P. Apkarian, and Z. L. Wang, “Fundamentals of Scanning Electron Microscopy,” *Scanning Microsc. Nanotechnol.*, pp. 1–40, 2007.

[126] K. D. Vernon-Parry, “Scanning electron microscopy: an introduction,” *III-Vs Rev.*, vol. 13, no. 4, pp. 40–44, 2000.

[127] G. S. Bumbrah and R. M. Sharma, “Raman spectroscopy – Basic principle, instrumentation and selected applications for the characterization of drugs of abuse,” *Egypt. J. Forensic Sci.*, vol. 6, no. 3, pp. 209–215, 2016.

[128] L. M. Malard, M. A. Pimenta, G. Dresselhaus, and M. S. Dresselhaus, “Raman spectroscopy in graphene,” *Phys. Rep.*, vol. 473, no. 5–6, pp. 51–87, 2009.

[129] M. S. Dresselhaus, G. Dresselhaus, R. Saito, and A. Jorio, “Raman spectroscopy of carbon nanotubes,” *Phys. Rep.*, vol. 409, no. 2, pp. 47–99, 2005.

[130] M. S. Dresselhaus, G. Dresselhaus, A. Jorio, A. G. Souza Filho, and R. Saito, “Raman spectroscopy on isolated single wall carbon nanotubes,” *Carbon N. Y.*, vol. 40, no. 12, pp. 2043–2061, 2002.

[131] F. Fernandez-Lima, E. Vigil, I. Zumeta, F. L. Freire, R. Prioli, and E. Pedrero, “Rutherford backscattering spectrometry analysis of TiO2 thin films,” *Mater. Charact.*, vol. 50, no. 2–3, pp. 155–160, 2003.

[132] A. E. Adeoye, E. Ajenifuja, B. A. Taleatu, and A. Y. Fasasi, “Rutherford Backscattering Spectrometry Analysis and Structural Properties of Zn ? Pb 1 −? S Thin Films Deposited by Chemical Spray Pyrolysis,” vol. 2015, 2015.

[133] D. Primetzhofer, M. Sytnyk, P. J. Wagner, P. Bauer, and W. Heiss, “The potential of Rutherford Backscattering Spectrometry for composition analysis of colloidal nanocrystals,” *Nucl. Instruments Methods Phys. Res. Sect. B Beam Interact. with Mater. Atoms*, vol. 332, no. 1, pp. 122–125, 2014.

[134] C. A. Of and E. Structures, “BACKSCATTERING AND,” 1982.

[135] M. Mayer, “Rutherford Backscattering Spectrometry (RBS),” *Work. Nucl. Data Sci. Technol. Mater. Anal.*, no. May, pp. 19–30, 2003.

[136] R. Backscattering and T. S. Films, “Rutherford Backscattering Spectrometry (RBS) Analysis of Tungsten Silicide Films,” no. 1, pp. 3500–3501.

[137] Keithley Instruments Inc., “Measuring the resistivity and determining the conductivity type of semiconductor materials using a four-point collinear probe and the model 6221

DC and AC current source," no. 2615, pp. 1–4, 2005.

[138] A. Nagar, "Four Probe Method," pp. 3–4.

[139] four probe Principle, ". The constant of proportionality," *Instrument*, p. 2012, 2012.

[140] S. E. & Services, "Resistivity of Semiconductors by four probe method users manual," pp. 17–23.

[141] Y. Yan, J. Miao, Z. Yang, F.-X. Xiao, H. Bin Yang, B. Liu, and Y. Yang, "Carbon nanotube catalysts: recent advances in synthesis, characterization and applications.," *Chem. Soc. Rev.*, vol. 44, no. 10, pp. 3295–346, 2015.

[142] Microchem, "SU-8 2000 Permanent Epoxy Negative Photoresist," *Process. Guidel.*, 2015.

[143] P. Walker and W. H. Tarn, *Handbook_of_Metal_Etchants*. 1991.